Luiz Paulo Borges Miranda

Numerical Simulation of the Restart Flow of Thixotropic Elastoviscoplastic Materials in Contractions and Expansions Geometries Using OpenFoam

Brasil

2024

Luiz Paulo Borges Miranda

Numerical Simulation of the Restart Flow of Thixotropic Elastoviscoplastic Materials in Contractions and Expansions Geometries Using OpenFoam

Thesis submitted to the Programa de Pós-Graduação em Engenharia Mecânica of Universidade Federal de Uberlândia in partial fulfilment of the requirements for the degree of **DOCTOR OF PHILOSOPHY IN MECHANICAL ENGINEERING** .

Universidade Federal de Uberlândia – UFU

Faculdade de Engenharia Mecânica – FEMEC

Programa de Pós-Graduação em Engenharia Mecânica

Supervisor: Daniel Dall'Onder Dos Santos

Brasil

2024

Ficha Catalográfica Online do Sistema de Bibliotecas da UFU
com dados informados pelo(a) próprio(a) autor(a).

M672
2023

Miranda, Luiz Paulo Borges, 1991-
Numerical Simulation of the Restart Flow of Thixotropic Elastoviscoplastic Materials in Contractions and Expansions Geometries Using OpenFoam [recurso eletrônico] / Luiz Paulo Borges Miranda. - 2023.

Orientador: Daniel Dall'Onder Dos Santos.
Tese (Doutorado) - Universidade Federal de Uberlândia, Pós-graduação em Engenharia Mecânica.
Modo de acesso: Internet.
Disponível em: http://doi.org/10.14393/ufu.te.2023.619
Inclui bibliografia.
Inclui ilustrações.

1. Engenharia mecânica. I. Santos, Daniel Dall'Onder Dos,1986-, (Orient.). II. Universidade Federal de Uberlândia. Pós-graduação em Engenharia Mecânica. III. Título.

CDU: 621

Bibliotecários responsáveis pela estrutura de acordo com o AACR2:

Gizele Cristine Nunes do Couto - CRB6/2091
Nelson Marcos Ferreira - CRB6/3074

UNIVERSIDADE FEDERAL DE UBERLÂNDIA
Coordenação do Programa de Pós-Graduação em Engenharia Mecânica
Av. João Naves de Ávila, nº 2121, Bloco 1M, Sala 212 - Bairro Santa Mônica, Uberlândia-MG, CEP 38400-902
Telefone: (34) 3239-4282 - www.posmecanicaufu.com.br - secposmec@mecanica.ufu.br

ATA DE DEFESA - PÓS-GRADUAÇÃO

<table>
<tr><td>Programa de Pós-Graduação em:</td><td colspan="5">Engenharia Mecânica</td></tr>
<tr><td>Defesa de:</td><td colspan="5">Tese de Doutorado Acadêmico, nº 372, PPGEM</td></tr>
<tr><td>Data:</td><td>19/12/2023</td><td>Hora de início:</td><td>13:30</td><td>Hora de encerramento:</td><td>16:00</td></tr>
<tr><td>Matrícula do Discente:</td><td colspan="5">11923EMC008</td></tr>
<tr><td>Nome do Discente:</td><td colspan="5">Luiz Paulo Borges Miranda</td></tr>
<tr><td>Título do Trabalho:</td><td colspan="5">Numerical Simulation of the Restart Flow of Thixoelastoviscoplastic Materials in Contractions and Expansions Geometries Using OpenFoam</td></tr>
<tr><td>Área de concentração:</td><td colspan="5">Transferência de Calor e Mecânica dos Fluidos</td></tr>
<tr><td>Linha de pesquisa:</td><td colspan="5">Dinâmica dos Fluidos e Transferência de Calor</td></tr>
<tr><td>Projeto de Pesquisa de vinculação:</td><td colspan="5"></td></tr>
</table>

Reuniu-se por meio de videoconferência a Banca Examinadora, designada pelo Colegiado do Programa de Pós-graduação em Engenharia Mecânica, assim composta: Professores Doutores: João Marcelo Vedovotto - FEMEC/UFU; Francisco José de Souza - FEMEC/UFU; Flávia Schwarz Franceschini Zinani - UNISINOS; Diogo Elias da Vinha Andrade - UFRGS; e Daniel Dall'Onder dos Santos, orientador do candidato.

Iniciando os trabalhos, o presidente da mesa, Dr. Daniel Dall'Onder dos Santos, apresentou a Comissão Examinadora e o candidato, agradeceu a presença do público, e concedeu ao Discente a palavra para a exposição do seu trabalho. A duração da apresentação do Discente e o tempo de arguição e resposta foram conforme as normas do Programa.

A seguir o senhor(a) presidente concedeu a palavra, pela ordem sucessivamente, aos(às) examinadores(as), que passaram a arguir o(a) candidato(a). Ultimada a arguição, que se desenvolveu dentro dos termos regimentais, a Banca, em sessão secreta, atribuiu o resultado final, considerando o(a) candidato(a):

Aprovado.

Esta defesa faz parte dos requisitos necessários à obtenção do título de Doutor.

O competente diploma será expedido após cumprimento dos demais requisitos, conforme as normas do Programa, a legislação pertinente e a regulamentação interna da UFU.

Nada mais havendo a tratar foram encerrados os trabalhos. Foi lavrada a presente ata que após lida e achada conforme foi assinada pela Banca Examinadora.

Documento assinado eletronicamente por **Daniel Dall'Onder dos Santos**, **Professor(a) do Magistério Superior**, em 19/12/2023, às 16:01, conforme horário oficial de Brasília, com fundamento no art. 6º, § 1º, do Decreto nº 8.539, de 8 de outubro de 2015.

Documento assinado eletronicamente por **João Marcelo Vedovotto**, **Professor(a) do Magistério Superior**, em 19/12/2023, às 16:01, conforme horário oficial de Brasília, com fundamento no art. 6º, § 1º, do Decreto nº 8.539, de 8 de outubro de 2015.

Documento assinado eletronicamente por **Diogo Elias da Vinha Andrade**, **Usuário Externo**, em 19/12/2023, às 16:02, conforme horário oficial de Brasília, com fundamento no art. 6º, § 1º, do Decreto nº 8.539, de 8 de outubro de 2015.

Documento assinado eletronicamente por **Francisco José de Souza**, **Professor(a) do Magistério Superior**, em 19/12/2023, às 16:03, conforme horário oficial de Brasília, com fundamento no art. 6º, § 1º, do Decreto nº 8.539, de 8 de outubro de 2015.

Documento assinado eletronicamente por **Flávia Schwarz Franceschini Zinani**, **Usuário Externo**, em 19/12/2023, às 16:24, conforme horário oficial de Brasília, com fundamento no art. 6º, § 1º, do Decreto nº 8.539, de 8 de outubro de 2015.

A autenticidade deste documento pode ser conferida no site https://www.sei.ufu.br/sei/controlador_externo.php?acao=documento_conferir&id_orgao_acesso_externo=0, informando o código verificador **5034052** e o código CRC **91CFAE6C**.

"Ay mariposas, no se aguanten más
Hay que crecer aparte y volver
Hacia adelante seguirás
Ya son milagros, rompiendo crisálidas
Hay que volar, hay que encontrar
Su propio futuro"
(Dos oruguitas, Sebastián Yatra)

MIRANDA, L. P. B. **Numerical Simulation of the Restart Flow of Thixotropic Elastoviscoplastic Materials in Contractions and Expansions Geometries Using OpenFoam**. 2023. 124 p. PhD Thesis, Federal University of Uberlândia, Uberlândia, MG, Brazil

Abstract

The modelling of thixotropic elastoviscoplastic (TEVP) materials has made important advances in recent years, and more numerical studies are needed to validate these models. The majority of the numerical simulations found in the literature consider only one or two rheological behaviours, making it impossible to have a deeper discussion about the interaction between all three main classes of rheological behaviours. An example of the application of a TEVP material flow is the restart operation of a gelled waxy oil, where paraffin crystals are deposited, altering the rheological behaviour of the flow. In addition to the TEVP behaviour of the gelled oil, the transient nature of the restart operation increases the complexity of the flow. The present work presents an open-source tool capable of simulating TEVP materials at restart flows, analyzing how this behaviour influences the flow parameters, such as the flow velocity, the fluidity field and the time to achieve the developed flow. The adopted geometries are the 4:1 planar contraction and the 1:4 planar expansion, and the flow is considered incompressible and isothermal. At the beginning of the simulation, the flow is assumed to be fully structured, at rest, and without any internal effort. Then, a pressure gradient between the inlet and the outlet is imposed, accelerating the flow and breaking the internal structure of the material. The simulations were performed until the flow was considered at a steady-state. The results are presented in terms of the dimensionless stress field, the normalized fluidity field, the dimensionless velocities, and the time evolution of the velocity and the fluidity of some specific points of the domain. The effects of the viscoelasticity, the avalanche time, the construction time and the dimensionless imposed pressure gradient are discussed individually while the other parameters are kept constant. The results highlight the importance of considering all three rheological behaviours simultaneously: the advective transport of the unstructured material made it possible to have regions with active flow and stress lower than its yield stress, for example. Increasing the viscoelasticity increased the acceleration at the beginning of the flow, but the steady-state flow showed itself independent of the Deborah number.

Keywords: TEVP material. Thixotropy . Planar contraction. Planar Expansion.

MIRANDA, L. P. B. **Simulação Numérica da Operação de Reinicialização do escoamento de Materiais Tixo-Elastoviscoplásticos em Geometrias de Contração e Expansão Utilizando *software* OpenFOAM**. 2023. 124 p. Tese de Doutorado, Universidade Federal de Uberlândia, Uberlândia, Minas Gerais, Brasil

RESUMO

A modelagem de materiais tixo-elastoviscoplásticos (*TEVP*) apresentou avanços importantes nos últimos anos, e mais estudos numéricos são necessários para validar esses modelos. A maioria das simulações numéricas encontradas na literatura consideram apenas um ou dois comportamentos reológicos, dificultando assim uma análise mais profunda sobre como as três principais classes de comportamentos reológicos interagem entre si. Um exemplo de aplicação de um material *TEVP* é a operação de reinício de escoamento de um duto preenchido por um óleo parafínico gelificado, onde cristais de parafina são depositados, alterando o comportamento reológico do escoamento. Além da complexidade do material, a operação de reinício é por definição uma operação em regime transiente, o que aumenta as dificuldades para a simulação numérica. O presente trabalho apresenta uma ferramenta *open-source* capaz de simular escoamentos de reinício de materiais *TEVP*, analisando como o comportamento reológico influencia os parâmetros do escoamento, tais como o campo de velocidade, o campo de fluidez e o tempo para atingir o regime permanente. As geometrias adotadas são a contração planar 4:1 e a expansão planar 1:4, e o escoamento é considerado incompressível e isotérmico. No início da simulação, o material é considerado como completamente estruturado, em repouso e sem qualquer esforço interno. Então, é imposto um gradiente de pressão entre a entrada e a saída, acelerando o escoamento e quebrando a estrutura interna do material. As simulações foram executadas até que o escoamento seja considerado em regime permanente. Os resultados são apresentados em termos do campo de tensão adimensional, o campo de fluidez normalizado, o campo de velocidades adimensional, e a evolução temporal da velocidade e da fluidez de alguns pontos específicos do domínio. Os efeitos da viscoelasticidade, do tempo de avalanche, do tempo de construção e do gradiente de pressão adimensional imposto são discutidos individualmente enquanto os outros parâmetros são mantidos constantes. Os resultados destacam a importância de considerar todos os três comportamentos reológicos simultaneamente: o transporte advectivo do material desestruturado possibilitou que o escoamento apresente regiões com fluxo ativo mesmo com a tensão local inferior à sua tensão de escoamento, por exemplo. O aumento da viscoelasticidade aumentou a aceleração no início do escoamento, mas o escoamento em regime permanente mostrou-se independente do número de Deborah.

Palavras-chave: material TEVP, tixotropia. Contração planar. Expansão planar

List of Figures

List of Tables

List of abbreviations and acronyms

BSB	Both Sides Diffusion formulation
CFD	Computational Fluid Dynamics
EDIF	Explicit Diffusion formulation
EPTT	Exponential Phan-Thien-Tanner model
FVM	Finite Volume Method
FDM	Finite Difference Method
FEM	Finite Element Method
GCI	Grid Convergence Index
GNF	Generelizaed Newtonian Fluid
MBM	Modified Bautista-Manero Puig model
PISO	Pressure Implicit with Splitting of Operator
SIMPLE	Semi-Implicit Method for Pressure-Linked Equations
SPSS	Solvent-Polymer Stress Splitting formulation
TEVP	Thixotropic Elastoviscoplastic
WAT	Wax Appearance Temperature

List of symbols

a	Theoretical order of accuracy
$\mathbf{b}$	Vector containing the independent values of $\boldsymbol{\omega}^j$
CGI_{fine}^{21}	Grid Convergence Index of the meshes 2 and 1
$\mathbf{D}$	Strain rate tensor
De	Deborah number
$e_{i,ii}$	Error between the meshes i and ii
$e_{ext,i}$	error between the extrapolated value and the mesh i
h^*	Representative element length
h_n	Height of the narrow channel
h_w	Height of the wide channel
H_v	Heaviside function
j	An arbitrary time j
J	Compliance
J_0	Compliance when the material is fully structured
K	consistency index
l_c	Characteristic length
l_n	Length of the narrow channel
l_w	Length of the wide channel
$\mathbf{M}$	Matrix containing the coefficients associated with the values of $\boldsymbol{\omega}^j$ and $\boldsymbol{b}$
n	power-law index
p	Pressure
p_i	Inlet pressure
p_o	Outlet pressure

Pl	Plastic number
Q^*	Dimensionless flow rate
r_{21}	ratio between the representative element length of two meshes 1 and 2
Re	Reynolds number
s	A positive parameter of the adopted rheological model
t^*	Dimensionless time
t_c	Characteristic time
t^*_{ve}	Viscoelastic dimensionless time
t^*_a	Dimensionless avalanche time
T^*_c	Dimensionless construction time
$T^*_{c,0}$	Dimensionless construction time when the local stress is bellow the yield stress
$\mathbf{u}$	Velocity
$\mathbf{u}^*$	Dimensionless velocity
u_c	Characteristic velocity
$u_{c,ve}$	Viscoelastic characteristic velocity
u^*_x	Dimensionless horizontal velocity
$u^*_{x,ve}$	Dimensionless viscoelastic horizontal velocity
x	Horizontal position
x^*	Dimensionless horizontal position
y	Vertical position
y^*	Dimensionless vertical position
Wi	Weissenberg number
α_t	Dimensionless avalanche time constant
β	Viscosity ratio
$\boldsymbol{\gamma}$	Strain tensor

$\boldsymbol{\gamma}_e$	Elastic strain tensor
$\boldsymbol{\gamma}_v$	Viscous strain tensor
$\dot{\boldsymbol{\gamma}}$	Strain rate tensor
$\dot{\boldsymbol{\gamma}}_e$	Elastic strain rate tensor
$\dot{\boldsymbol{\gamma}}_v$	Viscous strain rate tensor
$\dot{\boldsymbol{\gamma}}_{\mathbf{1}}^{*}$	Characteristic strain rate
Δp^*	Dimensionless pressure gradient
η_0	Total viscosity
η_s	Solver viscosity
η_p	Polymer viscosity
λ_1	Relaxation time
λ_2	Retardation time
ρ	Density
τ	Stress intensity
$\boldsymbol{\tau}$	Deviatoric part of the stress tensor
τ_0	Yield stress
τ_c	Characteristic stress
τ_s	Newtonian component of $\boldsymbol{\tau}$
τ_p	Viscoelastic component of $\boldsymbol{\tau}$
τ_{xy}	Shear stress
τ^*	Dimensionless stress
ϕ_0	Fluidity when the material is fully structured
ϕ_s	Structural fluidity
ϕ_v	Fluidity
ϕ_∞	Fluidity when the material is fully unstructured
ϕ_{eq}	Equilibrium fluidity

ϕ_v^*	Normalized fluidity
ϕ_{eq}^*	Normalized equilibrium fluidity
ϕ_J^*	Reference normalized fluidity
ω	An arbitrary flow parameter
ω_{ext}	Extrapolated value of the analysed flow parameter
ω_i	Flow parameter analysed at mesh i

Contents

Part I

Theoretical references

1 INTRODUCTION

Usually, the rheological behaviours are conveniently grouped into three general classes: the 'purely viscous' behaviour, the 'time-dependent' behaviour, and the viscoelastic behaviour (CHHABRA; RICHARDSON, 1999). However, this division is purely theoretical, and a real material often presents a combination of all these three behaviours. Examples of these complex materials are widely adopted in the oil and food industry, for example. Even so, only a few studies found in the literature can discuss the interactions between all these behaviours, and the main reason for this lack of studies is the complexity of these materials.

The modelling of thixotropic elastoviscoplastic (TEVP) materials has made important advances in recent years (DE SOUZA MENDES; THOMPSON, 2019; LARSON; WEI, 2019; VARCHANIS et al., 2019), and more numerical and experimental studies are needed to validate these works. The majority of the numerical simulations found at the literature considers only one or two rheological behaviours, making it impossible to have a deeper discussion about the interaction between all the three main classes of rheological behaviours.

Another issue is that the numerical obstacles imposed by the complexity of the rheological behaviour usually leads studies to have important restrictions, such as simple geometries, for example. Thus, there is also a demand for more numerical simulations of complex flows, where the flow presents more elaborate characteristics than a viscometric flow. Once again, only a few works fount in the literature deals with these complex flows, such as the restart flow.

1.1 Motivation

Numerical works that take into account all three of these rheological behaviours are relatively rare in the literature. Hence the need to study this research branch deeply, especially because these different rheological behaviours can interact with each other, leading to flow patterns different from those observed when a smaller number of behaviours are considered. Futhermore, the transient character of the restart flow increases the difficulties and the numerical cost of the simulations, specially when a non viscometric flow is considered.

Thus, there is a demand for numerical studies that consider more complex rheological behaviours, within complex geometries and considering the trasient effects of the flow. One example of application that has these characteristics is the restart problem, where the flow starts at rest and accelerates over time, until reaching the steady-state.

1.2 Objective

The present work seeks to develop an open source tool capable to simulate TEVP materials at restart flows, analysing how the sum of these behaviours influences operating parameters, such as the pressure difference needed to re-establish the flow, the evolution of fluidity (reciprocal of viscosity) over time, and velocity profiles during operation.

The specific objectives of this thesis are:

- Implement an OpenFOAM® solver capable to solve TEVP transient incompressible flows;
- Evaluate the capacity of the solver of reproduce each rheological behaviour considered, comparing its results with carnality and semi analytical solutions;
- Evaluate the numerical uncertainties associated with the mesh adopting a transient TEVP flow inside of a 4:1 contraction and 1:4 expansion geometry;
- Identify the influence of the Deborah number over the restart flow;
- Identify the influence of the avalanche time over the restart flow;
- Identify the influence of the construction time over the restart flow;
- Identify the influence of the dimensionless pressure gradient over the restart flow.

1.3 Thesis structure

The present thesis is organized into eight chapters. The current chapter presents a brief context of subject, the main objectives and the thesis structure. Chapter 2 provides a literature review of the analysed problem, discussing the rheological aspects, the main models and similar numerical works. Chapter 3 shows a review of the main numerical methods that can be employed to solve complex flows, such as the TEVP flow. Chapter 4 presents the rheological, physical and numerical methods adopted at the present work, discussing the main reasons of each choice. The code validation and the mesh quality tests are shown in the Chapter 5. Chapter 6 presents the obtained results adopting the 1:4 expansion and the 4:1 contraction geometries. Finally, Chapter 7 summarizes the main results of the present work, and concluding the thesis.

2 LITERATURE REVIEW

The first part of this literature review presents an important application of a TEVP restart problem: the restart of a gelled waxy oil inside transport ducts. The main rheological characteristics and conditions of this application are presented and discussed. Then, a review of the experimental studies of restart flows is presented, discussing its main conclusions. The recent advances of the TEVP modelling are reviewed, followed by a review of the numerical simulations of complex materials.

2.1 Paraffin oils and the gelling process

Due to the high global demand for oil, offshore production has shown significant growth in last decades, and this expansion is even more relevant when considering production in deep waters from 1990 onwards (CHALA; SULAIMAN; JAPPER-JAAFAR, 2018), as can be seen in Figure 1. This kind of operation deals with several important technical issues due to the severe conditions to which it is exposed, such as difficulties in drilling and transporting processes.

Figure 1 – Offshore oil production.

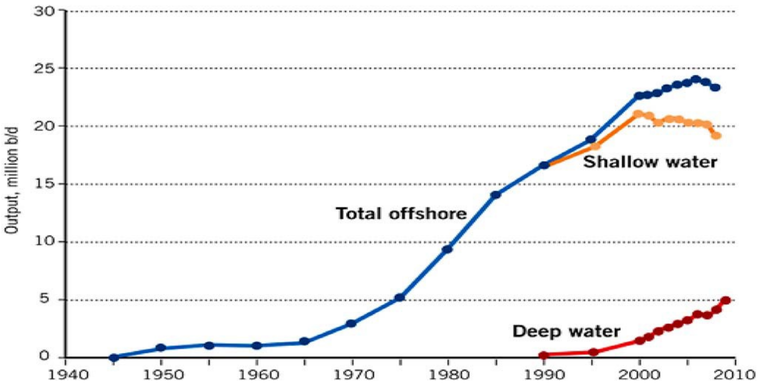

Source: Chala, Sulaiman & Japper-Jaafar (2018)

The growth of production in deep waters has increased the interest in understanding the flow of oils where paraffin crystals can be formed and deposited along the flow. This process can significantly alters the rheology of the oil, specially when a production shutdown occur (DALLA; SOARES; SIQUEIRA, 2019). At these conditions, several different rheological behaviours become more relevant, such as viscoplasticity, viscoelasticity and thixotropy (SIERRA; VARGES; RIBEIRO, 2016). This increase in flow complexity has a number of implications, increasing technical difficulties and operating costs. Due to the complex behaviour that gelled oil can present, the restart operation is considered a significant problem for oil production(VINAY; WACHS; FRIGAARD, 2007), and it is common for the estimates of the conditions necessary to carry out this operation to be overestimated (WACHS; VINAY; FRIGAARD, 2009). Several works in the literature discuss possible reasons for differences between theoretical values and those observed by the industry. Furthermore, the experimental reproduction of the conditions of the restart operation can present significant difficulties and costs, generating the demand for numerical studies about this flow (CHALA; SULAIMAN; JAPPER-JAAFAR, 2018).

Crude oil is a mixture of hydrocarbon compounds, and when more than 5% of the oil is composed by paraffins it can be considered as a waxy crude oil (ZHANG; LIU, 2008). Waxy crude oils are considered light oil, and its reserves represent about 20% of world reserves (FRIGAARD; VINAY; WACHS, 2007), about 80% of China's oil production (ZHAO et al., 2017), and a significant part of Brazilian production (CHRISMAN et al., 2019; NOVAES, 2010). Furthermore, with the decline of other oil reserves, the extraction of waxy crude oil has grown significantly. (LI et al., 2015).

One of the characteristics of a waxy crude oil is a relatively high wax appearance temperature (WAT). This temperature defines when the solubility of paraffins drops to the point of allowing their crystallization and deposition(OH; JEMMETT; DEO, 2009). Under certain conditions, such as the flow being at rest, this process can lead to the gelation of the oil, changing its rheological behaviour. This process has been studied at least since 1920s (REISTLE, 1928; REISTLE, 1932). However, with the increase in offshore production, this phenomenon has become more relevant, due to the temperature to which the seabed transport pipelines are exposed, of the order of 5°C (AZEVEDO; TEIXEIRA, 2003), and the difficulty of maintaining these pipelines. Figure 2 illustrates how the gelation process can change the rheological behaviour of the oil. Sousa et al. (2023) present a review of the economic impact of the wax deposition issue. Under laboratory conditions, concentrations as low as 1% are able to gel the oil (KANÉ et al., 2003).

The wax crystallization and deposition process are a complex phenomenon, and it is possible to find several revisions on the subject in the modern literature(AIYEJINA et al., 2011; ALI et al., 2022; ALNAIMAT; ZIAUDDIN, 2020; OLAJIRE, 2021; EL-DALATONY et al., 2019). The precipitation and deposition of waxes depend of thermodynamic variables, such as composition, pressure and temperature, and also on the flow characteristics, such as the flow hydrodynamics, heat and mass transfer, and solid–solid and surface–solid interactions (HAMMAMI; RATULOWSKI; COUTINHO, 2003). It can be found in the literature several techniques to deal with the wax deposition, such as controlling the operation conditions, mechanical methods, chemical treatments, thermal treatments, coating material, among others(ALI et al., 2022). Even though the extreme environment around seabed makes wax precipitation unavoidable(CHALA; SULAIMAN; JAPPER-

Figure 2 – Gelled oil inside a transport pipeline.

Source: Sandu & Wright (2013)

JAAFAR, 2018), some techniques can change the rheological behaviour of the gelled oil, facilitating its removal, for example(HAO; AL-SALIM; RIDZUAN, 2019; HELSPER; ALI; LIBERATORE, 2021). The Figure 3 schematically shows how the deposition of paraffin occurs inside the transport pipeline in operation below the WAT of the oil.

Figure 3 – Schematic representation of the paraffin deposition inside a low temperature transport pipeline.

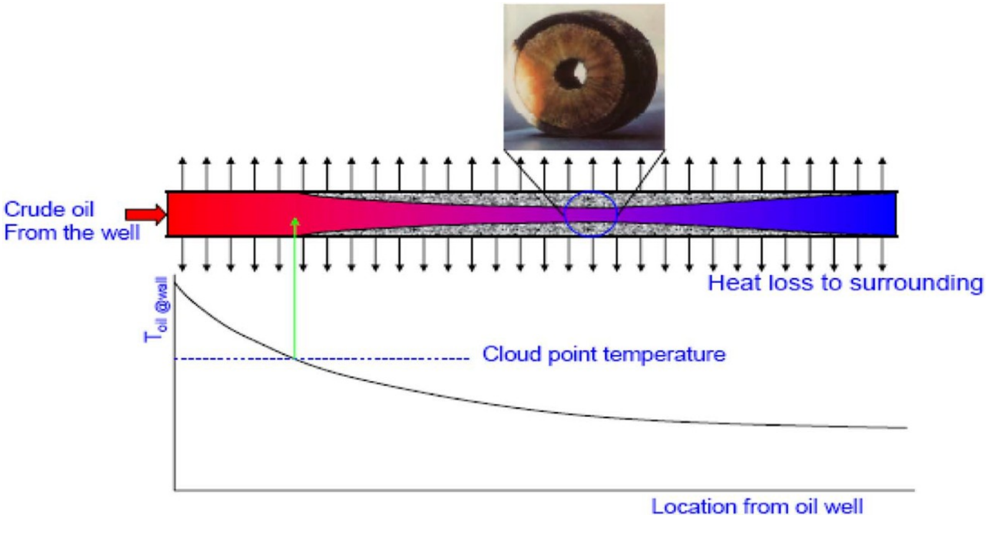

Source: Lee et al. (2008)

Seitzer & Lovell (1981) highlight that the wax deposition conditions change the wax crystal forms, thus changing its rheological behaviour. Lee et al. (2008) studied the effects of cooling rates over the gel strength, as a lower cooling rate increase the time for the wax to move within the fluid, allowing wax crystals to grow more and affecting the strength of the gel. Tinsley et al. (2009) discussed the effects of a class of compounds in crude oil, the asphaltenes, upon the crystallization behaviour of a model waxy oil. A higher concentration of asphaltenes can degrade the microscopic structure of the wax network, reducing the yield stress. Abivin, Taylor & Freed (2012) discussed the effects of the composition of thirteen oil samples, and some of the results suggests that the viscoelastic properties are linked to the asphaltene content. This demonstrates that the gel-like behaviour is also due to the associating tendency of asphaltenes that creates an elastic network within the gelled oil. Hou & Zhang (2007), Visintin et al. (2008), Legnani et al. (2020) and Karimi & Nazar (2020) analysed some factors that may affect the rheological behaviour of gelled waxy crude oil, such as temperature history, shear history, and composition, for example.

Zhapbasbayev et al. (2021) studied the effect of pour point depressants over the waxy oil dynamic viscosity and yield stress, considering the temperature dependence of these two rheological parameters. Tarcha et al. (2014) carried out experiments to verify the effect of time on the yield stress (τ_0) of crude oil. It has been observed that time has an important impact over τ_0. Moreover, the authors highlighted the importance of a critical deformation, showing that it can be a more relevant property than the yield stress itself. Andrade & Coussot (2020) stated that the rheological behaviour of wax suspensions is not only impacted by the temperature but also by the history of the temperature. The elastic modulus and the yield stress increase when the temperature is decreased, and the minimum temperature the material has experienced during its preparation can have influence over them.

Chala, Sulaiman & Japper-Jaafar (2018) presented a review of the main works on the deposition of paraffin crystals in pipelines. The authors point out that the contraction suffered by the fluid during the cool-down process has not received enough attention from the academic community, since this contraction generates nearly empty spaces inside the pipe, which may even call into question the hypothesis of a single-phase flow. A deeper analysis of this phenomenon can help to develop more efficient models to estimate the necessary pressure for the restart operation, for example. Lee et al. (2008) reported that during the waxy crude oil cool down, it can experience thermal shrinkage, and gas voids may appear, making the fluid compressible. Chala et al. (2020) analysed the behaviour of these voids when the waxy crude oil is exposed to a temperature gradient, and Chala et al. (2022) discussed the effects of the hydrostatic pressure over these voids. Shafquet et al. (2015) measured 8-14% of gas voids that were formed due to the thermal shrinkage in a waxy crude oil. Luthi (2013) stated that the ageing below pour point and the thermal shrinkage causes the appearance of gas voids close to the wall, so that the gelled crude does not get in perfect contact with it, decreasing the necessary pressure to restart the flow. Phillips et al. (2011) reported that the fluid volume shrinkage can induce shear, which in turn can reduce the pressure required to restart the flow. They have also find that the rates of shrinkage-flow have a positive correlation with the ratio of pipeline length and diameter and the cooling rate.

Sulaiman, Chala & Zainur (2019) investigated experimentally the compressibility of gelled crude oil. Different cooling rates and seabed temperatures were considered. It was observed that the specimen with higher seabed temperature and slower cooling rates showed higher compressibility tendencies.

2.2 Experimental studies on the restart operation

Abedi, Mendes & de Souza Mendes (2019) carried out an experimental study with viscoplastic fluids with and without thixotropic characteristics, aiming to better identify the relationship between the rheological properties and the minimum pressure gradient for the resumption of flow in a tube. The authors came to the conclusion that a simple balance of forces can provide a good estimate of the pressure gradient, a result that contradicts part of the literature on the subject, where the minimum gradient is typically smaller than that obtained in the balance of forces. As the study considers materials with and without thixotropic characteristics, these results suggest that the difference between the balance of forces value and the value obtained is not due to thixotropic behaviour.

Moisés et al. (2018) studied numerically and experimentally the operation of restarting the flow of viscoplastic fluids in a horizontal tube. In the experiments, a thixotropic and a non-thixotropic fluid were adopted. Numerical results managed to reproduce the main characteristics of the flow, and presented a reasonable agreement with the experimental results. The effects of thixotropy were analysed using the equilibrium time and a parameter that controls the breakdown term of the fluid structure. The increase in the equilibrium time and the decrease in the breakdown parameter caused an increase in the start-up time. Furthermore, increasing the pressure difference decreases the start-up time and increases the flow rate.

Dalla, Soares & Siqueira (2019) carried out experiments to obtain the critical stress necessary for restarting the flow of crude oil and a Carbopol solution in a pipeline. The results obtained were compared with the yield stress values obtained in a rheometer, taking into account the four main reasons that could lead to discrepancies between these two values: the thermal and stress history, the radial temperature distribution, the contraction suffered by the fluid during the cooling process and the different ways of imposing a flow of crude oil. Taking these parameters into account, the difference between the values obtained in the experiment and in the rheometer was considered small. The differences observed in the experiments with the Carbopol solution can be related to the sliding condition on the walls.

2.3 TEVP material modeling

As the name suggests, a TEVP material is characterized by three different rheological behaviours: the thixotropy, the viscoelastic and the viscoplastic behaviours. Of these three, the viscoplastic is the only time independent. Its main characteristic is the low fluidity (or high viscosity) below a certain stress, the yield stress. When a material shows a null fluidity (or infinite viscosity) under the yield stress, it is called a true yield stress material. When a material shows a small but non null fluidity under the stress field, it can be called a apparent yield stress fluid. True yield stress materials possess a strength that must be overcome by a finite stress to flow(DE SOUZA MENDES; THOMPSON, 2019).

Figure 4 – Schematic representation of the changes in the microstructure of the thixotropic material.

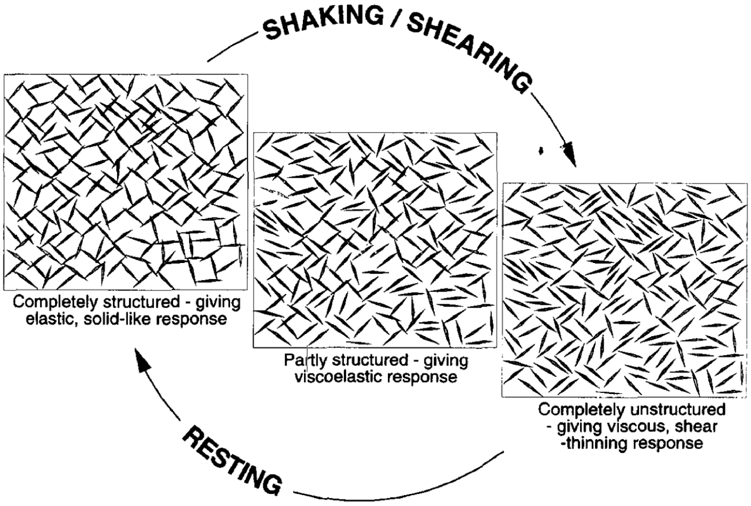

Source: Barnes (1997)

Viscoelasticity is the property of materials that can exhibit both viscous and elastic deformations when under a finite stress during a certain time. Once this stress is ceased, the elastic deformation tends to return to its initial state, while the viscous deformation is permanent. On the other hand, thixotropy is the property of materials that increases its fluidity over time when exposed to a constant stress. Usually, thixotropy is associated to the microstructure of the material, that can be broken when subjected to a finite stress. Thus, some thixotropic formulations propose a structure parameter, that tries to represent the microstructure state of the material. Usually, the structure parameter has a maximum and a minimum values, that represent the completely structured state and the completely unstructured state of the material. Figure 4 illustrates the changes in the microstructure of a thixotropic material. The more time the material is subject to a certain stress, the more its microstructure can be broken, changing its capacity to deform elastically or to resist to the stress, and consequently changing the rheological properties of the material.

Some authors adopt the shear stress step increase experiment to illustrate the differences between thixotropy and viscoelasticity. Figure 5 and Figure 6 present the results of this experiment in terms of the shear rate and apparent viscosity (η) for a purely viscoelastic response, a purely thixotropic response, and a combination of these two behaviours. Even though the definitions of thixotropy, the viscoelastic and the viscoplastic behaviours may look completely different, often it is difficult to identify and separate each one, and until today there is debate about these definitions in the literature.

Figure 5 – Shear rate ($\dot{\gamma}$) response to a step increase in shear stress experiment (a) Input: imposed step-change in shear stress; (b) a purely viscoelastic response; (c) a purely thixotropic response; and (d) thixotropic and viscoelastic response.

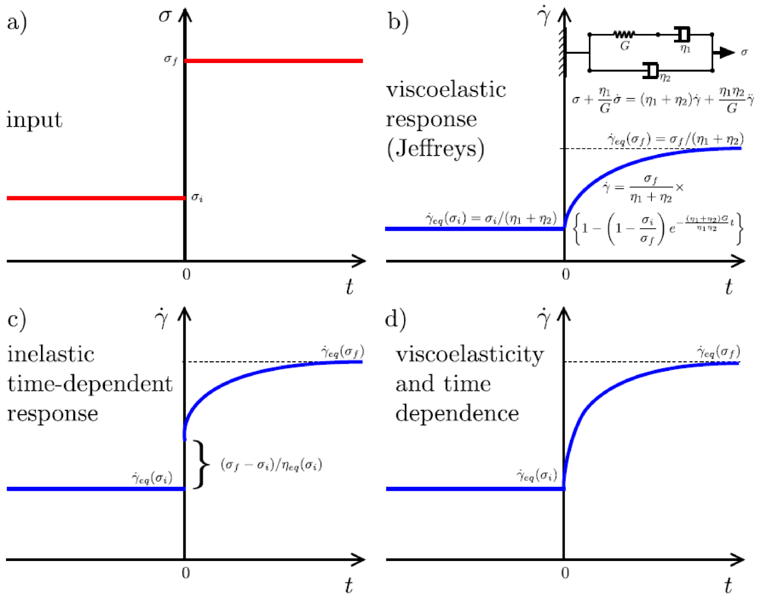

Source: de Souza Mendes & Thompson (2019)

The work of de Souza Mendes & Thompson (2012) presents a review of thixotropic elastoviscoplastic models. The different ways of modelling the behaviour of these materials were discussed, as well as their advantages and disadvantages. The mechanisms to model the structural parameters were also discussed, in order to guarantee that they describe the thixotropic behaviour. The authors show, for example, the need to adopt the structure breakage term as a function of stress, and not of strain rate. In a later work, the authors propose a TEVP model that dispenses the use of a structural parameter (DE SOUZA MENDES; ABEDI; THOMPSON, 2018).

Figure 6 – Apparent viscosity (η) response to a step increase in shear stress experiment (a) Input: imposed step-change in shear stress; (b) a purely viscoelastic response; (c) a purely thixotropic response; and (d) thixotropic and viscoelastic response.

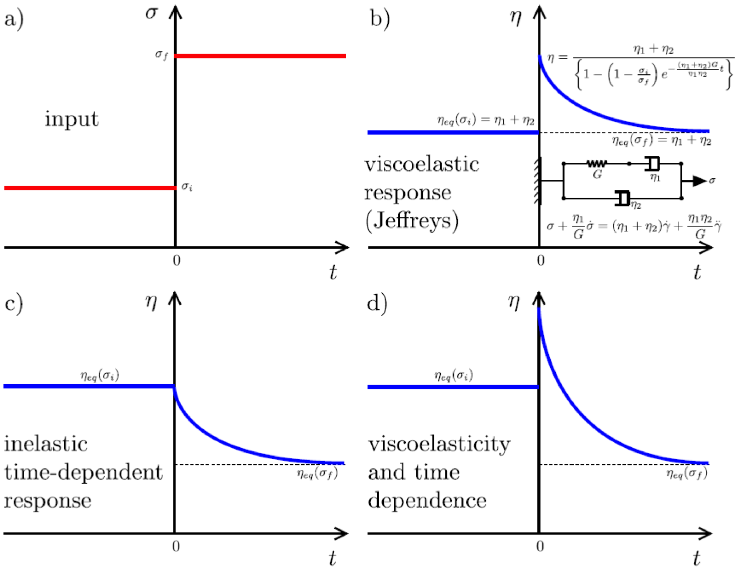

Source: de Souza Mendes & Thompson (2019)

With advances in TEVP models studies , de Souza Mendes, Abedi & Thompson (2018) proposed a method to develop models for thixo-elasto-viscoplastic fluids, adopting a tensor equation and a differential equation. The proposed model is a function of fluidity, which is the reciprocal of viscosity, that is considered as an indicator of the state of the microstructure of the fluid, which allows determining the characteristics of the construction and destruction parameters of the microstructure based on in experiments.

In a more recent work, de Souza Mendes & Thompson (2019) presented a review of the state of the art in the study of thixotropic viscoplastic materials, discussing their main characteristics and presenting recent advances in this area. According to the authors there is still much that needs to be done, even with recent advances in techniques to determine the thixotropic characteristics of fluids. Phenomena such as aging and recovery of fluids are still far from being understood, for example. Another difficulty found are the differences between the models and the real behaviour of the fluids. Furthermore, studies on more complex flows than viscometric flow are rare.

Varchanis et al. (2019) proposed a constitutive equation for TEVP fluids based on the model proposed by Saramito (2007), introducing thixotropic effects. The proposed equation models fluid aging and rejuvenation effects, as well as the anisotropic effects that can occur with these fluids. Experimental data were used to test the model in a series of flow conditions, in order to test the different rheological behaviour that can occur at the flow. To define the model parameter values, a non-linear regression method was adopted. The authors highlight the importance of extensional flows in the characterization of TEVP fluids.

Larson & Wei (2019) presented a review on thixotropic behaviour, evaluating experimental, theoretical and computational aspects. The authors highlight the recent advances in this field of study, but also point out that there are important challenges to be overcome. The authors point out a series of limitations in the literature, such as the difficulty in finding different databases to validate models, for example. Finally, the authors conclude that the highest priorities at the moment should be to obtain more data on more complex flows, both through numerical simulations and experimentally, in order to be able to evaluate the current models.

Giannokostas et al. (2020) proposed a constitutive equation to model the rheological behaviour of blood, considering it a TEVP fluid. The modelling of thixotropy and the tensor equation was proposed in order to facilitate the application of the model in more complex flows. In total, the proposed constitutive equation presents eleven elements, which were determined through a non-linear regression adopting experimental data from other works found in the literature. Then, the authors present a series of rheometric flows with the proposed model, simulating experiments in steady-state and transient state.

2.4 Numerical simulations

The simulation of the start-up flow has been studied in the literature for years, but the majority of these studies focus only in one or two different rheological behaviour. Furthermore, numerical works that deal with the simulation of the flow of thixotropic materials tends to be relatively scarce in the literature, due its complexity and the difficulty to model this behaviour.

Negrão, Franco & Rocha (2011) presented the results of a one-dimensional mathematical model to solve the equations of mass balance and linear motion of a transient flow of a TEVP compressible fluid. The results were compared with results from a Newtonian fluid, a Bingham fluid and a viscoplastic fluid. The main differences between the TEVP and the viscoplastic models occur at low strain rates. Another important result is that peak pressure for thixotropic fluids is not always greater than its Newtonian equivalent, for example.

Jahromi et al. (2011) compared the response of a modified Bautista-Manero Puig (MBM) model (BAUTISTA et al., 1999; BOEK et al., 2005) and a shear-thinning exponential Phan-Thien-Tanner (EPTT) model(THIEN; TANNER, 1977) in planar 4:1 rounded-corner contraction flow. The modified Bautista-Manero Puig model has a kinetic equation for the reciprocal of the viscosity and can predict thixotropy and viscoelasticity, and in some cases can incorporate plasticity too(CALDERAS et al., 2013), although the authors decided to focus on the first two behaviours. The simulations were performed assuming that the inertia effects are negligible, with solvent/total viscosity ratio of 1/9, and zero shear viscosity of 8/9, and two different flow conditions were adopted: a strong-hardening regime and a moderate hardening regime. The results are presented in terms of the evolution in vortex characteristics, stress and viscosity fields. Comparing the results of simulations, the authors highlight that there are significant differences observed at We= 1 in the transient development of velocity, stress, pressure and viscosity profiles around the contraction zone for the MBM moderate hardening regime flow against that of EPTT, while larger elasticity levels of We= 2 are required for the strong-hardening MBM flow to detect differences in transient vortex structure development over its EPTT counterpart.

Cheddadi, Saramito & Graner (2012) solved numerically a cylindrical Couette flow considering an elasto-viscoplastic fluid, adopting a tensor model. Then, the results were compared with experimental results. The different rheological behaviours interact with each other, so that a viscoplastic or viscoelastic model can not present the same behaviour of an elasto-viscoplastic flow. Furthermore, the authors identified that the steady-state flow under these conditions is not unique: it depends on the initial conditions of the stress tensor.

Sargentini (2013) adopted the software OpenFOAM® to perform simulations of the flow of a viscoplastic fluid modelled by the Bingham function, where the effect of temperature on several rheological parameters was considered. The author concludes that the conditions for the resumption of flow do not depend only on the pressure difference, but also on the local temperature. Furthermore, the pressure difference required for the restart operation is higher than the pressure difference to maintain the flow once it reaches steady-state.

López-Aguilar et al. (2015) simulated steady-state flows of TEVP materials over a 4:1:4 axisymmetric, rounded-corner contraction followed by an expansion geometry. Two models were adopted: a Bingham–Papanastasiou model adapted model, and a new micellar thixotropic constitutive model (LÓPEZ-AGUILAR et al., 2014) that has a non-linear differential equation for the fluidity, to represent the structure of the fluid. Considering elastic and plastic influences separately, the authors evaluated the influence of the yield stress, the regularization stress growth exponent, the polymeric concentration, and the thixotropic destruction parameter. The results were presented in terms of flow field features, such as vortex dynamics, stress field structure, yield front patterns and enhanced pressure drop. Vortex intensity and size are observed to sharply reduce with increasing yield stress and elasticity levels. Different yield front patterns were observed, including asymmetric patterns, depending of the combination combinations of these behaviours.

Link et al. (2015) performed a numerical investigation of an elasto-viscoplastic thixotropic fluid flowing through a 1:4 plane expansion, assuming an inertialess steady flow of an incompressible structured fluid. The adopted model was proposed by Mendes (2011) and is based on the upper-convected Oldroyd-B constitutive equation, modified to include the influence of the structure parameter over the shear modulus, the relaxation time and the viscosity. The authors observed that, for the analysed range of parameters, elasticity tends to inhibit yielding, which can change significantly the flow pattern and the shape and size of the unyielded regions.

The work of Oishi, Thompson & Martins (2016) may be the first published work that captures the transient motions of TEVP materials. To represent the apparent-yield-stress nature of the complex materials considered, a Bingham model with a bi-viscosity regularization method was employed. In a first moment, the authors analysed the plane channel flow subjected to a constant pressure gradient. The TEVP material is considered stationary and fully structured at the beginning of the numerical simulation, and the pressure gradient accelerates the flow until it arrives at the fully developed flow condition. The effects of the thixotropic equilibrium time, yields stress, and Weissenberg number were illustrated with the structure parameter profile over a cross section of the planar channel. Then, a more complex problem is analysed, where a block made by a TEVP material initially at fully-structured square shape is subjected to the action of gravity. The stress imposed by the gravity force is able to provoke the break down process of the block, changing its form. Three dimensionless quantities were varied: Weissenberg number, dimensionless yield stress, and dimensionless thixotropic equilibrium time. The work presents several images illustrating how these parameters interact with each other, showing how complex the transient motions of TEVP materials can be. For the analysed range of parameters, the time scale associated to the elastic response of the material is faster than the characteristic times scale associated to other behaviours.

In a later work, Oishi, Martins & Thompson (2017) adopted as an initial configuration a trapezoidal block on an inclined plane, considering that the block is constituted by a TEVP material. Several parameters were varied by the authors, such as the equilibrium time, the plastic number, the Weissenberg number, and other rheological parameters. The authors identified the “avalanche effect” in all simulations. Even though the yield stress, evaluated by the plastic number, was the most relevant property associated with the evolution of the material flow over the inclined plane, other rheological parameters had significant influence over the process, highlighting the importance to consider the interaction between different rheological behaviours. Another important conclusion is that increasing elasticity can allow a higher deformation of the material without decreasing the structure parameter.

Cunha, de Souza Mendes & Siqueira (2020) analysed flows of thixotropic viscoplastic fluids inside pipelines, considering the transient regime. Both completely structured and completely unstructured initial conditions were adopted, as well as different plastic numbers. When the fluid begins the simulation completely structured, it is possible to observe that the flow intensifies rapidly after the microstructure breaks, which represents the avalanche effect. On the other hand, when the initial condition is the completely unstructured fluid, the fluidity field may present a discontinuity due to the viscoplastic characteristics of the fluid. As the adopted fluid does not present viscoelastic characteristics, the steady-state flow does not depend on the initial condition of the flow.

Siqueira, Pasquali & de Souza Mendes (2020) presented a theoretical and numerical study of a Couette flow between concentric cylinders, adopting a thixotropic viscoplastic behaviour for the fluid. The study explores the influence of the initial conditions and the imposed stress on the flow evolution, and reveals that thixotropic viscoplastic materials present a permanent regime that is independent of the initial conditions. This result contrasts with the results presented by Cheddadi, Saramito & Graner (2012), which adopts an elasto-viscoplastic fluid, without thixotropic behaviour.

Bao & Zhang (2020) presents a numerical study on the restart behaviour of gelled waxy crude oil pipelines using an elasto-viscoplastic thixotropic model. The study aims to understand the flow characteristics and predict the restart process of the pipeline after a shutdown. By numerical simulations, the study provides insights into the transient flow behaviour, pressure distribution, and wall shear stress during pipeline restart operations, contributing to the understanding of pipeline operations and potential mitigation strategies for challenges associated with gelled crude oil transportation. The authors adopted a modified Dullaert-Mewis model (DULLAERT; MEWIS, 2006) to perform numerical simulations of pipeline restart and evaluate the effects of compressibility, Reynolds number, yield stress number and structural breakdown rate. Then, the effect of viscoelasticity on pipeline restart was analysed by comparing the pipeline restart predictions obtained with the proposed model and the Teng's model (TENG; ZHANG, 2013), that do not account the viscoelasticity. The simulations were done adopting an axisymmetric channel geometry, and the waxy gel is assumed to be stationary and fully structured prior to restart. At the begining of the simulation, a pressure gradient is imposed between the inlet and the outlet of the domain, and this pressure gradient works as the driving force of the flow, accelerating it until it achieves the fully developed flow state. The flow conditions, such as the adopted geometry, allowed the authors to adopt a linear distribution of shear stress along the radial direction, reducing numerical obstacles. Among other conclusions, the authors have found that as the compressibility of gelled waxy crude oil increases, the restart time and steady-state velocity at the same restart pressure increases and the minimum required pressure difference for successful restart decreases. When viscoelasticity of gelled waxy crude oil is considered, the restart time and the calculated minimum required pressure gradient for restart decreases.

Sánchez et al. (2022) implement a modified version of the Bautista-Manero Puig model using the toolbox RheoTool(PIMENTA; ALVES, 2017), developed with the software OpenFOAM®, and adopted it to solve simulations in two different geometries: the contraction 4:1 and the contraction followed by an expansion 4:1:4. They analysed the effects of the inertia, the viscoelasticity and the thixotropic behaviour over some of the flow parameters, like the velocity, the normal stresses and the corner vortexes. In a similar way to Jahromi et al. (2011), the authors adopted two different flow conditions: one with a relatively quick structural recovery and another with a slightly slow structural recovery. These two cases where simulated using different values of Reynolds number and Deborah number, and their effect over the corner vortexes are shown, both in the transient and in the steady-state.

It is important to highlight that of all the works discussed in this section, only Oishi, Thompson & Martins (2016) and Oishi, Martins & Thompson (2017) present a fully numerical simulation of the transient TEVP flows. López-Aguilar et al. (2015) and Link et al. (2015) adopt a TEVP model, but they consider only the steady-state flow. Negrão, Franco & Rocha (2011), Siqueira, Pasquali & de Souza Mendes (2020), Cunha, de Souza Mendes & Siqueira (2020) and Bao & Zhang (2020) assume an analytic solution of their stress profile, decreasing the numerical costs. Jahromi et al. (2011) and Sánchez et al. (2022) only considered thixotropic viscoelastic behaviours, while Cheddadi, Saramito & Graner (2012) only considered elastoviscoplastic flows. These results show the scarcity of works discussing the transient effects of a complex flow.

3 NUMERICAL METHOD

Computational fluid dynamics (CFD) is a branch of fluid mechanics that uses numerical methods to solve the governing equations of problems that involve fluid flows. The two main governing equations are the balance equations of mass and momentum, but different problems can have different formulations of these two equations, and others governing equations can be added, or even subtracted, to the mechanical model. A non-isothermal problem, for example, may need to solve the energy balance equation. Thus, there is no perfect method or formulation, and each individual problem must be analysed individually to determine the best configuration for its solution. This chapter presents and discuss the main characteristics of the numerical method adopted, justifying the author choices.

The mathematical model for the transient, incompressible and isothermal flow of a TEVP material consists of four equations: the balance equation of mass, the balance equation of momentum, the stress equation and the evolution equation for the fluidity (ϕ). The numerical method must solve all these equations simultaneously, converging to the solution, reducing errors and being as stable as possible.

3.1 Discretization method

The discretization method defines how the solver algorithm will obtain a system of equations that approximate the differential equations in a discrete set of points in time and space. The main discretization methods are the finite difference method (FDM), finite volume method (FVM) and finite element method (FEM). In addition to these methods, it is possible to find hybrid methods. Although some methods are more suitable for certain types of problems, in a sufficiently fine mesh and with the appropriate parameters, all methods should converge to the same result.

3.1.1 Finite difference method

The finite difference method (FDM) is the oldest method for the numerical solution of partial differential equations, and it can also be considered the easiest method to apply to simple geometries. This method solves the conservation equations in its differential form: the differential equation is approximated at each mesh node, replacing the partial derivatives with approximations defined as a function of the values of neighbouring nodes. Thus, an equation is obtained per grid node, relating the values of each node with the values of neighboring nodes. Usually, the FDM can not be applied on more complex meshes, and it is only applied to simpler geometries, but there are exceptions. The work of Oishi, Thompson & Martins (2016) applied a FDM scheme to solve a free surface problem, adopting a TEVP material properties.

3.1.2 Finite volume method

In the finite volume method (FVM) , the mesh is discretized into a finite set of control volumes, and the balance equations are integrated over these volumes. Then, all the equation terms are written as functions of the properties values at the centroid of the control volume. To obtain the properties values at the surfaces of the control volume, an interpolation scheme is applied. The FVM has two main advantages over the finite difference method: the finite volume method can be applied to any type of mesh, which allows the application of this method to flows with more complex geometries, and it guarantees the conservation of its properties, since conservation is guaranteed in each of the control volumes, and thus, when adding all the control volumes that make up the geometric domain, conservation is guaranteed in the mesh as a whole (PATANKAR, 1980).

3.1.3 Finite element method

The finite element method also uses a set of discrete volumes, just like the finite volume method. However, in the finite element method, the property values are calculated at the mesh nodes, and an approximation function is used to obtain the values inside the element. To obtain the coefficients of this approximation function, a weight function is used. The most attractive characteristic of the FEM is its ability to handle complex geometries with relative ease. However, the more complex the mesh, the more difficult it is to solve the algebraic system associated with it, which can decrease the efficiency of the method. In structural mechanics analysis, the FEM method is the most used method in simulations. The work of Link et al. (2015) adopts the FEM.

3.1.4 Hybrid methods

As the name suggests, hybrid methods mix different methods features, aiming to have the best of each method. These methods can be developed for specific problem classes, and they are not as common in the literature as the FVM and the FEM. López-Aguilar et al. (2015) adopts an hybrid method, mixing characteristics of the FEM and FVM.

3.2 Solution Methods

The mathematical systems usually have at least two differential equations, like the momentum balance equation and the mass balance equation for an incompressible flow. As can be seen in Equation 3.1, the solution of each equation depends of the solution of the others equations of the system, thus all equations must converge to the solution simultaneously. To achieve this, several strategies can be applied, and usually these strategies are divided between implicit/explicit methods, and between segregated/coupled methods.

$$\begin{aligned} &\nabla \cdot \mathbf{u} = 0 \\ &\rho \frac{\partial \mathbf{u}}{\partial t} + \rho \left(\nabla \mathbf{u} \right) \mathbf{u} = -\nabla p + \nabla \cdot \ \boldsymbol{\tau} \end{aligned} \tag{3.1}$$

where $\mathbf{u}$ is the velocity, ρ is the material density, p is the pressure and $\boldsymbol{\tau}$ is the deviatoric part of the stress tensor.

3.2.1 Implicit methods

In implicit methods, equations are solved using not only values from the previous iteration, but from the iteration itself as well. Thus, the equations are solved simultaneously. Implicit methods are unconditionally stable and require fewer iterations to obtain a solution, but require more computer memory to solve. Fig. 7 represents an implicit method, where the variables from time *j* are calculated using other values from time *j* and values from time *j-1*.

Figure 7 – Schematic representation of an implicit method.

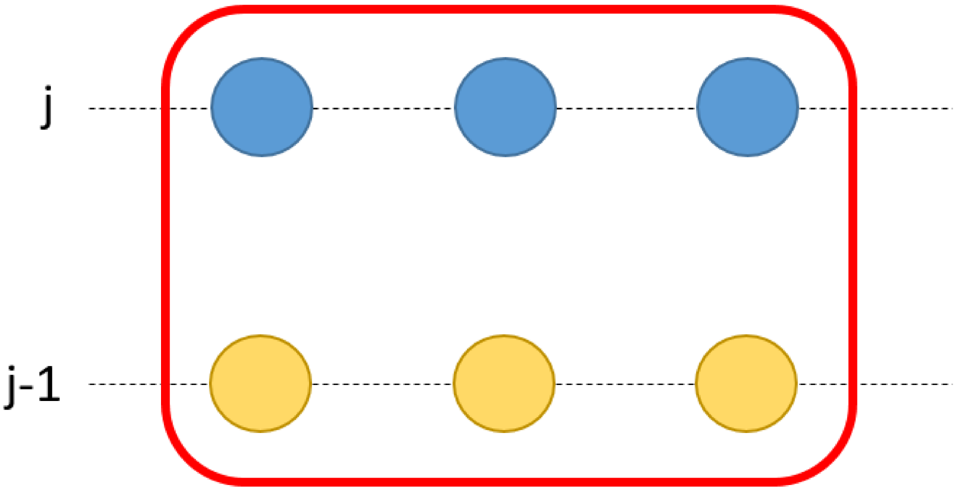

After been discretized and linearised, the equations, like Equation 3.1, assumes the following form:

$$\mathbf{M}\boldsymbol{\omega}^{j} = \mathbf{b} \tag{3.2}$$

where $\boldsymbol{\omega}^j$ is the vector containing the values of an arbitrary property $\boldsymbol{\omega}$ of the flow, defined at a specific point of the mesh and at the time *j*. $\boldsymbol{M}$ contains the coefficients associated with the values of $\boldsymbol{\omega}^j$ and $\boldsymbol{b}$ is a vector with the values independent of $\boldsymbol{\omega}^j$. $\boldsymbol{M}$ is a square matrix, and each of the rows of $\boldsymbol{\omega}^j$, $\boldsymbol{M}$ and $\boldsymbol{b}$ represent the one of the governing equations applied to a specific point of the mesh, that can be the centroid of a volume or a node of the mesh, for example, depending of the discretization method. It is interesting to the matrix $\boldsymbol{M}$ to be diagonally dominant, since it is necessary to invert it to obtain the vector $\boldsymbol{\omega}^j$. This is one of the reasons why the orthogonality of a mesh is a relevant feature of the system.

3.2.2 Explicit methods

In explicit methods $\boldsymbol{\omega}^j$ is calculated using only the values from the previous known time. In this way, the equation for each point can be solved individually. Explicit methods may not have their stability guaranteed and require a greater number of iterations, which usually means a longer simulation time. Figure 8 illustrates an explicit method, where each of the variables of the time *j* only depends on the values of the time *j-1*. Explicit methods are conditionally stable, that means that they are stable only under certain conditions and the time step in explicit methods are usually smaller than the time step in implicit methods. On the other hand, explicit methods are simpler to implement and demand less numerical resources when compared to implicit methods.

Figure 8 – Schematic representation of an explicit method.

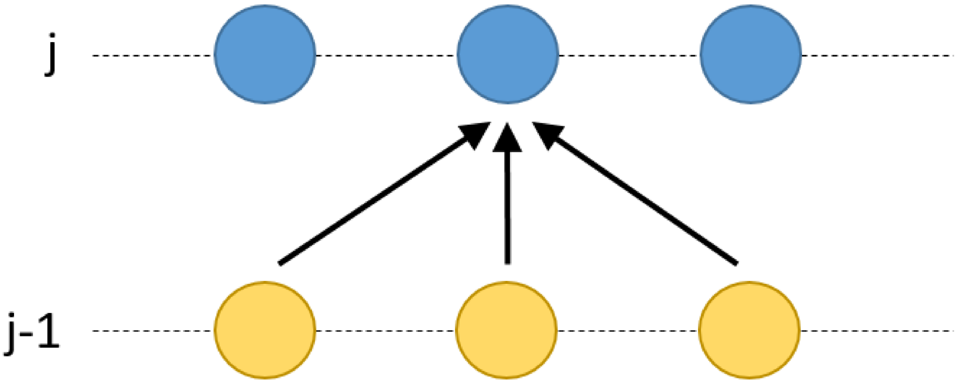

3.2.3 Coupled methods

The coupled methods solve all equations of the mathematical model simultaneously, easing the interaction between different equations at cost of increasing the size of the matrices involved, which increases the numerical difficulties. This way, coupled methods usually requires less interactions to solve the system and are more stable than segregated methods. These characteristics make coupled methods specially suited for transient simulations(PIMENTA; ALVES, 2019).

3.2.4 Segregated methods

As the mathematical model can contain several different equations, the segregated methods solve each equation in sequence. This way the equations can be solved individually, decreasing the size of the associated matrix, reducing the numerical cost of these operations. On the other hand, the segregated methods can demand a larger number of iterations to obtain the solution, as the system as a whole must be solved and the equations can interact with each other. They are also less stable, when compared to coupled methods.

To bypass these obstacles, some methods try to couple different equations, increasing the accuracy and stability of these algorithms. The main category of these algorithms are the pressure-correction algorithms, where an intermediate velocity field is adopted to solve the mass balance equation, and then the velocity field is corrected using the new pressure field.

3.2.4.1 SIMPLE

The SIMPLE algorithm is a pressure-correction algorithm proposed by Patankar & Spalding (1972) in the early 1970s. Figure 9 shows the flowchart of the SIMPLE algorithm implemented by default at OpenFOAM®, where this algorithm is used to solve steady-state simulations. In the literature it is possible to find variations of this algorithm, like the SIMPLEC algorithm(DOORMAAL; RAITHBY, 1984), that is also implemented by default at OpenFOAM®.

As can be seen in Figure 9, the first equation solved at the SIMPLE algorithm is the momentum predictor, adopting the pressure values calculated at the previous iteration. Then, the pressure equation is solved, using the velocity field calculated with the momentum predictor. This pressure equation is the Poisson equation for pressure, and it is equivalent to the mass balance equation. Then, the velocity field is corrected, adopting the new pressure field calculates at the previous step.

3.2.4.2 PISO

The PISO algorithm was proposed by Issa (1986) and its algorithm splits the operators into an implicit predictor and multiple explicit corrector steps, hence its name: PISO stands for Pressure Implicit with Splitting of Operator. Figure 10 shows the flowchart of the PISO algorithm implemented by default at OpenFOAM®, where the multiple explicit corrector steps previously mentioned are identified as the “PISO loop”. It was originally

Figure 9 – Schematic representation of SIMPLE algorithm.

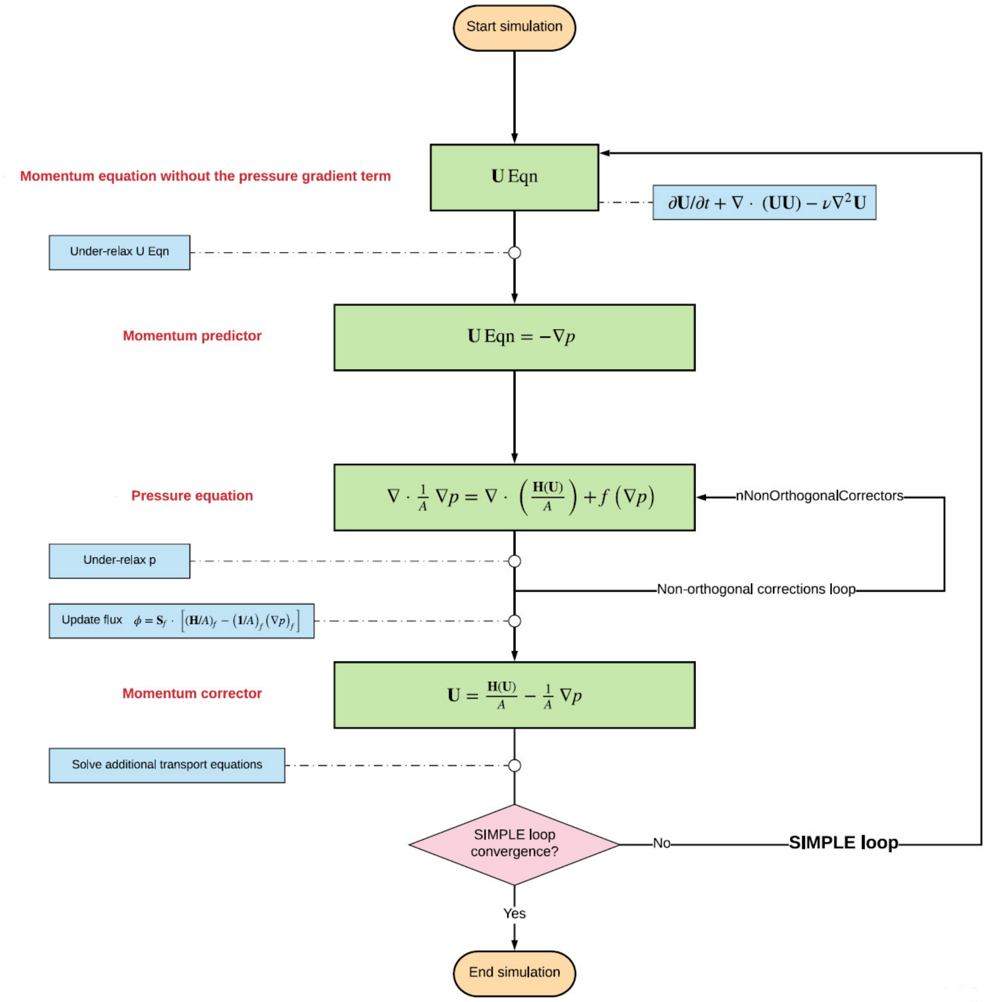

Source: adapted from Guerrero (2018)

developed to solve unsteady flows, and the PISO algorithm implemented by default at OpenFOAM® kept this feature, even though it is possible to find adaptations of this algorithm to successfully solve steady-state problems. Another important feature is that, after performing the defined number of corrections, the algorithm follows to the next time step, without evaluating if the solution has converged.

3.2.4.3 PIMPLE

The PIMPLE algorithm can be seen as a modification of the PISO algorithm to incorporate some SIMPLE algorithm features. As can be seen in Figure 11, the PIMPLE algorithm has both the SIMPLE loop and the PISO loop and it is equivalent to PISO when the number of outer iterations is equal to the unity. When more than one outer iterations are performed, the algorithm verify the solution convergence, allowing to improve the accuracy and the efficiency of the solver simultaneously. The PIMPLE algorithm can be

Figure 10 – Schematic representation of PISO algorithm.

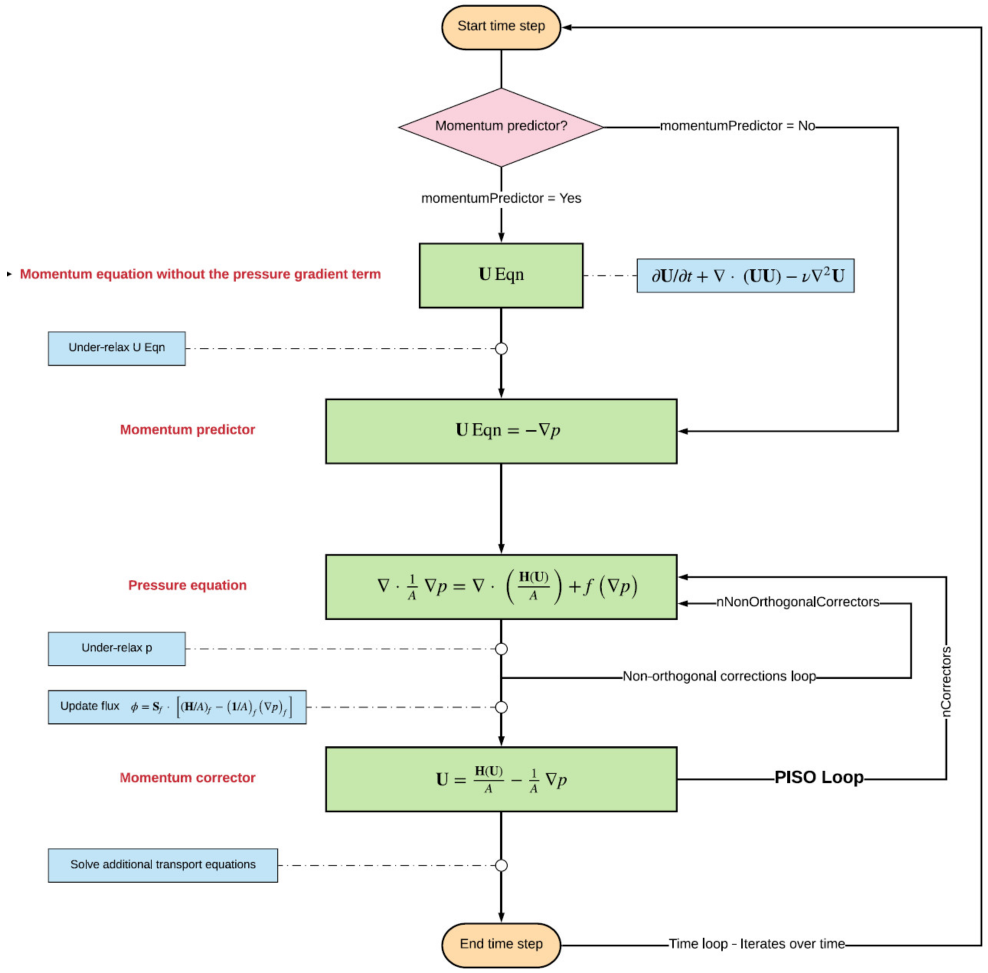

Source: adapted from Guerrero (2018)

used to solve transient and steady-state problems and usually allows bigger time steps when compared to the PISO algorithm. The PIMPLE algorithm can also be called PISO with iterative marching.

3.3 OpenFOAM

OpenFOAM® is a free, open source CFD software written in C++ language and it follows object-oriented programming, allowing a high customization capacity. These features make OpenFOAM® one of the most used CFD software. Its standard routines uses the finite volume method to solve several engineering problems, such as complex fluid flows, chemical reactions, turbulence and heat transfer, for example. Regarding the complex fluid flows, OpenFOAM® standard routines can solve generalized Newtonian fluid (GNF) unsteady flows, viscoelastic flows, and, more recently, thixotropic flows.

Figure 11 – Schematic representation of PIMPLE algorithm.

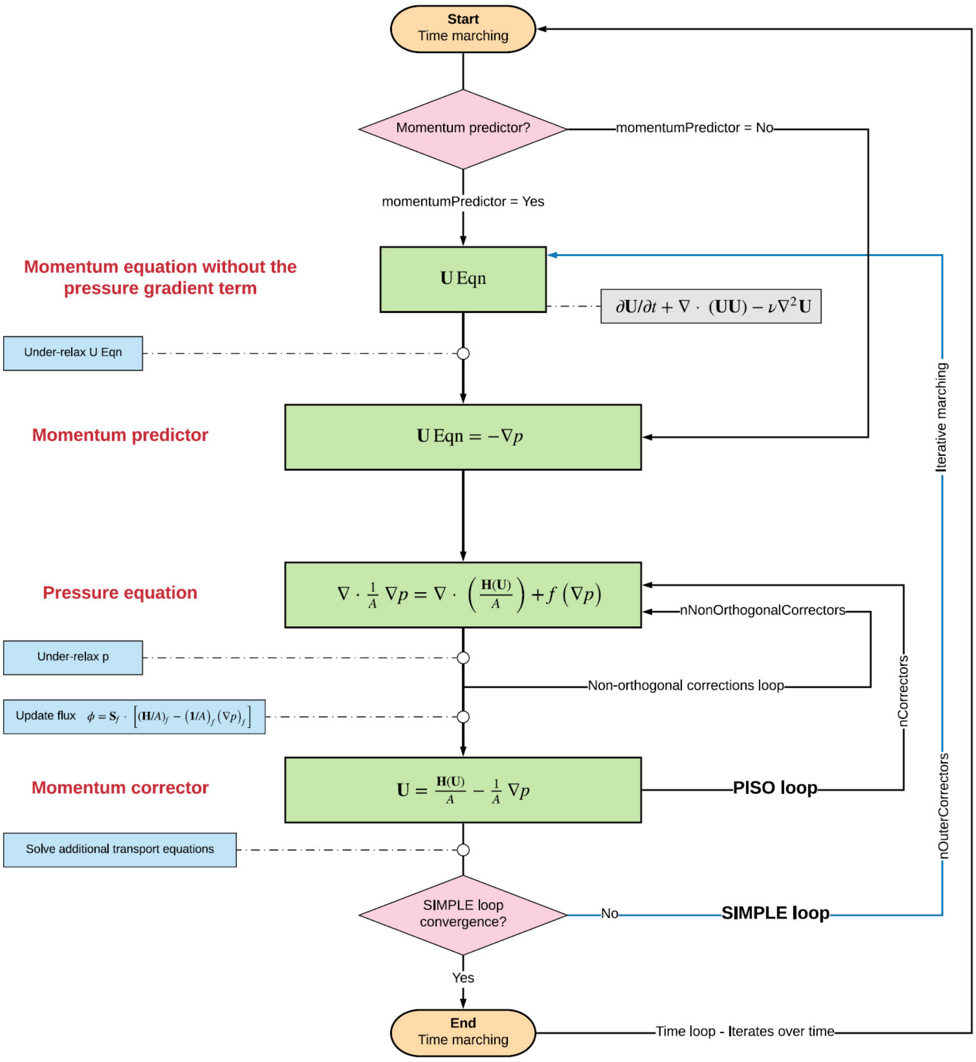

Source: adapted from Guerrero (2018)

3.3.1 RheoTool

RheoTool is an open-source toolbox for OpenFOAM® focused to simulate GNF and viscoelastic fluids under pressure-driven and/or electrically-driven flows. Its standard routines offers several models, solvers and tools to help solving complex fluid flows. Such features include, but are not limited to: coupled solvers, an interface with external sparse matrix solvers, non-isothermal flows solver, and a log-conformation tensor approach routine for viscoelastic flows.

3.4 Stress split

A common strategy to deal with viscoelastic flows is splitting the stress tensor in two terms: a viscoelastic component and a Newtonian component. This transformation contribute to the numerical solution of the flow, as each component can be treated accordingly to its particularities. Adopting a constitutive equation based on the Oldroyd-B model(OLDROYD, 1950), with the following form:

$$\boldsymbol{\tau} + \lambda_1 \overset{\triangledown}{\boldsymbol{\tau}} = 2\eta_0 \left(\mathbf{D} + \lambda_2 \overset{\triangledown}{\mathbf{D}} \right) \tag{3.3}$$

where λ_1 is the relaxation time; λ_2 is the retardation time; $\overset{\triangledown}{\boldsymbol{\tau}}$ is the upper-convected time derivative of stress tensor; η_0 is the total viscosity; $\mathbf{D}$ is the deformation rate tensor. The expressions for λ_2, $\mathbf{D}$ and $\overset{\triangledown}{\boldsymbol{\tau}}$ are:

$$\begin{aligned} \lambda_2 &= \frac{\lambda_1 \eta_s}{\eta_0} \\ \mathbf{D} &= \frac{1}{2}\left[\nabla \mathbf{u} + (\nabla \mathbf{u})^T\right] \\ \overset{\triangledown}{\boldsymbol{\tau}} &= \frac{\partial \boldsymbol{\tau}}{\partial t} + \mathbf{u} \cdot \nabla \boldsymbol{\tau} - \left[(\nabla \mathbf{u})^T \cdot \boldsymbol{\tau} + \boldsymbol{\tau} \cdot (\nabla \mathbf{u})\right] \end{aligned} \tag{3.4}$$

where η_s is the Newtonian component of η_0. Splitting $\boldsymbol{\tau}$ into its viscoelastic component ($\boldsymbol{\tau}_p$) and its Newtonian component ($\boldsymbol{\tau}_s$) and applying these conditions to the constitutive equation (Equation 3.3), the result is:

$$\begin{aligned} \boldsymbol{\tau} &= \boldsymbol{\tau}_s + \boldsymbol{\tau}_p \\ \boldsymbol{\tau}_s &= 2\eta_s \mathbf{D} \\ \boldsymbol{\tau}_p + \lambda_1 \overset{\triangledown}{\boldsymbol{\tau}}_p &= 2\eta_p \mathbf{D} \end{aligned} \tag{3.5}$$

where η_p is the viscoelastic contribution of η_0. Usually, the viscoelastic component is associated with the polymer, hence the subscribed "p" at η_p, and the Newtonian component is associated with the solvent, explaining the subscribed "s" at η_s and τ_s. Equation 3.5 is simpler to numerically solve than Equation 3.3, even though they are analytically equivalent. Equation 3.5 also allows to deal with each component individually, increasing the stability of the algorithm.

3.5 Log conformation

The log-conformation tensor methodology (FATTAL; KUPFERMAN, 2004) can minimize the numerical instabilities frequently observed for high Weissenberg number flows. This methodology proposes to substitute the stress in Equation 3.3 by another variable, in such a way that with this transformation, the extensional components of the deformation field act additively, rather than multiplicatively. But there are some restrictions to be able to perform this transformation, specially when non constant properties are considered. If λ_1 and η_p are not considered as constants (adopting that they can vary with the strain rate, for example), then the ratio $\frac{\lambda_1}{\eta_p}$ must be constant.

Another issue of this methodology is that it was proposed for viscoelastic flows, and Oishi, Thompson & Martins (2016) declared that, at their TEVP flow simulations, the time scale associated to the elastic response of the material is faster than the characteristic times scale associated to other behaviours. Thus, it is expected that this methodology may not be as efficient for TEVP flows as it is for viscoelastic flows.

3.6 Viscoelastic stabilization methods

As can be seen in Equation 3.3, the constitutive equation of the Oldroyd-B model lacks an explicit diffusive term, and this characteristic increases the instability of the solution, increasing its difficulty and even making it impossible some times. A possible solution for this problem is to include diffusive terms in the equations, splitting the stress tensor into different components or even adding and subtracting a diffusive term. All these manipulations are analytically equivalent to the Oldroyd-B model, but at numerical routines they use different strategies to obtain the solution. The work of Amoreira & Oliveira (2010) discuss the efficiency of these different strategies. The most relevant formulations found in the literature are:

- Original formulation: the original formulation is the Equation 3.3 and Equation 3.1, without any transformation or manipulation. This formulation is unstable and there are no relevant reason to prefer it over any other formulation(AMOREIRA; OLIVEIRA, 2010).

- Solvent-polymer stress splitting (SPSS)(DUARTE; MIRANDA; OLIVEIRA, 2008): This formulation adopts the stress split shown in Section 3.4 and has some physical background as a viscoelastic fluid is often composed by an elastic polymeric solute in a Newtonian solvent. This formulation is the most efficient according to the work of Amoreira & Oliveira (2010), and it is part of the RheoTool standard library, as the “none” stabilization method. The formulation of this method is composed by Equation 3.5 and the Equation 3.1 with the following modification:

$$\nabla \cdot \boldsymbol{\tau} = \eta_s \nabla^2 \mathbf{u} + \{\nabla \cdot \boldsymbol{\tau}_p\} \tag{3.6}$$

- Explicit diffusion (EDIF)(GUéNETTE; FORTIN, 1995): This formulation also adopts the stress split shown in Section 3.4, but it add and subtract a diffusive term, seeking to increase its influence over the solution and stabilizing it. This technique is purely numeric, so there is no physical background to support it. The work of Amoreira & Oliveira (2010) showed that this formulation usually need more interactions than the SPSS technique to solve the same problem. This formulation can also be called the "both sides diffusion" (BSD) and it is part of the Rheotool standard library. The formulation of this method is composed by Equation 3.5 and the Equation 3.1 with the following modification:

$$\nabla \cdot \boldsymbol{\tau} = (\eta_p + \eta_s)\,\nabla^2 \mathbf{u} + \left\{\nabla \cdot \boldsymbol{\tau}_p - \eta_p \nabla^2 \mathbf{u}\right\} \tag{3.7}$$

- RheoTool User manual(PIMENTA, 2022) shows an adaptation of the BSD method and call it "coupling method"(PIMENTA; ALVES, 2017). This method is recommended for most of the cases by the RheoTool User manual(PIMENTA, 2022), but the formulation that is implemented at the toolbox is only suitable to solve constitutive equations where η_p is constant. When η_p is not constant, a new term must be added, which decrease the efficiency of this method, matching it to the EDIF method efficiency. Equation 3.8 shows how this method is implemented at RheoTool. The formulation of this method is composed by Equation 3.5 and the Equation 3.1 with the following modification:

$$\nabla \cdot \boldsymbol{\tau} = (\eta_p + \eta_s)\,\nabla^2 \mathbf{u} + \{\nabla \cdot \boldsymbol{\tau}_p - \nabla \cdot (\eta_p \nabla \mathbf{u})\} \tag{3.8}$$

In Equation 3.6, Equation 3.7, and Equation 3.8 the curly brackets are used to group the terms that are to be treated as explicit source terms. The choice of the formulation has direct impact over the efficiency and the stability of the algorithm, and there is no perfect solution. It is possible to find more formulations in the literature, but usually they are specific for a family of constitutive equations, or they are equivalent of the ones presented here.

3.7 Time Scale

The TEVP transient flow has four governing equations, and three of them have a time derivative, meaning that each equation can have a different timescale. Barnes (1997) affirms that thixotropic timescales are usually longer than viscoelastic timescales, and the same was observed by Oishi, Thompson & Martins (2016), for example. This is an issue, as the smaller timescales acts as a bottleneck to the time step size, and the bigger timescales demand a long simulated time. This combination increases the numerical cost and increase the instability of the routine, as a time step can be too big to accurately simulate a behaviour at the same time it could be too small to identify the effects of other behaviour in a reasonable amount of computational time.

The use of a segregated method, like PISO or PIMPLE, increases the numeric costs even more. As can be seen in Section 3.6, the coupling of the four equations is not simple, and several terms are treated as explicit source terms, which demands more iterations to be solved. Even though PIMPLE usually allows bigger time steps when compared to PISO, it does not ensure a faster simulation, as the explicit terms still need to be solved iteratively. But the PIMPLE algorithm does ensure that there is a convergence criteria at each time step, which is an important feature: when the routine is not able to achieve the convergence at each time step, these numerical errors pile up during the simulation, changing the transient response, specially on long simulations.

Thus, correctly determining the time step size is of paramount importance. There is no perfect way to determining it, and time step in the present work is defined by the smaller time step between three main criteria:

- A maximum Courant number(COURANT; FRIEDRICHS; LEWY, 1967). This criteria is implemented by default at OpenFOAM® and it is related to the distance that any information travels within the mesh during a time step. At the TEVP re-start problem, the velocity is usually relatively low, so this criteria is the least adopted between the three;

- A maximum relative change within the time step for the fluidity field and the stress field: This criteria limits how much the fluidity field and the stress field can change within a time step. If the partial time derivative of the fluidity is too high at a certain point of the mesh, the time step size decreases, so the time evolution of the fluidity field can be accurately described. This criteria is particularly important when the internal structure of the TEVP material starts to break, leading to the avalanche effect(COUSSOT et al., 2002);

- A fraction of the total time simulated, limited by a minimum and a maximum values. As already cited, a TEVP simulation can demand a long simulation time, so this criteria tries to update the time step size as the simulation progress, for example: the time step size is always equal to 0.1% of the total simulated time. The time step size can not increase indefinitely, and this criteria would be redundant at the beginning of the simulation, so a maximum and a minimum values are defined. This is the main criteria to define the time step size. It is worthy to mention that, this minimum time step size is only valid to this particular criteria. The first or the second criteria can define a smaller time step size.

Part II

Methodology

4 Modelling

The goal of this section is to discuss the rheological, numerical and physical modelling adopted to solve the re-start flow of a TEVP material.

4.1 Rheological model

The present work adopts the rheological model proposed by de Souza Mendes, Abedi & Thompson (2018), and this section presents the model in detail. In their work, de Souza Mendes, Abedi & Thompson (2018) also discuss how to experimentally obtain each property of the model, and applies the proposed experimental methodology to obtain the rheological data for an aqueous suspension of laponite. Their obtained properties were used as a starting point to the values adopted at the present work, and the differences between these two properties sets are also discussed at this section.

4.1.1 The stress equation

The adopted stress equation is an adaptation of the Oldroyd-B stress equation (Equation 3.3),as follows:

$$\phi_v \mathbf{T} + \left(1 - \frac{\phi_v}{\phi_\infty}\right) J\left(\phi_v^*\right) \overset{\triangledown}{\mathbf{T}} = 2 * \mathbf{D} + 2 * \left(\frac{1}{\phi_\infty} - \frac{\phi_v}{\phi_\infty^2}\right) J\left(\phi_v^*\right) \overset{\triangledown}{\mathbf{D}} \tag{4.1}$$

where ϕ_v is the fluidity, ϕ_∞ is the fluidity of the material when fully unstructured, and J is the compliance. At the original Oldroyd-B stress equation, η_0, λ_1, and λ_2 are constants, while at Equation 4.1 their counterparts are equal to:

$$\begin{aligned} \eta_0 &= \frac{1}{\phi_v} \\ \lambda_1 &= \frac{1}{\phi_v}\left(1 - \frac{\phi_v}{\phi_\infty}\right) J\left(\phi_v^*\right) \\ \lambda_2 &= \left(\frac{1}{\phi_\infty} - \frac{\phi_v}{\phi_\infty^2}\right) J\left(\phi_v^*\right) \end{aligned} \tag{4.2}$$

The stress split manipulation presented at Section 3.4 can also be applied to Equation 4.1:

$$\boldsymbol{\tau}_p + \frac{1}{\phi_v}\left(1 - \frac{\phi_v}{\phi_\infty}\right) J\left(\phi_v^*\right) \overset{\triangledown}{\boldsymbol{\tau}}_p = \frac{2}{\phi_s}\mathbf{D} \tag{4.3}$$

where ϕ_s is the structural fluidity, and it is equal to:

$$\phi_s = \frac{1}{\eta_p} = \phi_v \left(1 - \frac{\phi_v}{\phi_\infty}\right)^{-1} \tag{4.4}$$

4.1.2 Analogous mechanical system

As an adaptation of the Oldroyd-B stress equation, the mechanical system analogous to Equation 4.1 is represented at Figure 12, also know as Jeffreys model.

Figure 12 – Mechanical system analogous to Equation 4.1.

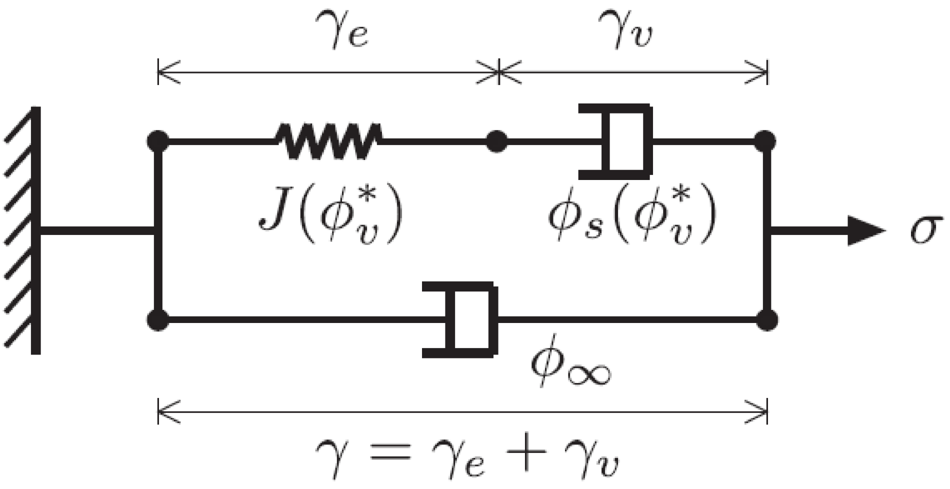

Source: de Souza Mendes, Abedi & Thompson (2018)

The following relationships can be inferred from Figure 12:

$$\begin{aligned}\boldsymbol{\gamma} &= \boldsymbol{\gamma}_e + \boldsymbol{\gamma}_v \\ \dot{\boldsymbol{\gamma}} &= \dot{\boldsymbol{\gamma}}_e + \dot{\boldsymbol{\gamma}}_v \\ \boldsymbol{\tau} &= \frac{\dot{\gamma}}{\phi_\infty} + \frac{\dot{\gamma}_v}{\phi_s} + \frac{\gamma_e}{J(\phi_v^*)}\end{aligned} \tag{4.5}$$

where $\boldsymbol{\gamma}$ is the strain tensor, and $\dot{\boldsymbol{\gamma}}$ is the strain rate tensor. The subscript e indicates the elastic contribution and the subscript v indicates the viscous contribution.

4.1.3 Fluidity ϕ_v

The adopted rheological model replaces the concept of viscosity with the concept of fluidity, that is the reciprocal of the viscosity, as can be seen in Equation 4.2 and Equation 4.4. The main advantage of this transformation is that the fluidity has always finite values, while true yield stress models show infinite viscosity under the yield stress.

Thus, it is possible to define a maximum and a minimum values for the fluidity of a specific material, which allows to define the normalized fluidity ϕ_v^*:

$$\phi_v^* = \frac{\phi_v - \phi_0}{\phi_\infty - \phi_0} \tag{4.6}$$

where ϕ_0 is the fluidity of the fully structured material, or the minimum fluidity, and ϕ_∞ is the fluidity of the fully unstructured material, or the maximum fluidity. Thus, the maximum normalized fluidity is equal to one, when the material is completely unstructured and the fluidity is maximum, and the minimum normalized fluidity is equal to zero, when the material is completely structured and the fluidity is minimum. For true yield stress models, ϕ_0 is equal to zero, and the normalized fluidity is equal to the ratio between the local fluidity and the fluidity of the fully structured material.

The present model assumes that there is an one-to-one correspondence between the current fluidity and the current microscopic state, thus there is no need to define a structure parameter and the normalized fluidity (ϕ_v^*) can be used directly to describe the structuring level. That is the reason, for example, it is possible to define the compliance J as a function of only ϕ_v^*, as can be seen in Equation 4.1 to Equation 4.4.

4.1.4 Fluidity evolution equation

The second differential equation that composes the adopted rheological model is the evolution equation for the fluidity. As a thixotropic material, the changes at the microscopic state do not happen instantly, so it is necessary to stablish a model that defines how the microscopic state changes over time. It is expected that, after being exposed to a certain stress for a sufficient time, the microscopic state would converge to a specific value, allowing to define an equilibrium fluidity (ϕ_{eq}^*) function. This way, the fluidity evolution equation must take into account not only the current state, but also the state it would converge after a sufficient long time. Equation 4.7 show the adopted fluidity evolution equation.

$$\frac{\partial \phi_v^*}{\partial t} + \mathbf{v} \cdot \nabla \phi_v^* = f\left(\phi_v^*, \phi_{eq}^*\right) \tag{4.7}$$

where $f\left(\phi_v^*, \phi_{eq}^*\right)$ is a characteristic of the material. It is important to highlight that the breakup and the build-up mechanisms are usually different (MEWIS; WAGNER, 2009), so that $f\left(\phi_v^*, \phi_{eq}^*\right)$ may be divided into two functions: the breakup part, where $\phi_v^* < \phi_{eq}^*$, and the build up part, where $\phi_v^* > \phi_{eq}^*$. Also, equilibrium fluidity (ϕ_{eq}^*) is a function of current stress ($\boldsymbol{\tau}$) , so it is possible to write $f\left(\phi_v^*, \phi_{eq}^*\right)$ as $f\left(\phi_v^*, \boldsymbol{\tau}\right)$

4.1.5 Equilibrium fluidity flow curve equation

As already mentioned, the function that correlates the current stress with the equilibrium fluidity is a characteristic of the material, so it can change its form for different materials and ranges. To describe the equilibrium fluidity function of an aqueous suspension of laponite, de Souza Mendes, Abedi & Thompson (2018) adopts the following expression:

$$\phi_{eq}(\tau) = \phi_0 + \frac{(\phi_\infty - \phi_0)\left[\frac{1}{\tau}\left(\frac{|\tau-\tau_0|}{K}\right)^{\frac{1}{n}}\right]}{(\phi_\infty - \phi_0) + \left[\frac{1}{\tau}\left(\frac{|\tau-\tau_0|}{K}\right)^{\frac{1}{n}}\right]} H_v(\tau - \tau_0) \tag{4.8}$$

where K is the consistency index, n is the power-law index, τ_0 is the yield stress, and the H_v function is the Heaviside function. τ is the stress intensity, given by:

$$\tau = \sqrt{\frac{\boldsymbol{\tau}^2}{2}} \tag{4.9}$$

The normalized equilibrium equation is equal to:

$$\phi^*_{eq}(\tau) = \frac{\left[\frac{1}{\tau}\left(\frac{|\tau-\tau_0|}{K}\right)^{\frac{1}{n}}\right]}{(\phi_\infty - \phi_0) + \left[\frac{1}{\tau}\left(\frac{|\tau-\tau_0|}{K}\right)^{\frac{1}{n}}\right]} H_v(\tau - \tau_0) \tag{4.10}$$

Figure 13 – Equilibrium fluidity curve obtained with Equation 4.8, adopting $\dot{\gamma}^*_1 = 1$, n=0.3 and $\phi^*_0 = 10^{-3}$

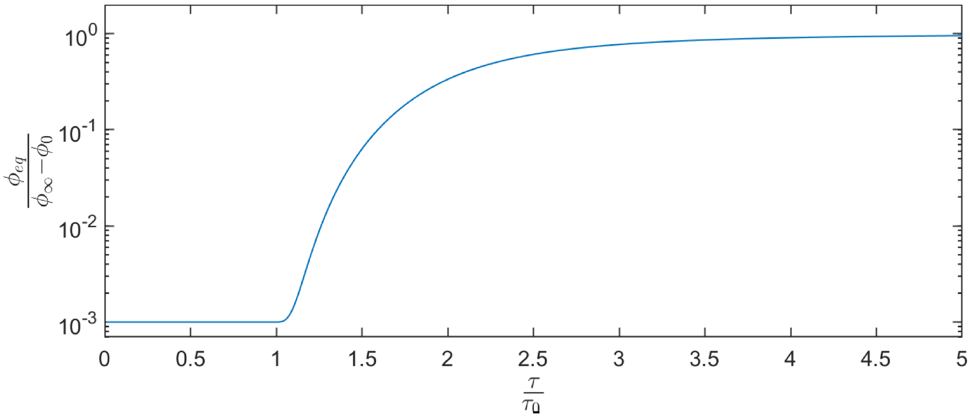

Equation 4.8 is based on the Herschel–Bulkley equation, and can represent both true yield materials and apparent yield stress materials. Figure 13 shows an example of equilibrium fluidity curve obtained with Equation 4.8. If $\tau < \tau_0$, the equilibrium fluidity is

equal to the minimum fluidity ϕ_0, and when the value of τ surpasses τ_0, the value of ϕ_{eq} changes drastically, increasing some orders of magnitude. As the value of τ increases, the value of ϕ_{eq} tends asymptotically to the maximum fluidity of the material, ϕ_∞. If $\phi_0 = 0$, the material is considered as a true yield stress material, while materials with $\phi_0 > 0$ are considered as apparent yield stress materials.

4.1.6 Fully structured material fluidity

In its work, de Souza Mendes, Abedi & Thompson (2018) declared that no Newtonian plateau at the low-stress range was observed during the experiments, leading to the conclusion that $\phi_0 = 0$ for the aqueous suspension of laponite studied. This results means that this suspension is a true yield stress material. Even though Equation 4.8 can model this behaviour, it poses many numerical problems. For example: the Equation 4.6 can be re-written as:

$$\phi_v = \phi_v^* \left(\phi_\infty - \phi_0\right) + \phi_0 \tag{4.11}$$

where ϕ_v^* can range from zero to one. When $\phi_0 = 0$, ϕ_v can be equal to zero, which is a problem, as several expressions are divided by ϕ_v, such as Equation 4.3. Siqueira, Pasquali & de Souza Mendes (2020) and Cunha, de Souza Mendes & Siqueira (2020), whose works are also based at de Souza Mendes, Abedi & Thompson (2018) paper, adopt $\phi_0^* = 10^{-8}$, where:

$$\phi_0^* = \frac{\phi_0}{\phi_\infty - \phi_0} \tag{4.12}$$

From a numerical point of view, a $\phi_0 << \phi_\infty$ can approximate the solution of a $\phi_0 = 0$, although a $\phi_0 = 0$ means that the material is a true yield stress material, while $0 < \phi_0 << \phi_\infty$ means a apparent yield stress material. Furthermore, from a numerical point of view, the bigger the difference between ϕ_0 and ϕ_∞, the more difficult is to solve Equation 3.1 and Equation 4.1. ϕ_0 and ϕ_∞ defines the minimum and the maximum values of ϕ_v, and Section 3.6 shows that the ϕ_v can appear as an explicit term at some formulations. Thus, the bigger the difference between ϕ_0 and ϕ_∞, the more relevant this term tends to be, and because of its explicit nature it is specially difficult to solve. At the present work, $\phi_0^* = 10^{-3}$ was adopted, as a compromise between the numerical efficiency and the observed behaviour of the aqueous suspension of laponite.

4.1.7 Avalanche behaviour

The avalanche behaviour in viscoplastic fluids is characterized by the self-feeding process where the microscopic structure of the material breaks, increasing the fluidity of the material, which increases the flow rate, what, in turn, favours more breakage of the microscopic structure (COUSSOT et al., 2002). This self-feeding process can lead to a sudden microstructure collapse, where the thixotropic viscoplastic material starts to flow at a high rate. To model this behaviour of the aqueous laponite suspension, de Souza Mendes, Abedi & Thompson (2018) proposes the following function when $\phi_{eq}^* > \phi_v^*$:

$$f\left(\phi_v^*, \phi_{eq}^*\right) = \frac{s}{t_a^*} \frac{1}{\phi_{eq}^* + \phi_0^*} \left(\phi_{eq}^* - \phi_v^*\right)^{\frac{s+1}{s}} \left(\phi_v^* + \phi_0^*\right)^{\frac{s-1}{s}} \tag{4.13}$$

where s is a positive parameter, and t_a^* is the dimensionless avalanche time and their expressions are:

$$s = \frac{8}{exp\left(\phi_{eq}^*/0.09\right) - 1} + 1.2 \tag{4.14}$$

$$t_a^* = \alpha_t \frac{\left(1 - \phi_{eq}^*\right)^{1.1}}{\left(\phi_{eq}^*\right)^{0.4}} \tag{4.15}$$

where α_t is a time constant. Both s and t_a^* tends to the infinity when $\phi_{eq}^* \to 0$. The ratio $\frac{s}{t_a^*}$, that is present at Equation 4.13, also tends to the infinity when $\phi_{eq}^* \to 0$, which means that $f\left(\phi_v^*, \phi_{eq}^*\right)$ not only increases at the vicinity of $\phi_{eq}^* = 0$ but tends to the infinity, making the microstructural change instantaneous, independent of the current fluidity ϕ_v^*. Even though Equation 4.13 only rules the domain where $\phi_{eq}^* > \phi_v^*$ and the minimum value of ϕ_v^* is zero, the condition $\phi_{eq}^* \to 0$ is still an issue, so to avoid it the present work adopted a constant value for $s = 2$. The same strategy was adopted by Siqueira, Pasquali & de Souza Mendes (2020) and Cunha, de Souza Mendes & Siqueira (2020).

4.1.8 Construction time

On the other hand, when $\phi_{eq}^* > \phi_v^*$ the internal structure of the material tends to recover, decreasing the fluidity of the material. This phenomenon normally happens on a different time scale when compared to the avalanche behaviour: if the avalanche behaviour can lead to an abrupt change at the microstructure of the material, the change at the fluidity provoked by the construction time is usually more gradual, and often involves large time scales. The following expression has proposed (DE SOUZA MENDES; ABEDI; THOMPSON, 2018) to model the aqueous laponite suspension $f\left(\phi_v^*, \phi_{eq}^*\right)$ when $\phi_{eq}^* < \phi_v^*$:

$$f\left(\phi_v^*, \phi_{eq}^*\right) = \frac{\phi_v^* - \phi_{eq}^*}{T_c^*} \tag{4.16}$$

where T_c^* is the dimensionless characteristic time of the microstructure construction process. At the present work, the following expression was adopt to determine T_c:

$$T_c^* = \begin{cases} \frac{\mathrm{T}_{c,0}^*}{10}, & \text{if } \tau > \tau_0 \\ \mathrm{T}_{c,0}^*, & \text{if } \tau \leq \tau_0 \end{cases} \tag{4.17}$$

Thus, the expression for $f\left(\phi_v^*, \phi_{eq}^*\right)$ can be obtained adding the functions presented at the previous and the present section:

$$f\left(\phi_v^*, \phi_{eq}^*\right) = \begin{cases} \frac{s}{t_a^*}\frac{1}{\phi_{eq}^*+\phi_0^*}\left(\phi_{eq}^* - \phi_v^*\right)^{\frac{s+1}{s}}\left(\phi_v^* + \phi_0^*\right)^{\frac{s-1}{s}}, & \text{if } \phi_v^* \leq \phi_{eq}^* \\ \frac{\phi_v^*-\phi_{eq}^*}{\mathrm{T}_c^*}, & \text{if } \phi_v^* > \phi_{eq}^* \end{cases} \tag{4.18}$$

Figure 14 shows the behaviour described by Equation 4.18, adopting different values of ϕ_{eq}^* and ϕ_v^*. The red lines mean that $f\left(\phi_v^*, \phi_{eq}^*\right)$ is positive ($\phi_{eq}^* \geq \phi_v^*$), and $f\left(\phi_v^*, \phi_{eq}^*\right)$ follows the behaviour described by Equation 4.13, while the blue lines mean that $f\left(\phi_v^*, \phi_{eq}^*\right)$ is negative ($\phi_{eq}^* < \phi_v^*$) and $f\left(\phi_v^*, \phi_{eq}^*\right)$ follows Equation 4.16.

Figure 14 – Values of $f\left(\phi_v^*, \phi_{eq}^*\right)$ for different ϕ_{eq}^* and ϕ_v^*, adopting $\alpha_t = 10^4$, $\mathrm{T}_{c,0}^* = 10^4$ and $s = 2$

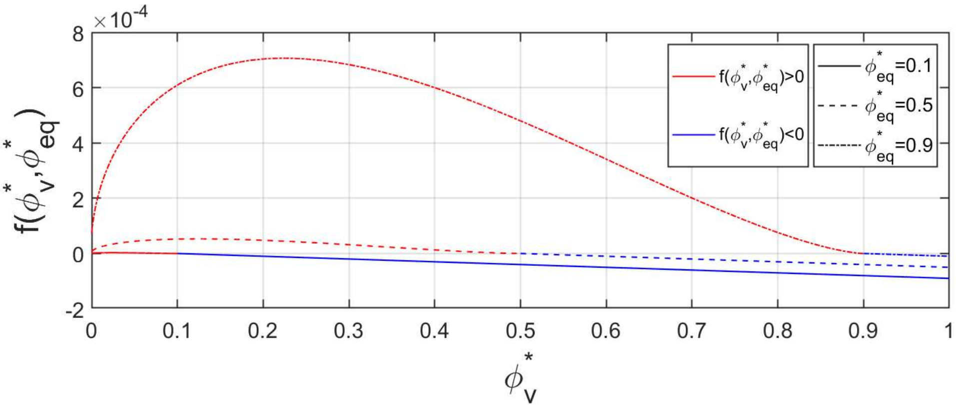

4.1.9 Compliance

At its experiments, de Souza Mendes, Abedi & Thompson (2018) obtained a null first normal stress difference for $\phi_v^* > 0$, meaning that $J(\phi_v^* > 0) = 0$. But they were not able to determine $J(\phi_v^* = 0) = J_0$, even though they clearly identified an elastic behaviour of the suspension. The condition $\phi_v^* = 0$ may not be appropriate to implement at a numerical simulation, so to avoid any issue, the present work implemented the following compliance function $J(\phi_v^*)$

$$J(\phi_v^*) = J_0 H_v(\phi_J^* - \phi_v^*) \tag{4.19}$$

this way, when $\phi_J^* > \phi_v^*$, $J(\phi_v^*) = J_0$, and when $\phi_J^* < \phi_v^*$, $J(\phi_v^*) = 0$. To model the behaviour described by de Souza Mendes, Abedi & Thompson (2018), $\phi_J^* = 10^{-10}$ was adopted at the present work.

4.2 Physical model

The main studied cases of the present work is the re-start flow of TEVP materials at a 4:1 planar contraction and at a 1:4 planar expansion geometries. The flow is considered incompressible and isothermal. Thus, the mass balance equation and the momentum balance equation are two of the governing equations of these cases, as follow:

$$\begin{aligned} &\nabla \cdot \mathbf{u} = 0 \\ &\rho \frac{\partial \mathbf{u}}{\partial t} + \rho \left(\nabla \mathbf{u} \right) \mathbf{u} = -\nabla p + \nabla \cdot \boldsymbol{\tau} \end{aligned} \tag{4.20}$$

In addition to them, there are the constitutive equations of the rheological model (Equation 4.3 and Equation 4.7). The flow is assumed to be initially at rest, fully structured, and without any internal effort. Then, a pressure gradient between the inlet and the outlet is imposed, accelerating the flow and breaking the internal structure of the material. The simulations were performed until the maximum velocity temporal derivative magnitude is lower than 10^{-5}, when the flow is considered at steady-state.

The incompressible flow hypothesis is contested by some authors, such as Lee et al. (2008). But considering a compressible flow would add another layer of complexity over the problem, making the solution more difficult, and likely overshadowing the influence of the rheological parameters.

The isothermal hypothesis not only reduces one equation to be solved (the energy balance equation), but also avoids having to define a model where the rheological properties of the material are also a function of the temperature. Furthermore, the isothermal hypothesis is coherent with the hypothesis of having an infinite planar channel at the inlet and that the flow is at rest for sufficient time to be as close to the fully structured state as possible.

The flow being initially at rest is the main characteristic of a restart flow, and being initially fully structured is coherent when the flows is at rest for a sufficient amount of time. On the other hand, the hypothesis of no internal effort at the beginning of the flow has only chosen to simplify the flow. Phillips et al. (2011), for example, discuss the existence of residual stresses after the thermal contraction. In theory, the solver adopted at the present work can solve flows with residual stresses at the begging of the simulation, but to define an appropriate boundary condition and the initial stress field is not a simple task.

4.2.1 Geometry and boundary conditions

The present work adopts two geometries: a planar expansion 1:4 and a planar contraction 4:1, as shown in Figure 15. In both expansion and contraction geometries, the distance between the two plates of the narrow channel is equal to $2h_n$, and its length is equal to $l_n = 15h_n$, while the wide channel length is equal to $l_w = 20h_n$ and the distance between the two plates of the wide channel is equal to $8h_n$. These geometries are simplifications of flow geometry commonly found at the industries, and several other numerical simulation adopt then, such as Jahromi et al. (2011) and Link et al. (2015). The contraction geometry is often considered as a benchmark experiment for viscoelastic flows(BIRD; WIEST, 1995). Even with their simplicity, these geometries can present complex flow dynamics, highlighting all the modelled behaviours, such as the avalanche effect and the advective transport of the unstructured material.

Figure 15 – Geometries adopted at the present work: (a) 4:1 contraction geometry and (b) 1:4 expansion geometry.

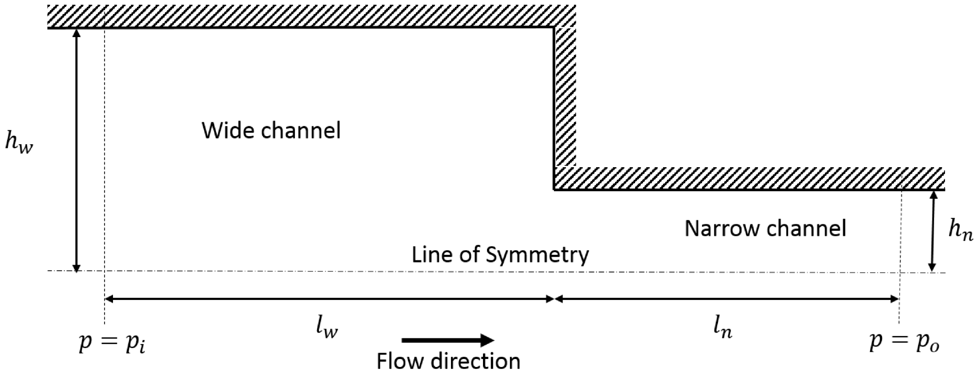

(a) 4:1 contraction geometry

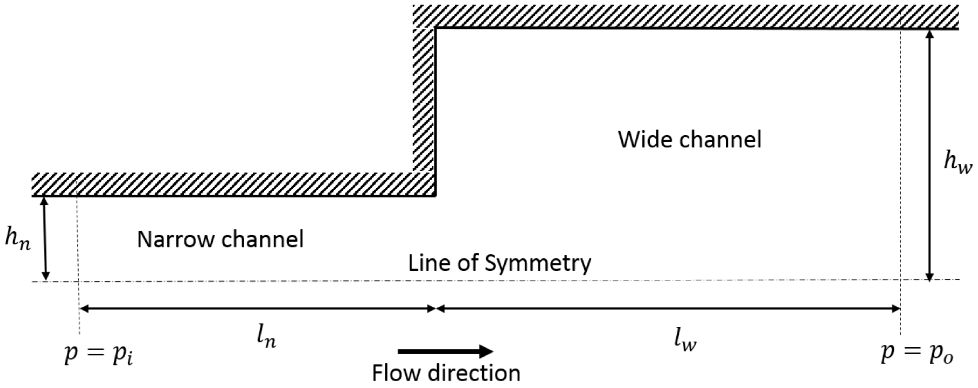

(b) 1:4 expansion geometry

Although some works disagree with the no-slip condition at the walls (Luthi (2013) for example), the present work adopts this boundary condition, due its simplicity and the low velocities involved. The symmetry condition is imposed at the centreline, to reduce the numerical effort to solve these equations. A flat pressure profile is imposed at the inlet and the outlet, and the other flow properties, as the velocity and the fluidity, are calculated assuming a zero gradient condition at the inlet and outlet. This way, the inlet boundary condition simulates an infinite planar channel. Often the outlet channel is shorter than the entrance region provoked by the change of height, thus the zero gradient condition at the outlet region is needed to minimize its influence over the flow.

4.2.2 Dimensionless quantities

A total of eight dimensionless parameters are needed to define the flow. Five of then are related to the rheological model: ϕ_0^*, n, α_t, T_c, $\dot{\gamma}_1^*$. The other three are the dimensionless imposed pressure gradient (Δp^*), the Deborah number (De) and the Reynolds number (Re). The definitions of $\dot{\gamma}_1^*$, Δp^*, De and Re are:

$$\begin{aligned} \dot{\gamma}_1^* &= t_c \left(\frac{\tau_0}{K}\right)^{\frac{1}{n}} \\ \Delta p^* &= \frac{p_i - p_o}{\tau_0} \\ De &= \frac{\lambda_1}{t_c} \\ Re &= \frac{\rho u_c^2}{\tau_c} \end{aligned} \tag{4.21}$$

where t_c, u_c, and τ_c is the characteristic time, velocity and stress, respectively. p_i and p_o are the pressure at the inlet and at the outlet, respectively. The expression of t_c and τ_c are equal to:

$$\begin{aligned} t_c &= \frac{1}{\tau_0\left(\phi_\infty - \phi_0\right)} \\ \tau_c &= \frac{p_i - p_o}{L_w \frac{h_n}{h_w} + L_n} \end{aligned} \tag{4.22}$$

As the flow starts at rest and accelerates as the simulation advances, it is an issue to define a u_c and τ_c that represents the flow. The Equation 4.22 is an estimation of the maximum stress when the simulations starts, assuming no inertial effects and neglecting the effects of the abrupt expansion/contraction over the flow. At the simulations, the maximum stress are located at abrupt expansion/contraction, which makes its estimation really complicated. However, when $t \rightarrow 0$, the pressure gradient over the narrow channel far enough of the expansion/contraction is relatively constant around $0.96\tau_c$. Thus, Equation 4.22 was adopted as a good enough estimation. The value of the characteristic velocity is obtained solving the following expression(THOMPSON; SOARES, 2016):

$$\tau_c = \tau_0 + K\left(\frac{u_c}{l_c}\right)^n + \frac{u_c}{\phi_0 l_c} \tag{4.23}$$

where l_c is the characteristic length, and it is equal to the narrow channel height. Once again, u_c is just an estimation, adopted mainly to define the Reynolds number. The same methodology was adopted by Oishi, Thompson & Martins (2016) to determine u_c. Even though the present work does not aim to investigate the inertia effects, they are taken into account, so the Re must be defined to fully describe the flow.

Finally, the following dimensionless variables were adopted at the present work:

$$t^* = \frac{t}{t_c} \qquad \mathbf{u}^* = \frac{\mathbf{u}t_c}{l_c} \qquad \boldsymbol{\tau}^* = \frac{\boldsymbol{\tau}}{\tau_0} \tag{4.24}$$

4.2.3 Deborah number x Weissenberg number

As discussed by Poole (2012), the Deborah number and the Weissenberg number are widely used to define the viscoelastic effects, even though they quantify different effects. As can be seen in Equation 4.21, De represents a ratio between two times, the time of relaxation over the characteristic time. On the other hand, the Weissenberg number (Wi) represents the ratio between elastic forces and viscous forces. The Wi expression is often found as:

$$Wi = \frac{\lambda_1 u_c}{l_c} \tag{4.25}$$

However, as already discussed, the definition of a characteristic velocity at a complex re-start flow can be quite challenging, thus the present work adopted the Deborah number to represent the viscoelastic effects.

4.2.4 Rheological parameters values

Table 1 and Table 2 present the values of the rheological parameters found at the works of de Souza Mendes, Abedi & Thompson (2018), Cunha, de Souza Mendes & Siqueira (2020) and the present work. At their work, de Souza Mendes, Abedi & Thompson (2018) was not able to measure the compliance of the material at the fully structured state. As the present work aims to perform numerical simulations, there is no issue defining an arbitrary value for this property.

Table 1 – Comparison between the values of ϕ_0^*, n, $\dot{\gamma}_1^*$, and α_t found in the literature and adopted at the present work.

	ϕ_0^*	n	$\dot{\gamma}_1^*$	α_t
de Souza Mendes, Abedi & Thompson (2018)	0	0.32	0.8	22768.32
Cunha, de Souza Mendes & Siqueira (2020)	10^{-8}	0.3	1	10^4
Present work	10^{-3}	0.3	1	10 to 10^4

Another difference the present work tends to adopt lower values for T_c^* and α_t. The main reason for that is to accelerate the flow, as a higher α_t decrease the rate that the

Table 2 – Comparison between the values of T_c^*, and De found in the literature and adopted at the present work.

	T_c^* if $\tau > \tau_0$	T_c^* if $\tau \leq \tau_0$	De
de Souza Mendes, Abedi & Thompson (2018)	11153.4	254989.8	-
Cunha, de Souza Mendes & Siqueira (2020)	10^4	10^5	0
Present work	0.1 to 10^4	1 to 10^5	0 to 10

microstructure of the flow is broken, delaying its steady-state, for example, and increasing the numerical cost to obtain it. But the biggest difference is the value of ϕ_0^*. While de Souza Mendes, Abedi & Thompson (2018) characterized the aqueous suspension of laponite as an true yield stress material ($\phi_0^* = 0$), the present work adopted $\phi_0^* = 10^{-3}$. The main reason for that difference is numerical: the lower the ϕ_0^*, the more difficult is to solve the stress equation, as Section 5.1.2.1 explains in detail. Adopting a $\phi_0^* = 0$ or even $\phi_0^* = 10^{-8}$ would increase the numerical cost of these solutions, increasing the time needed to obtain then in some orders of magnitude.

The value of ϕ_0^* represents the difference between the maximum and minimum fluidity of the material. When the flow has a relatively high stress, the fluidity of the material inside the flow can vary some orders of magnitude, and changing the value of ϕ_0^* from 10^{-8} to 10^{-3}, for example, has little to no influence over the flow, as the difference between the maximum and the minimum fluidity inside the flow is already high enough. The issue is when the flow has relatively low stress, decreasing the maximum fluidity of the flow and consequently approaching the maximum and minimum values of fluidity of the flow. For this reason, all the numerical simulations of the present work adopts the condition of $\tau_c \geq 2\tau_0$, to ensure that the maximum fluidity of the flow is significantly higher than the minimum fluidity of the material.

4.3 Numerical model

The simulations presented in this work were performed using OpenFOAM®, with a customized solver implemented by the author. This customized solver can solve Equation 4.20, Equation 4.3 and Equation 4.18 by adopting the PIMPLE algorithm (Figure 11). This algorithm was chosen because of its capacity to evaluate the convergence of the solution, increasing its accuracy. The explicit diffusion technique was adopted as a stabilization method, without any special strategy to couple the governing equations, like the correction scheme adopted by Oishi, Thompson & Martins (2016), for example. This way, the explicit character of the governing equations is enhanced, justifying the adoption of the PIMPLE algorithm, as it can perform several iterations to solve these explicit terms. The price for this better accuracy is that the numerical cost is increased. It is important to highlight that these two strategies, the PIMPLE algorithm and the correction scheme adopted by

Oishi, Thompson & Martins (2016), are not mutually exclusive and can be implemented together.

Another important aspect is that at a transient simulation, the numerical errors can accumulate at each time step, and even relatively small errors can lead to important deviations after several time steps. This can change the transient response of the system, even though the steady-state response usually is achieved eventually, if the system does not diverge. This way, the steady-state response does not guarantee the accuracy of the transient response, and the discretization error estimation(ASME, 2008), for example, must take these transient elements into account. The PIMPLE algorithm capacity to evaluate the accuracy of the solution at the end of each iteration is vital here too: this way, it is possible to refine an unpolished response, while avoiding wasting time and numerical resources with a good enough solution.

All the other stabilization methods showed to be unstable or did not show any improvement when compared to the explicit diffusion technique. This instability is probably due to the explicit character of the system of equations, and probably a more implicit solution can allow a faster stabilization method. But, as already mentioned in Section 4.1.6, the viscoplastic behaviour itself increases the explicit character of the system of equations, making it difficult to obtain a “more implicit solution”.

As explained in Section 4.1.9, only a certain region of the simulated domain showed viscoelastic properties. Furthermore, there are other numerical bottlenecks, like the already mentioned explicit character of the governing equations. Thus, the implementation of a log conformation method, for example, showed no numerical advantage and the present work does not adopt it.

Even though the RheoTool toolbox has several routines built specifically to solve complex flows, they did not show any real improvement when compared to the routines implemented using only the default routines of OpenFOAM®. This way, all simulations shown in the present work were performed without the need to install the RheoTool toolbox.

5 Code validation and Discretization error estimation

The main objective of this chapter is to present solid evidence of the accuracy of the proposed methodology. To validate the code, the results of the proposed routine were compared with the results of similar works found in the literature. As already mentioned in Section 2.4, there are only a few numerical works that consider a TEVP behaviour, and their application or adopted models can vary significantly, making comparisons between them and the present work more difficult and even impossible. Thus, the code validation is divided into two parts: a viscoelastic part and a thixotropic viscoplastic part. Then, the discretization error estimation employed to evaluate the adopted mesh is presented, with the associated extrapolated error and grid convergence index (GCI).

5.1 Code validation

To validate the viscoelastic behaviour, two different approaches were adopted: an analytical solution of an Oldroyd-B model flow inside a planar channel and a numerical solution of the planar contraction Oldroyd-B model flow. Then, the methodology proposed by Siqueira, Pasquali & de Souza Mendes (2020) was employed to validate the thixotropic and viscoplastic behaviours of the present work. This methodology consists of a semi-analytical solution of the flow inside an axisymmetric channel, adopting a stress profile and using it to numerically solve the transient flow.

5.1.1 Viscoelastic behaviour

The stress equation (Equation 4.1) of the rheological model adopted at the present work is an adaptation of the Oldroyd-B model (Equation 3.3), so it is relatively simple to make them equivalent: assuming thixotropic characteristic times (α_t and T_t) long enough, the time derivative of the fluidity (Equation 4.18) tends to zero, allowing the fluidity and the coefficients of the stress equation (Equation 4.2) to be considered constant.

5.1.1.1 Planar channel

This section numerically reproduces the Poiseuille viscoelastic flow analytical solution proposed by Waters & King (1970). The adopted geometry is a planar channel and the fluid is initially at rest, when a constant pressure gradient is imposed over the domain. To simplify the calculations, the fluid is assumed as fully structured ($\phi_v = \phi_0$), and

α_t and $T^*_{c,0}$ are big enough so that $f\left(\phi^*_v, \phi^*_{eq}\right) \to 0$. Thus, the Oldroyd-B model coefficients η_p, η_s and λ_1 (Equation 3.5) are equal to:

$$\begin{aligned} \eta_p &= \frac{1}{\phi_0} - \frac{1}{\phi_\infty} \\ \eta_s &= \frac{1}{\phi_\infty} \\ \lambda_1 &= \left(\frac{1}{\phi_0} - \frac{1}{\phi_\infty}\right) J\left(\phi_0\right) = \eta_p J_0 \end{aligned} \tag{5.1}$$

The inertia effects are neglected and the two dimensionless quantities needed to define the flow are the Weissenberg number (Wi) and the viscosity ratio (β). Due to the flow characteristics, a new dimensionless time (t^*_{ve}) and dimensionless velocity ($U^*_{x,ve}$) are adopted in this section. The definitions of β, t^*_{ve} and $U^*_{x,ve}$ are:

$$\begin{aligned} \beta &= \frac{\eta_s}{\eta_s + \eta_p} \\ t^*_{ve} &= \frac{t l_c}{u_{c,ve}} \\ u^*_{x,ve} &= \frac{u_x}{u_{c,ve}} \\ u_{c,ve} &= \frac{\partial p}{\partial x} \frac{1}{2\eta_0} \end{aligned} \tag{5.2}$$

where t is the time, $u_{c,ve}$ and l_c are the characteristic velocity and characteristic length, respectively. For this configuration, the channel height is taken as the characteristic length and the characteristic velocity is equal to the symmetry velocity of the fully developed profile. The adopted mesh consists of a 1D mesh with 200 volumes. Figure 16 compares the temporal evolution of the dimensionless velocity for viscoelastic flows over the symmetry line for the two approaches: the analytical solution and the numerical solution, obtained with the routine developed by the author of the present work. The dotted line with x markers is the analytical solution proposed by Waters & King (1970) while the solid line is the result obtained with the proposed routine. Three different values of β and of Wi were adopted. As can be seen, the adopted routine can reproduce the analytical solution with accuracy.

5.1.2 Thixotropic viscoplastic behaviour

To evaluate the capacity of the adopted routine to replicate the thixotropic viscoplastic behaviour, the planar channel flow was simulated by adopting the rheological model presented in Section 4.1, with $J_0 = 0$. Assuming that the planar channel is long enough and the inertia and the viscoelastic effects are negligible, the stress equation (Equation 4.3) and the momentum balance equation (Equation 4.20) can be written as:

Figure 16 – Temporal evolution of $u^*_{x,ve}$ at the symmetry line. The dotted line with x markers is the analytical solution proposed by Waters & King (1970) while the solid line is the result obtained with the proposed routine. Results obtained adopting (a) $Wi = 1$ and $\beta = 0.1, 0.01$, and 0.001; and (b) $\beta = 0.1$ and $Wi = 0.1, 1$, and 10.

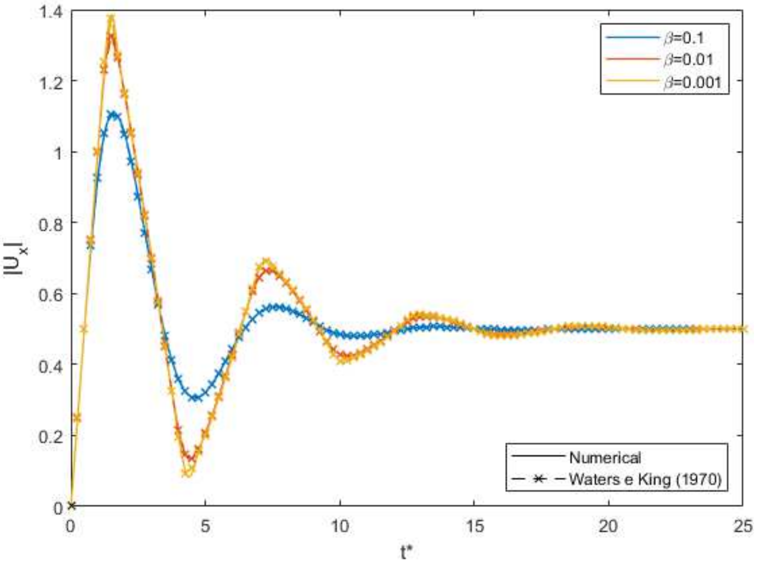

(a) $Wi = 1$ and $\beta = 0.1, 0.01$, and 0.001

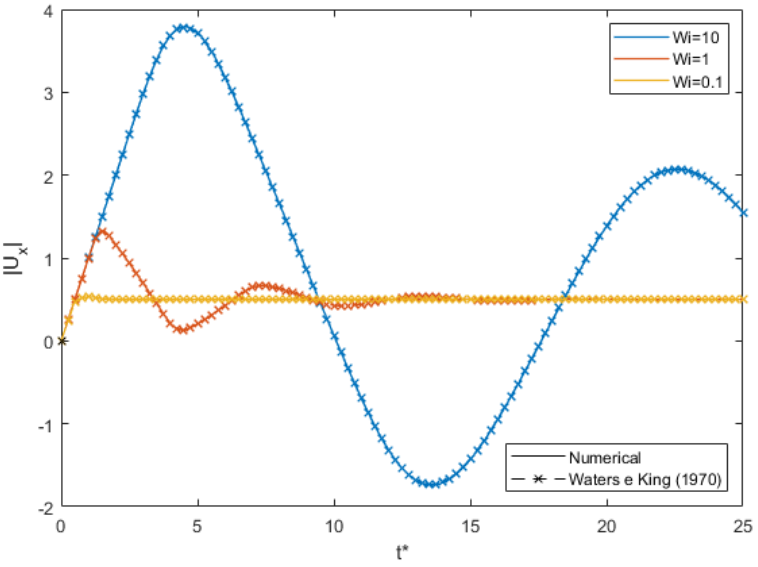

(b) $\beta = 0.1$ and $Wi = 0.1, 1$, and 10

$$\begin{aligned} \phi_v \boldsymbol{\tau} &= 2\mathbf{D} \\ \nabla \cdot \ \boldsymbol{\tau} &= \nabla p \\ \mathbf{D} &= \frac{1}{2}\frac{\partial u_x}{\partial y} \end{aligned} \tag{5.3}$$

The flow is initially at rest and fully structured, and then the Poiseuille flow condition is adopted, with an imposed pressure gradient. A 1D mesh is adopted to solve

Equation 4.18 and Equation 5.3, with the no-slip condition at the channel walls. Six dimensionless quantities are needed to define the flow: ϕ_0^*, n, α_t, $\mathrm{T}_{c,0}^*$, $\dot{\gamma}_1^*$ and the plastic number (Pl), which is defined as follows:

$$Pl = \left| \left(\frac{\partial p}{\partial x} \right)^{-1} \right| \tau_0 \tag{5.4}$$

Solving Equation 5.3, it is possible to obtain that the stress tensor is composed only of two shear components (τ_{xy} and τ_{yx}) and its magnitude is defined as:

$$\tau_{xy} = \frac{\partial p}{\partial x} y \tag{5.5}$$

Thus, the evolution of ϕ_v^* and u_x can be obtained by integrating Equation 4.18 over time. A similar methodology was applied by Cunha, de Souza Mendes & Siqueira (2020), but assuming the axisymmetric channel. Figure 17 and Figure 18 compare the results obtained with the methodology explained in the present section and results obtained with the routine developed by the author of the present thesis, the first figure in terms of the normalized fluidity (ϕ_v^*) and the second one in terms of the dimensionless flow rate (Q^*). The routine developed by the authors is fully numerical, thus it solves Equation 4.3, Equation 4.18 and Equation 4.20 by adopting a iteration process. Figure 17 and Figure 18 were obtained assuming $\phi_0^* = 10^{-3}$, $n = 0.3$, $\alpha_t = 10^4$, $\mathrm{T}_{c,0} = 10^4$, $\dot{\gamma}_1^* = 1$ and three different values of Pl: 0.01, 0.2 and 0.5. The results of these two different methodologies present a good agreement, showing that the routine developed in the present work can replicate the semi-analytical results of the methodology explained in the present section.

5.1.2.1 The numerical effects of ϕ_0^*

As mentioned in Section 4.1.6, the bigger the difference between ϕ_0 and ϕ_∞, the more difficult is to solve Equation 3.1 and Equation 4.1. ϕ_0^* represents how big is this difference, thus, the lower the ϕ_0^*, the more numerically difficult is to solve the system of equations. This can be observed in Equation 5.3. For example: assuming $\phi_0^* = 10^{-8}$, $l_c = 1$ and $Pl = 0.2$, the maximum value of τ_{xy} is equal to $5\tau_0$, while the values of ϕ_v can change from $\phi_v = 10^{-8}$ (at $y < 0.2 l_c$) to $\phi_v \approx 0.95\phi_\infty$ (at $y = l_c$). It means that ϕ_v can change 8 orders of magnitude while τ_{xy} only changed from τ_0 to $5\tau_0$. It means that $\mathbf{D}$ must also change almost 8 orders of magnitude to solve Equation 5.3. The numerical partial derivative $\frac{\partial U_x}{\partial y}$ can be written as:

$$\frac{\partial U_x}{\partial y} = \frac{U_x^{j+1} - U_x^{j}}{\Delta y} \tag{5.6}$$

Figure 17 – Temporal evolution of the normalized fluidity (ϕ_v^*) for: (a) $Pl = 0.01$, (b) $Pl = 0.2$ and (c) $Pl = 0.5$, comparing the results of a fully numerical method and a semi analytical method.

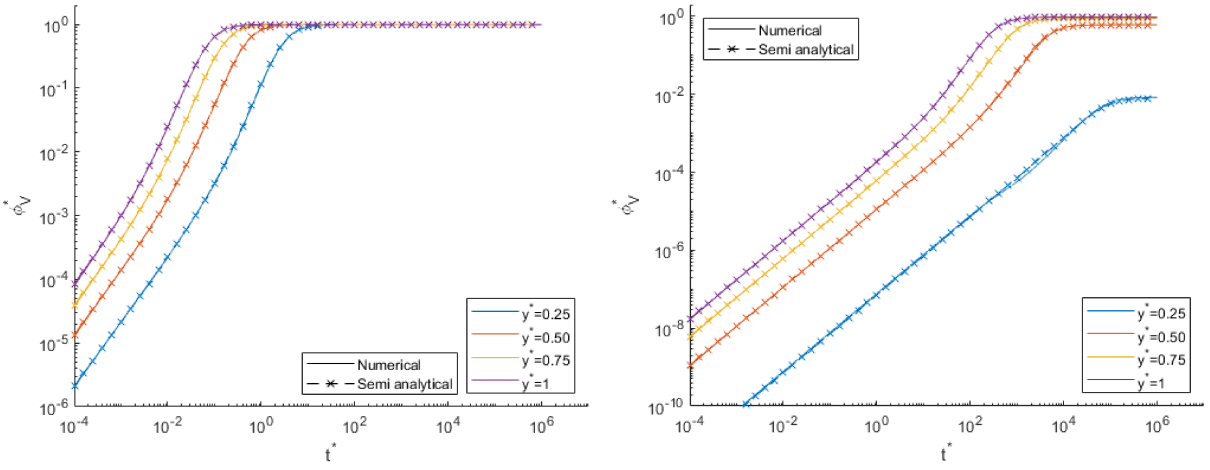

(a) $Pl = 0.01$ (b) $Pl = 0.2$

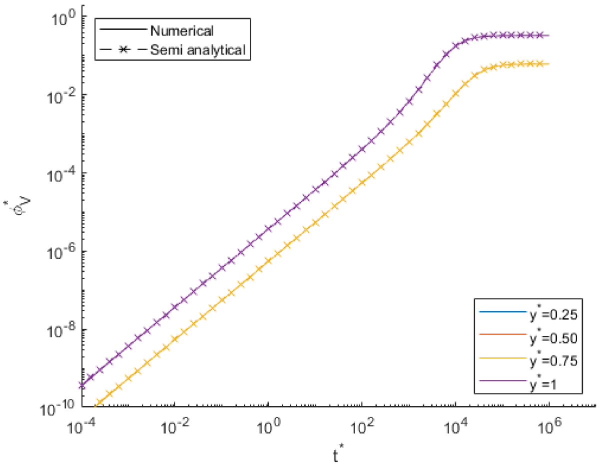

(c) $Pl = 0.5$

where U_x^{j+1} and U_x^j are the values of the horizontal velocity of two neighbouring volumes, and Δy is the distance between their centroids. Thus, when considering a $\Delta y = 10^{-2}$ and $\phi_0^* = 10^{-8}$, the values of U_x^{j+1} and U_x^j must be solved with 6 orders of magnitude of precision. Achieving this precision is a challenge for steady-state simulations, and can render a transient numerical simulation almost impossible, demanding years of calculations even for simple simulations, like a 200 volumes mesh of a planar channel. This is the main reason for the choice of the value of ϕ_0^* in the present work.

5.2 Discretization error estimation

The mesh quality tests were performed as described by ASME (2008), adopting the meshes described in Table 3. The adopted method is the Grid Convergence Index (GCI)(ROACHE, 1994), which is based on the Richardson extrapolation method(RICHARDSON,

Figure 18 – Temporal evolution of the dimensionless flow rate (Q^*) for Pl: 0.01, 0.2 and 0.5, comparing the results of a fully numerical method and a semi analytical method.

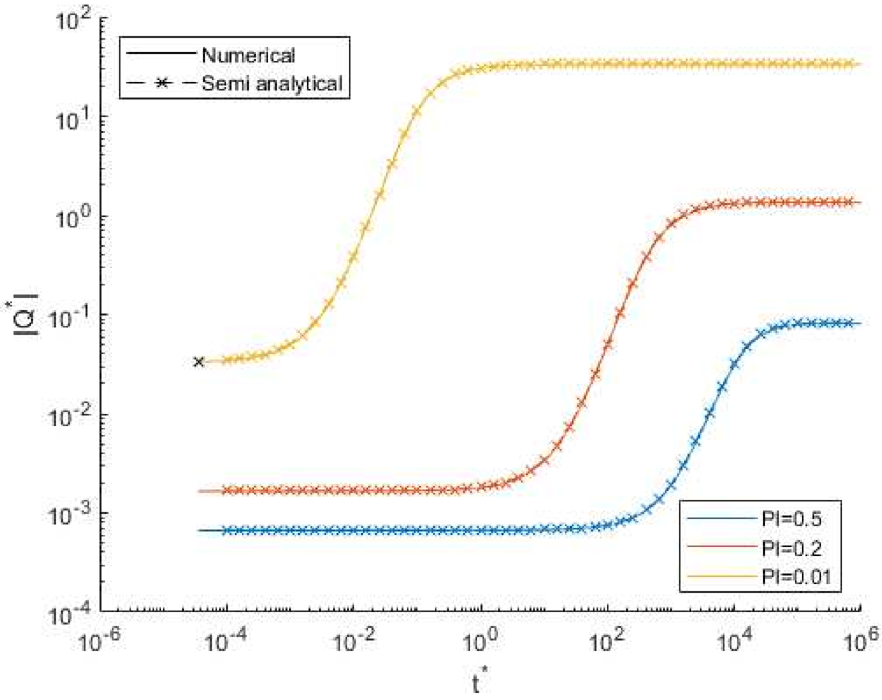

1911). These methods have been widely investigated and reviewed by many authors, like Oberkampf, Trucano & Hirsch (2004), for example. As the name suggests, the GCI method was originally developed to estimate of grid convergence errors, converting error estimates that are obtained from any grid-refinement ratio into an equivalent grid-doubling estimate. The extrapolated value ω_{ext}, the error from the extrapolated value (e_{ext}) and the Grid Convergence Index (CGI) are defined by the following expressions:

Table 3 – Mesh parameters

Mesh	3	2	1
Elements	2000	4808	10800
h^*	0.11616	0.07511	0.05029

$$\omega_{ext} = \frac{r_{21}^{a} * \omega_1 - \omega_2}{r_{21}^{a} - 1} \tag{5.7}$$

$$e_{ext,i} = \left| \frac{\omega_{ext} - \omega_i}{\omega_{ext}} \right| \tag{5.8}$$

$$CGI_{fine}^{21} = \frac{1,25 e_{21}}{r_{21}^{a} - 1} \tag{5.9}$$

where ω is the analysed flow parameter, r is the ratio between the representative element length (h^*) of two different meshes, a is the theoretical order of accuracy. The subscripts indicate the mesh where that parameter was obtained, as defined in Table 3. Thus, e_{21} is the error between the mesh 2 and 1, as follows:

$$e_{21} = \left| \frac{\omega_1 - \omega_2}{\omega_1} \right| \tag{5.10}$$

The numerical uncertainties were estimated using the difference between the extrapolation value and the obtained value in each mesh. The Grid Convergence Index is stated as an error percentage and provides a confidence bound on the estimated error band within which the numerically converged solution will likely lie.

Two tests were performed, one with the contraction geometry and another with the expansion geometry. The tests were performed assuming $\phi_0^* = 10^{-3}$, $n = 0.3$, $\alpha_t = 10$, $\mathrm{T}_{c,0} = 10^4$, $\dot{\gamma}_1^* = 1$, $\Delta p^* = 100$, $De = 1$ and $Re = 1.4$. The flow parameters adopted to evaluate the meshes are the horizontal velocity of the points (-10,0), (0,0), and (5,0) for the contraction test and (-5,0), (0,0) and (10,0) for the expansion test. These points are over the symmetry line, and they lie over the wide channel, the contraction/expansion (depending on the test) and the narrow channel. These three points were evaluated at two different times: $t^* = 1$ and $t^* = 10$. The results of the contraction test can be found in Table 4 and the results of the expansion test can be found in Table 5. The maximum e_{ext} of the adopted mesh was below 3%, for both local and global parameters. The CGI also indicates that the numerical uncertainties are small for this configuration. Figure 19 presents the adopted contraction mesh, showing its refinements near the contraction region.

Table 4 – e_{ext} and CGI of the contraction mesh.

		$t^* = 1$			$t^* = 10$		
	mesh	3	2	1	3	2	1
x*= (0 0 0)	ϕ	0.623	0.617	0.611	1.82	1.82	1.83
	ϕ_{ext}	0.598			1.83		
	e_{ext}(%)	4.21	3.07	2.06	1.31	1.1	0.735
	CGI_{fine}^{21}(%)	2.52			0.926		
x*= (-10 0 0)	ϕ	0.161	0.158	0.156	0.415	0.41	0.409
	ϕ_{ext}	0.151			0.409		
	e_{ext}(%)	6.15	4.35	2.91	2.4	1.07	0.719
	CGI_{fine}^{21}(%)	3.54			0.892		
x*= (5 0 0)	ϕ	0.636	0.623	0.615	2	1.99	2
	ϕ_{ext}	0.599			2		
	e_{ext}(%)	6.08	3.99	2.67	0.199	0.577	0.386
	CGI_{fine}^{21}(%)	3.25			0.485		

Table 5 – e_{ext} and CGI of the expansion mesh.

		t^* = 1			t^* = 10		
	mesh	3	2	1	3	2	1
$\mathbf{x}^*$= (0 0 0)	ϕ	0.605	0.6	0.599	2.01	2	2
	ϕ_{ext}	0.597			2		
	$e_{ext}(\%)$	1.39	0.492	0.269	1.07	0.733	0.402
	$CGI^{21}_{fine}(\%)$	0.336			0.5		
$\mathbf{x}^*$= (10 0 0)	ϕ	0.151	0.149	0.148	0.459	0.452	0.449
	ϕ_{ext}	0.147			0.449		
	$e_{ext}(\%)$	2.8	1.27	0.694	3.02	1.37	0.753
	$CGI^{21}_{fine}(\%)$	0.862			0.934		
$\mathbf{x}^*$= (-5 0 0)	ϕ	0.616	0.606	0.603	2.13	2.09	2.07
	ϕ_{ext}	0.599			2.07		
	$e_{ext}(\%)$	2.91	1.14	0.625	4.12	2.49	1.36
	$CGI^{21}_{fine}(\%)$	0.776			1.68		

Figure 19 – Adopted contraction mesh.

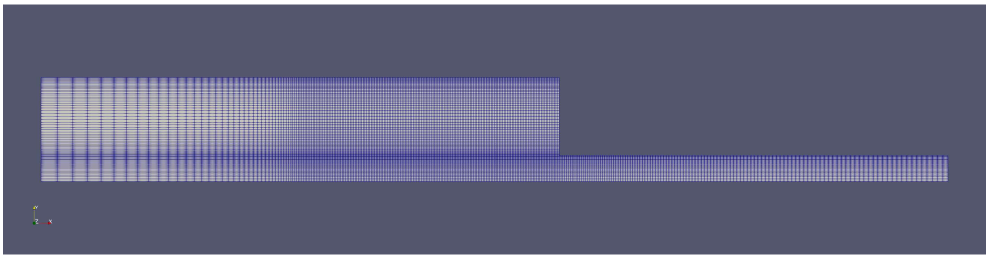

Part III

Results

6 Results

The goal of this section is to present and discuss the results obtained with the simulation of the restart flow. The results are presented in terms of the dimensionless stress ($\boldsymbol{\tau}^*$) field, the normalized fluidity (ϕ_v^*) field, the dimensionless velocities, and the time evolution of the velocity and the fluidity of some specific points of the domain, dissecting the complexity of this kind of flow. The effects of the viscoelasticity (De), the avalanche time (α_t), the construction time ($\mathrm{T}_{c,0}^*$) and the dimensionless imposed pressure gradient (Δp^*) are discussed individually while the other parameters are kept constant.

6.1 The thixotropic viscoplastic flow

The first flow configuration analyzed is the one that considers only the effects of the thixotropic and viscoplastic behaviours, neglecting any viscoelastic effects ($De = 0$). The dimensionless parameters are presented in Table 6. Figure 20 presents the temporal evolution of the dimensionless velocity at the symmetry line of both the narrow and wide channel of the expansion geometry, while Figure 21 presents the temporal evolution of the fluidity at the same locations.

Table 6 – The dimensionless parameters adopted in Section 6.1.

ϕ_0^*	n	$\dot{\gamma}_1^*$	α_t	$\mathrm{T}_{c,0}^*$	De	Δp^*	Re
10^{-3}	0.3	1	10^1	10^4	0	100	1.4

Due to the imposed boundary conditions at the inlet, the flow at the narrow channel simulates an infinite planar channel flow. Thus, the symmetry line of the narrow channel tends to be inside a so-called “plug zone”. This plug zone is characterized by its low stress ($\tau < \tau_0$), low fluidity ($\phi_v \approx \phi_0$) and velocity profile nearly constant. Thus, given the viscoplastic behaviour of the fluid (Equation 4.8), the normalized fluidity of the narrow channel tends to be constant and equals to zero at any point of the symmetry line far enough of the expansion. However, the narrow channel sample point (-5,0) is not far enough from the abrupt expansion, and during the development of the flow, the stress of this point can surpass τ_0, which leads to $\phi_v^* > 0$, even though it is still at least one order of magnitude bellow ϕ_0^*, meaning that $\phi_v \approx \phi_0$ (Equation 4.11). It is important to highlight that the condition $\tau > \tau_0$ for this sample point is true only during a certain period of the simulation, as can be seen in Figure 22, which presents the stress field for different values of t^* and the black zones delimit the regions where $\tau < \tau_0$. On the other hand, the wide channel sample point is always at the region where $\tau < \tau_0$, and all the changes at the ϕ_v^* shown in Figure 21b are due to the advective transport.

Figure 20 – Temporal evolution of the dimesionless velocity at symmetry line for (a) the narrow channel (-5,0) (b) the wide channel (10,0). The adopted dimensionless parameters are presented at Table 6.

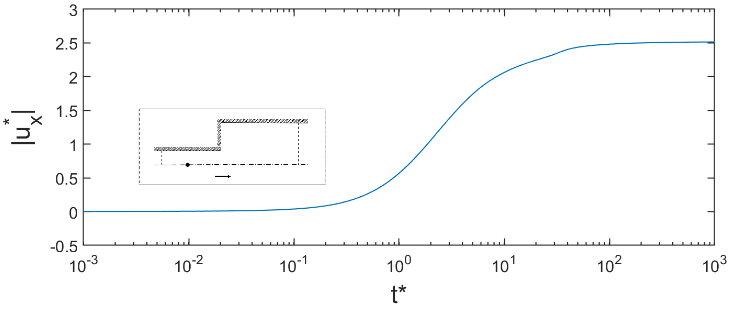

(a) (-5,0)

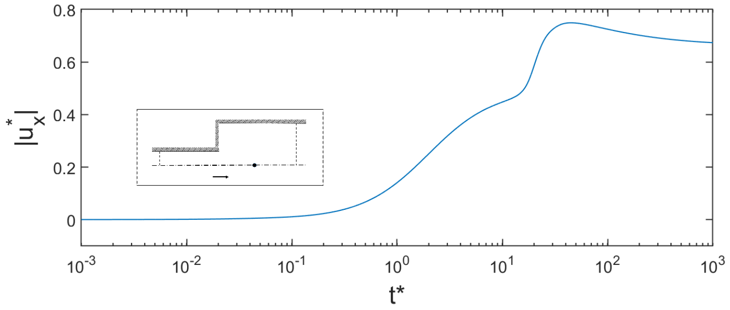

(b) (10,0)

Figure 21 – Temporal evolution of the normalized fluidity at symmetry line for (a) the narrow channel (-5,0) (b) the wide channel (10,0). The adopted dimensionless parameters are presented at Table 6.

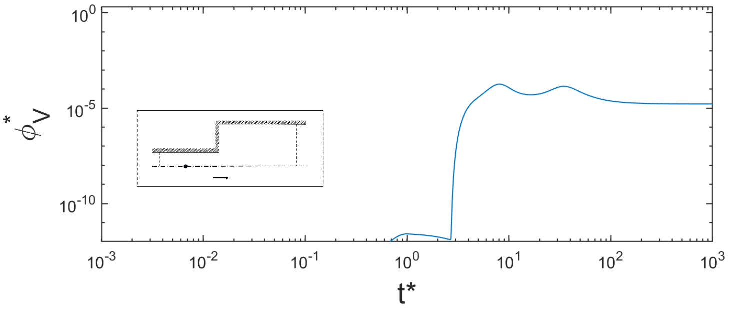

(a) (-5,0)

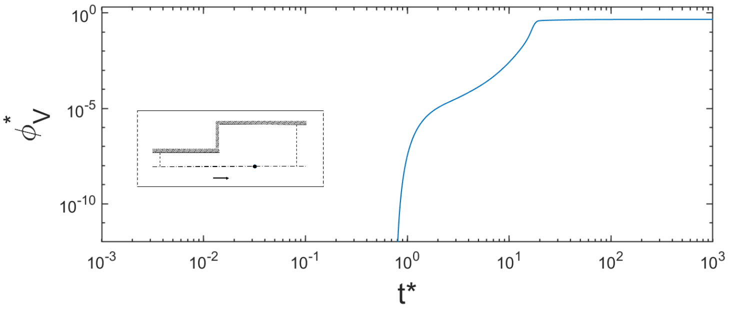

(b) (10,0)

Figure 22 – τ^* for (a) $t^* = 10^{-2}$, (b) $t^* = 10^0$, (c) $t^* = 10^1$, and (d) $t^* = 10^3$. The black areas have $\tau < \tau_0$. The adopted dimensionless parameters are presented at Table 6.

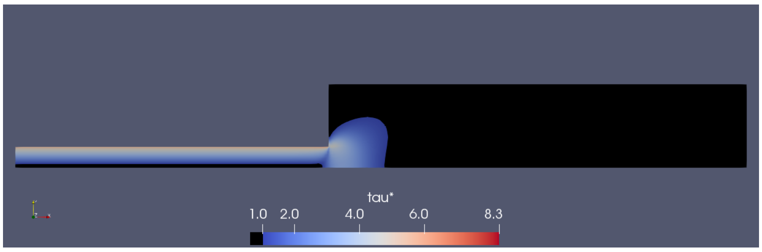

(a) $t^* = 10^{-2}$

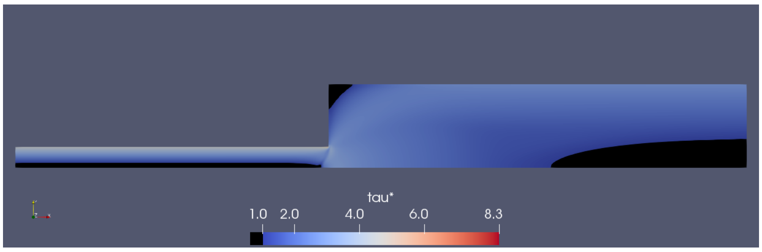

(b) $t^* = 10^0$

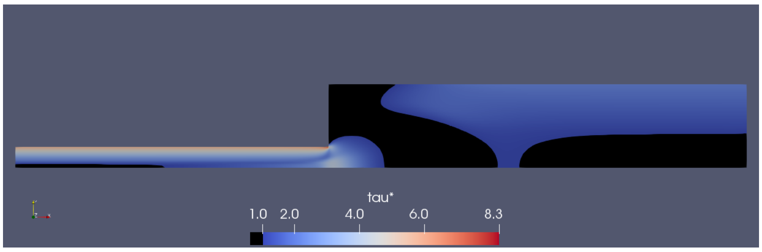

(c) $t^* = 10^1$

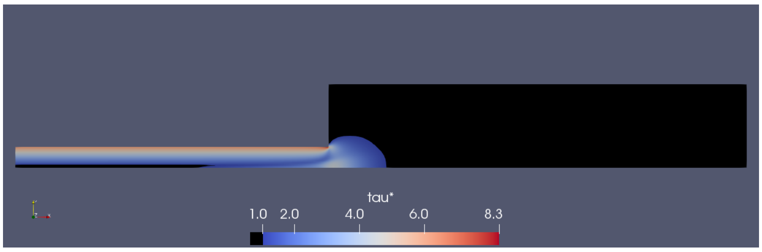

(d) $t^* = 10^3$

As the flow starts at rest and fully structured, at the beginning of the simulation ($t^* < 10^{-1}$) it is almost static. During this time, the internal microstructure of the flow is being broken, but not uniformly, as can be seen in Figure 23. As the flow is almost static, the transport term is almost null, as can be seen in Figure 21b, where the values of ϕ_v^* only start to change at the neighbourhood of $t^* = 10^0$ at the wide channel sample point. Even so, the values of ϕ_v^* are still lower than ϕ_0^* until near $t^* = 10$. This is relevant, as a $\phi_v^* << \phi_0^*$ means that $\phi_v \approx \phi_0$, as can be seen in Equation 4.11. As the time passes, the ϕ_v^* at the narrow channel walls increases, allowing the flow to accelerate.

With a higher fluidity near the narrow channel walls, flow accelerates, as can be seen in Figure 20 between $t^* = 0.1$ and $t^* = 10$. As the flow velocity increases, the

Figure 23 – ϕ_v^* field for (a) $t^* = 10^{-4}$, (b) $t^* = 10^{-3}$, (c) $t^* = 10^{-2}$, (d) $t^* = 10^{-1}$, (e) $t^* = 10^{0}$, (f) $t^* = 10^{1}$, (g) $t^* = 10^{2}$, and (h) $t^* = 10^{3}$. The black areas have $\phi_v^* < 10^{-5}$. The adopted dimensionless parameters are presented at Table 6.

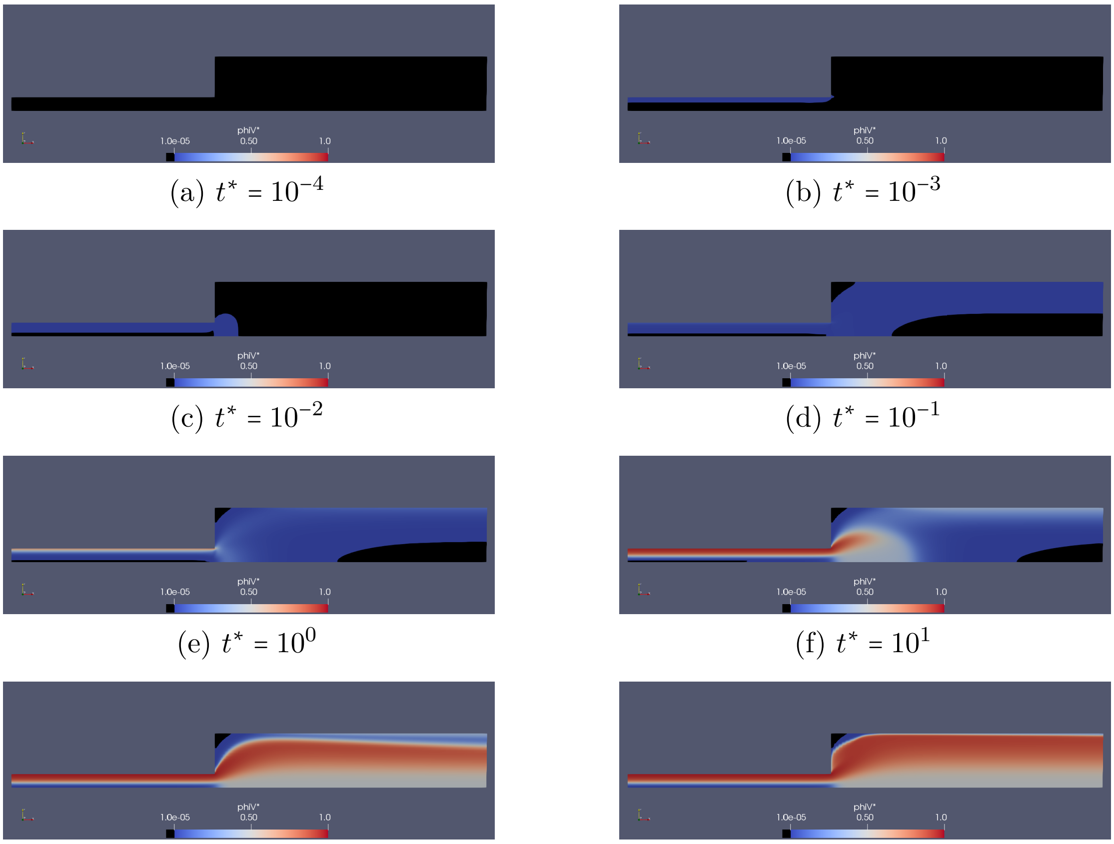

(a) $t^* = 10^{-4}$

(b) $t^* = 10^{-3}$

(c) $t^* = 10^{-2}$

(d) $t^* = 10^{-1}$

(e) $t^* = 10^{0}$

(f) $t^* = 10^{1}$

(g) $t^* = 10^{2}$

(h) $t^* = 10^{3}$

relevance of the transport term of Equation 4.7 increases too, forming a “yielded front” that is transported from the narrow channel through the wide channel, as can be seen in Figure 23f. This yielded front can be identified by the velocity and ϕ_v^* increase near $t^* = 10$ in Figure 20b and Figure 21b, respectively. This yielded front behaviour substantially changes the flow dynamics inside the wide channel, as the local fluidity ϕ_v^* becomes more a reflex of the history of the flow, because of the transport term, than a function of local instantaneous properties, such as the local stress. The driving force of the flow is a constant pressure gradient between the inlet and the outlet. As the yielded front advances, the fluidity increases, increasing the flow rate, enhancing the advective transport and allowing an increase at the narrow channel stress (Figure 22), which, in turn, increases ϕ_v^*. Thus, there is a complex relationship between all these flow parameters.

Another important aspect is that this yielded front advances with different velocities, depending, for example, on the wall distance. This behaviour, combined with the fact that the dimensionless shear stress is always lower at the wide channel when compared to the narrow channel, leads to a fluidity profile where the maximum fluidity is not necessarily near the wall, as expected of a planar channel. The flow tends asymptotically to the planar channel profile, as can be seen in Figure 23. This asymptotic behaviour delays the steady-state condition and can change the velocity profile of the wide channel, even though it is less noteworthy at the narrow channel. As can be seen in Figure 20b, the horizontal velocity at the symmetry line of the wide channel has a maximum value between $t^* = 10$ and $t^* = 100$, and then it starts to decrease. This behaviour is mainly associated with the position of the yielded front: as the higher velocities lie near the symmetry line, the transport term is more relevant at this region, increasing the fluidity and allowing a higher flow rate earlier at the projection of the narrow channel over the wide channel. As the yielded front spreads, the velocity profile becomes less concentrated, decreasing the velocity at the symmetry line without necessarily decreasing the total flow rate. Figure 24 shows the velocity profile at the line $x^* = 15$ for $t^* = 10$, $t^* = 100$, and $t^* = 1000$.

Figure 24 – u_x^* over the line $x^* = 15$ at $t^* = 10$, $t^* = 100$, and $t^* = 1000$. The adopted dimensionless parameters are presented at Table 6.

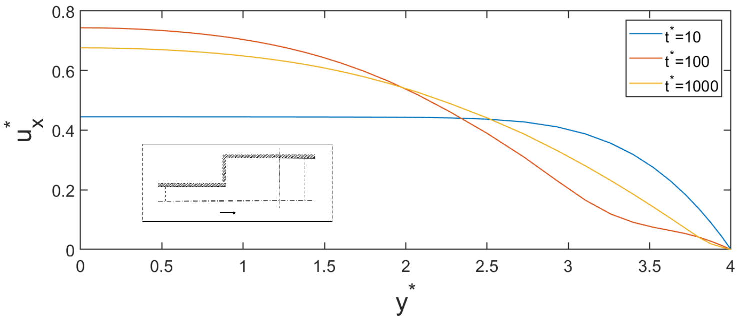

6.2 The TEVP flow

Before analyzing the effects of the α_t, $T^*_{c,0}$ and Δp^*, it is important to discuss the flow patterns of a TEVP flow. The goal of the section is to compare the results of the simulation with $De = 0$ and the simulation with $De = 1$, identifying similarities and differences. The dimensionless parameters are presented in Table 7. Figure 25 and Figure 26 compare the temporal evolution of the velocity and ϕ_v^* for $De = 0$ and $De = 1$ for the expansion geometry, respectively. The main differences can be found at $t^* < 1$, and the flows are almost indistinguishable for $t^* > 10$. This is somewhat expected, as the viscoelastic effects only occur when $\phi_v^* < 10^{-10}$. Thus, the viscoelastic areas decrease as the fluidity increases.

Table 7 – The dimensionless parameters adopted in Section 6.2.

ϕ_0^*	n	$\dot{\gamma}_1^*$	α_t	$T^*_{c,0}$	De	Δp^*	Re
10^{-3}	0.3	1	10^1	10^4	0 and 1	100	1.4

Figure 25 – Temporal evolution of u_x^* at symmetry line of (a) the narrow channel (-5,0) (b) the wide channel (10,0). The adopted dimensionless parameters are presented at Table 7.

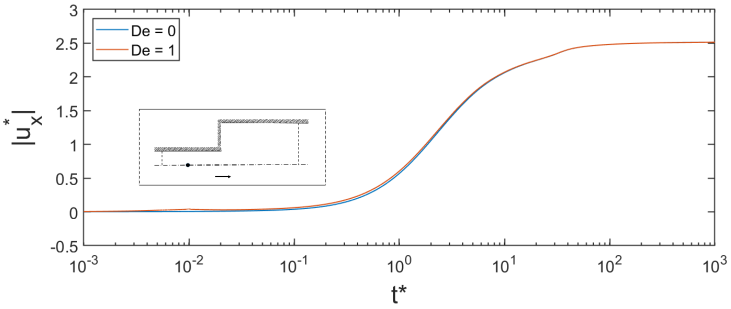

(a) (-5,0)

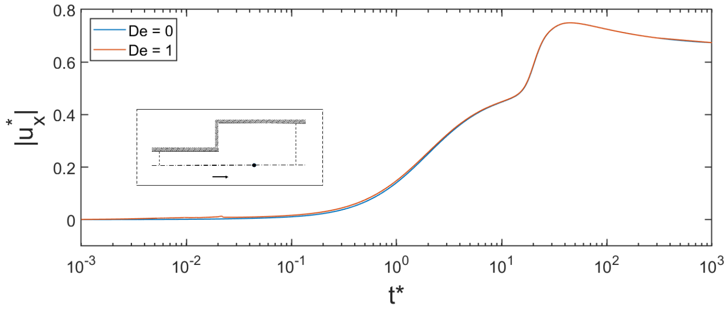

(b) (10,0)

Figure 26 – Temporal evolution of ϕ_v^* at symmetry line of (a) the narrow channel (-5,0) (b) the wide channel (10,0). The adopted dimensionless parameters are presented at Table 7.

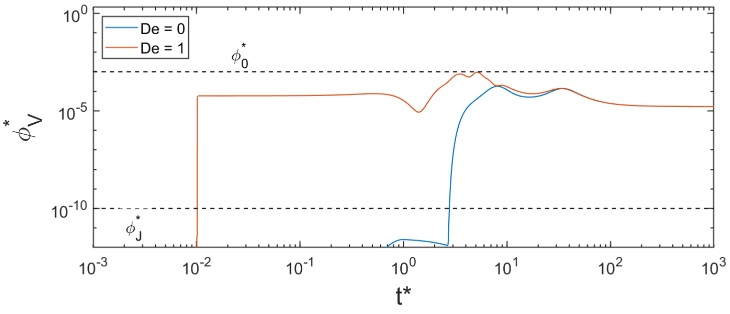

(a) (-5,0)

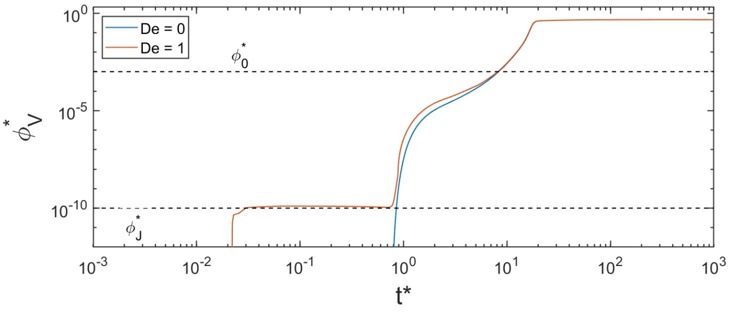

(b) (10,0)

As a general trend, the velocity increases when the viscoelastic behaviour is considered. Figure 27 highlights this difference, comparing the velocities of $De = 0$ and $De = 1$ between $t^* = 10^{-3}$ and $t^* = 10^{-1}$. Even though these velocities are relatively small when compared with the steady-state flow velocities, the $De = 1$ velocity can be one order of magnitude higher than the $De = 0$ velocity. For the adopted configuration, the maximum speed between $t^* = 10^{-3}$ and $t^* = 10^{-1}$ is around 1% and 2% of the steady-state velocity.

Figure 27 – u_x^* for $De = 0$ and $De = 1$ between $t^* = 10^{-3}$ and $t^* = 10^{-1}$ for (a) the narrow channel (-5,0) (b) the wide channel (10,0). The adopted dimensionless parameters are presented at Table 7.

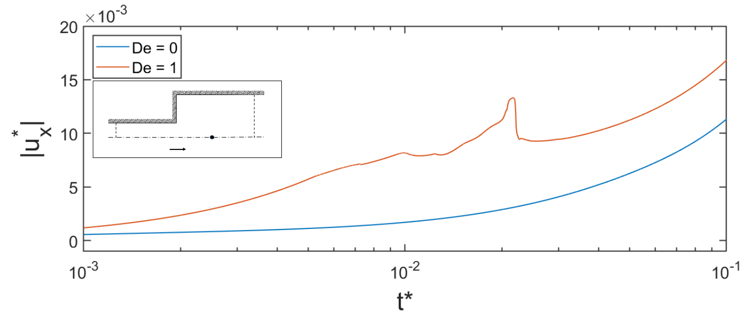

(a) (-5,0)

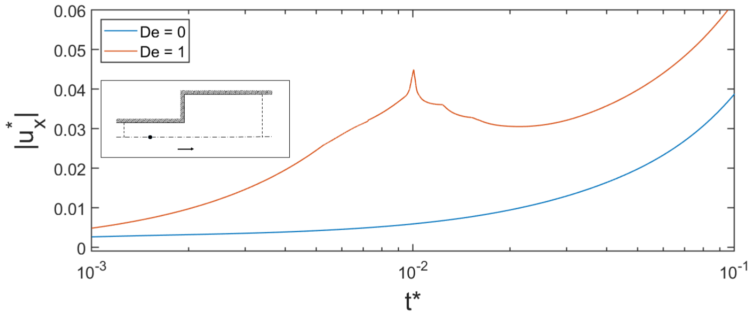

(b) (10,0)

Figure 27 also shows that the $De = 1$ flow presents a velocity decrease during this interval, even at the narrow channel. Comparing Figure 26 and Figure 27, it is possible to identify that the velocity peak of Figure 27 occurs at the exact moment when ϕ_v^* surpasses the $\phi_J^* = 10^{-10}$ mark for both the narrow and wide channels. Thus, the increased velocity is related with to viscoelastic behaviour, and its reduction is related to the absence of the aforementioned behaviour. Assuming a low enough ϕ_0^*, $\phi_s \approx \phi_0 << \phi_\infty$ (Equation 4.4) for structured fluids ($\phi_v^* < 10^{-10}$). This means that Equation 4.5 becomes:

$$\begin{aligned}
&\gamma \approx \gamma_e >> \gamma_v \\
&\dot{\gamma} \approx \dot{\gamma}_e >> \dot{\gamma}_v \\
&\boldsymbol{\tau} = \frac{\dot{\gamma}}{\phi_\infty} + \frac{\dot{\gamma}_v}{\phi_s} + \frac{\gamma_e}{J\left(\phi_v^*\right)}
\end{aligned} \tag{6.1}$$

The behaviour described by Equation 6.1 shows that, assuming a low enough ϕ_0^*, the Jeffreys model tends to behave as a Kelvin-Voigt model, as shown in Figure 28. This model is characterized by a viscous and an elastic element connected in parallel. This means that, under the aforementioned circumstances, the material effectively flows with a fluidity equal to ϕ_∞, that is some orders of magnitude above ϕ_v, explaining the higher acceleration and, consequently, higher velocities. Even though this region shows a viscoelastic behaviour, it is not an issue, as this just happens for a brief moment and the velocities involved are relatively small, thus γ is relatively small. Another issue is that, as soon as τ surpasses τ_0, the microstructure of the material starts to break, leading to $\phi_v^* > 10^{-10}$, when the viscoelastic effects cease abruptly. For this new configuration ($\phi_v^* > 10^{-10}$), $J(\phi_v^*) = 0$ and the adopted Jeffrey model can be simplified as two viscous elements connected in parallel. This analogous mechanical system can be simplified into only one viscous element, with $\phi_v = \phi_s + \phi_\infty$. Under this new scenario, Equation 4.5 is equal to:

Figure 28 – Kelvin-Voigt model analogous mechanical system.

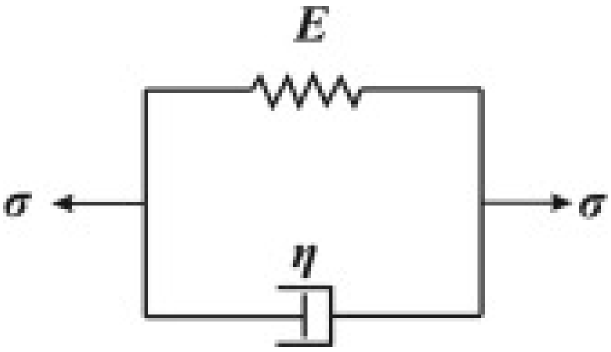

Source: (HAJIKARIMI; Moghadas Nejad, 2021)

$$\begin{aligned} \gamma &= \gamma_v \\ \dot{\gamma} &= \dot{\gamma}_v \\ \boldsymbol{\tau} &= \frac{\dot{\gamma}}{\phi_v} \end{aligned} \tag{6.2}$$

When $J(\phi_v^*) = 0$, the stress equation has only three elements: ϕ_v^*, $\boldsymbol{\tau}$ and $\dot{\gamma}$. ϕ_v^* is associated with the fluidity evolution equation (Equation 4.7), and $\dot{\gamma}$ is mainly associated with the momentum balance equation (Equation 4.20), meaning that they can not change freely within one time step. On the other hand, $\boldsymbol{\tau}$ can change freely, as its time derivative is not part of the stress equation anymore ($J(\phi_v^*) = 0$). This means that, at the moment when a viscoelastic material achieves the condition $\phi_v^* > 10^{-10}$, the effective fluidity of the flow decreases some orders of magnitude (from ϕ_∞ to ϕ_v), while $\dot{\gamma}$ is somewhat constant due to its bonds with other equations. This configuration leads to a stress peak, which accelerates the breakup process, and after a few time steps the increased fluidity and lower $\dot{\gamma}$ allow the stress to decrease. All this described phenomenon happens at a fraction of t_c, but the microstructure breakup can be relevant for a significant part of the simulation, and can provoke the breakup of regions that would not be broken if the viscoelastic forces were not considered. Figure 26 shows that both the narrow and the wide channel fluidities surpass 10^{-10} before its counterparts at the $De = 0$ simulation. The stress peak is one of the reasons why it is common that the ϕ_v^* time evolution is almost vertical when it surpasses the 10^{-10} mark when the viscoelastic behaviour is considered. Figure 29 compares the ϕ_v^* field of the $De = 0$ and $De = 1$ at the $t^* = 0.1$. The minimum ϕ_v^* at the $De = 1$ simulation narrow channel is higher than 10^{-5}, even at the symmetry line, and the $\phi_v^* < 10^{-5}$ zones at the wide channel have substantially decreased.

Figure 29 – ϕ_v^* field at $t^* = 10^{-1}$ for (a) $De = 0$, (b) and $De = 1$. The adopted dimensionless parameters are presented at Table 7.

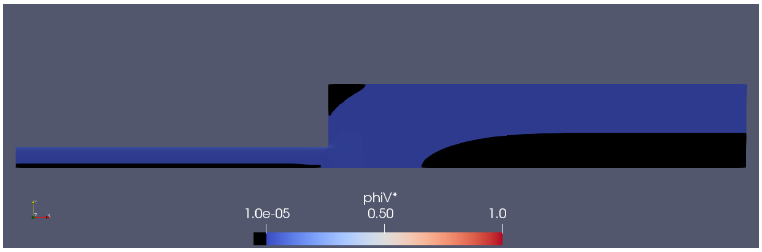

(a) $De = 0$

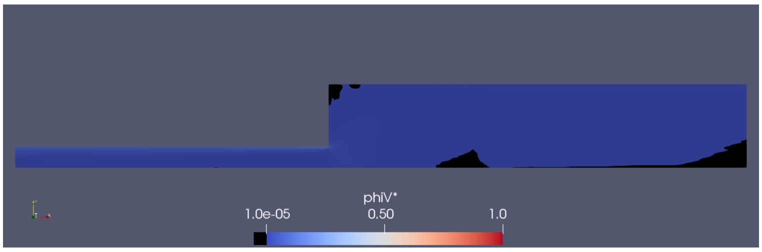

(b) $De = 1$

A few points must be considered about this stress peak: first and more importantly, the value of ϕ_0^* of the present work was chosen due to a numeric reason. Other works in the literature (DE SOUZA MENDES; ABEDI; THOMPSON, 2018; SIQUEIRA; PASQUALI; DE SOUZA MENDES, 2020; CUNHA; DE SOUZA MENDES; SIQUEIRA, 2020) considered lower values of ϕ_0^*, which would change the range $\phi_v^* < \phi_0^*$, allowing this stress peak to be more relevant. The second point is that the Heaviside function adopted for $J(\phi_v^*)$ (Equation 4.19) is a discontinuous function, making the transition between the elastic and the inelastic behaviour more abrupt. A continuous function would decrease the stress peak, even though it would not prevent it if this function changes fast enough. Third, the stress peak can accelerate the breakup process of regions that would take much more time to be broken, or even not broken at all. Figure 26b, for example, shows that ϕ_v^* at the point (10,0) surpasses 10^{-10} almost 100 times faster (from $t^* \approx 10^0$ to $t^* \approx 10^{-2}$) when the viscoelastic behaviour is considered. Fourth: as this stress peak lasts only a fraction of the time, this behaviour is numerical challenging. The involved time derivatives can be really high, and a poorly dimensioned time step would lead to an unreal increase in fluidity, for example. Figure 29 illustrates this numerical difficulty, the $\phi_v^* < 10^{-5}$ zones have smooth borders for $De = 0$, while at $De = 1$ the borders are far more irregular. The main reason for this difference is the difficulty to precisely calculating the flow parameters at this period.

Figure 26 also shows that the values of ϕ_v^* can be really unstable between $10^{-10} < \phi_v^* < 10^{-3}$, showing oscillations and a complex behaviour. As already discussed, when $\phi_v^* > 10^{-10}$, the viscoelastic effects are null, and when $\phi_v^* << \phi_0^*$, $\phi_v \approx \phi_0$, meaning that the exact value of ϕ_v^* has little to no impact over the other equations (Equation 4.1 and Equation 4.20). Another issue is that a variation of about 3% at the dimensionless stress field can change the value of ϕ_{eq}^* from zero to 10^{-5}, and another increase of 3% at the dimensionless stress field leads to $\phi_{eq}^* \approx 10^{-4}$. This way, it is expected that the value of ϕ_v^* will fluctuate when its exact value lies between $10^{-10} < \phi_v^* < 10^{-3}$, but this variation does not compromise the accuracy of the simulation.

6.2.1 The compliance model

To illustrate the influence of the choice of a Heaviside function adopted for the compliance model, a second compliance model is considered in the present section. Figure 30 and Figure 31 compare two simulations with exactly the same dimensionless parameters, but considering two different values of ϕ_J^*: (Equation 4.19) one with the value of 10^{-10} and the other equal to 1. The adopted geometry is the expansion, and the dimensionless quantities are shown in Table 8. These are the only results presented in this thesis that do not consider $\phi_J^* = 10^{-10}$. As the maximum value of ϕ_v^* is equal to one, it means that $J(\phi_v^*) = J_0$ for all the domain. Nevertheless, Equation 4.2 shows that λ_1 still decreases with the increase of ϕ_v^*.

Table 8 – The dimensionless parameters adopted in Section 6.2.1.

ϕ_0^*	n	$\dot{\gamma}_1^*$	α_t	$\mathrm{T}_{c,0}^*$	De	Δp^*	Re
10^{-3}	0.3	1	10^1	10^4	1	100	1.4

Figure 30 shows the velocity oscillations, a characteristic of viscoelastic flows, at least for some time. The flow with $\phi_J^* = 1$ also tends to the flow with $\phi_J^* = 10^{-10}$. Combining Equation 4.21 and Equation 4.2, it is possible to conclude that the increase of the fluidity decreases the De, even when $J(\phi_v^*)$ is a constant function. Besides, as the flow starts at rest and fully structured, the moment when the elastic forces are higher (due to the flow being fully structured) is also the moment where the viscous forces are higher (due to the low fluidity characteristic of the fully structured material), decreasing the influence of

Figure 30 – Influence of the ϕ_J^* over the temporal evolution of the u_x^* at the symmetry line of (a) the narrow channel (-5,0) and (b) the wide channel (10,0). The adopted dimensionless parameters are presented in Table 8.

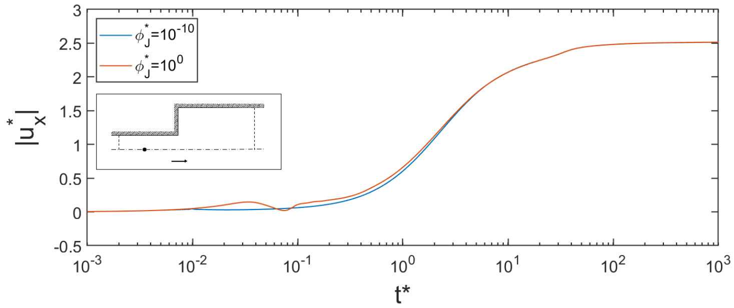

(a) (-5,0)

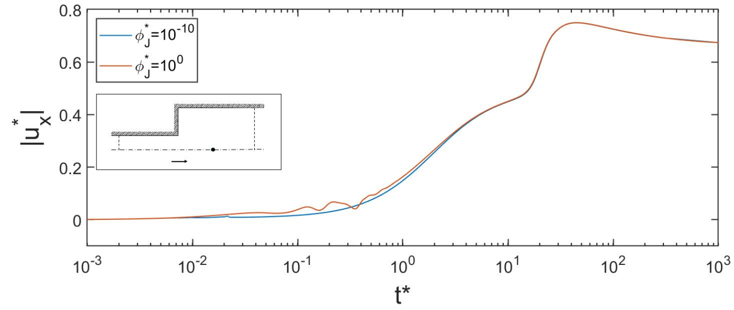

(b) (10,0)

Figure 31 – Influence of the ϕ_J^* over the temporal evolution of the ϕ_v^* at the symmetry line of (a) the narrow channel (-5,0) and (b) the wide channel (10,0). The adopted dimensionless parameters are presented in Table 8.

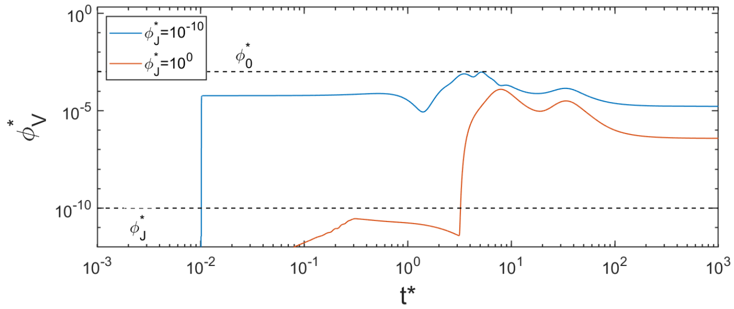

(a) (-5,0)

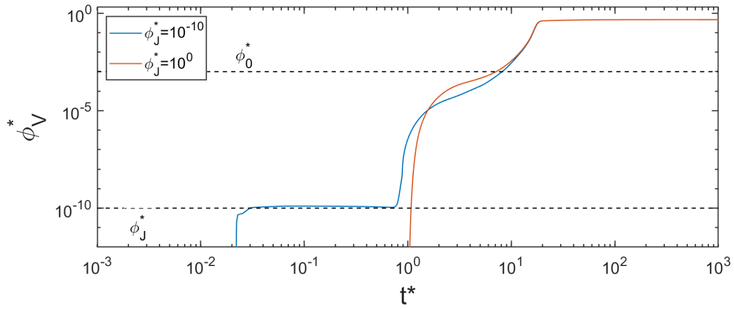

(b) (10,0)

the viscoelastic forces over the flow. Finally, as already discussed, the elastic behaviour has different time scales than the thixotropy behaviour, thus it is somewhat expected the elastic forces would be more relaxed when the thixotropy starts to show steady-state characteristics.

Without the stress peak provoked when the viscoelastic effects cease abruptly, the ϕ_v^* evolution for $\phi_J^* = 1$ in Figure 31 presents some similarities with Figure 26, which shows the ϕ_v^* evolution of the $De = 0$ simulation, such as the moment when they surpass the $\phi_v^* = 10^{-10}$ mark for both the narrow and wide channel. Furthermore, the $\phi_J^* = 1$ flow tends to have a higher velocity than the $\phi_v^* = 10^{-10}$, specially for $t^* < 10^1$. This behaviour corroborates the conclusion that increasing the viscoelastic behaviour tends to increase the velocity at the beginning of the simulation.

6.3 The influence of the De

Figure 32 and Figure 33 show the results for four different Deborah numbers: 0, 0.1, 1, and 10, adopting the expansion geometry and the dimensionless parameters presented in Table 9. As already discussed, the influence of the viscoelastic forces is limited by the $\phi_v^* < 10^{-10}$ condition, which means that as soon as the microstructure starts to break the viscoelastic effects are interrupted. Thus, the effects of increasing the De are only shown at relatively small times ($t^* < 10$). During this time, the higher the De, the higher the u_x^*, even though the simulations tend to have the same velocity at the steady-state. Also, increasing De from $De = 0.1$ to $De = 10$ increases the relaxation time and $J(\phi_v^*)$, which delays the τ growth and allows the narrow channel to stay longer at the condition $\phi_v^* < 10^{-10}$, as can be seen in Figure 33.

Table 9 – The dimensionless parameters adopted in Section 6.3.

ϕ_0^*	n	$\dot{\gamma}_1^*$	α_t	$\mathrm{T}_{c,0}^*$	De	Δp^*	Re
10^{-3}	0.3	1	10^1	10^4	0 to 10	100	1.4

Figure 33 also shows the temporal evolution of ϕ_v^* has a plateau between $t^* = 5 * 10^{-3}$ and $t^* 3 * 10^{-1}$ for $De = 0.1$. This plateau is apparently below ϕ_J^*, and the ϕ_v^* evolution curve does not present the almost vertical behaviour when it surpasses ϕ_J^*. The main reason for this behaviour is an interpolation error: the present work adopts a FVM method, which means the flow properties are calculated at the centroid of the volumes. Figure 33 shows the ϕ_v^* values at the symmetry line of the geometry, thus an interpolation method is adopted to obtain the property value at the boundary of the volume. The centroid of the volume has $\phi_v^* > \phi_J^*$, but due to the interpolation scheme adopted, the ϕ_v^* value at the symmetry line does not. Usually, the error introduced by the interpolation scheme can be considered small, but the values of ϕ_v^* in this region are quite small too, making

Figure 32 – Influence of the De over the temporal evolution of u_x^* at symmetry line of (a) the narrow channel (-5,0) and (b) the wide channel (10,0) of the expansion geometry. The adopted dimensionless parameters are presented in Table 9.

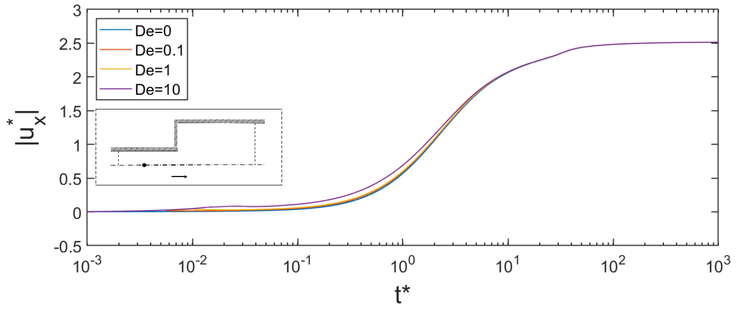

(a) (-5,0)

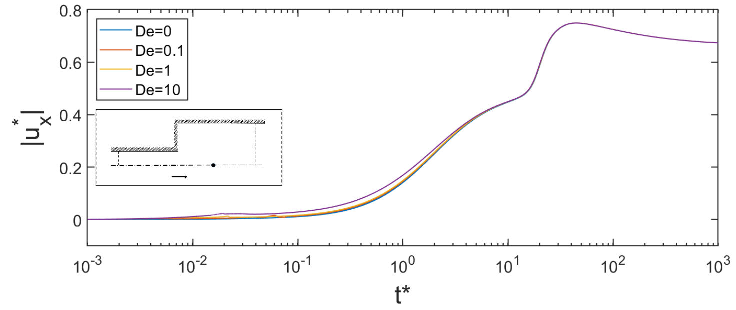

(b) (10,0)

Figure 33 – Influence of the De over the temporal evolution of ϕ_v^* at symmetry line of the narrow channel (-5,0) of the expansion geometry. The adopted dimensionless parameters are presented in Table 9.

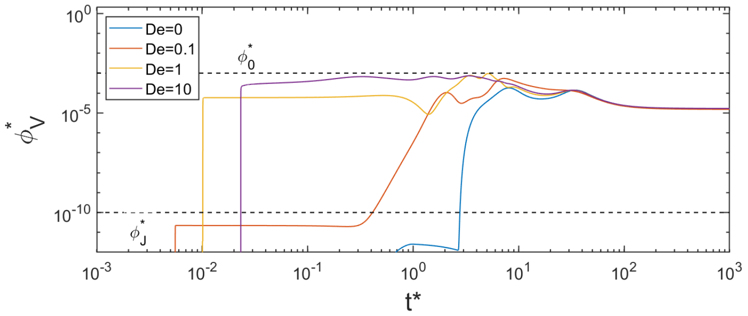

the interpolation errors relevant to the graph. These values are only used during the post-processing phase, thus they do not influence the simulation.

Another identifiable behaviour in Figure 32 is that a lower relaxation time leads to a lower stress peak when ϕ_v^* surpasses 10^{-10}, which in turn preserves more of the wide channel material under the condition of $\phi_v^* < 10^{-10}$ after the stress peak. Figure 34 shows an interval of Figure 32, highlighting the velocity oscillations at the wide channel between $t^* = 10^{-3}$ and $t^* = 10^{-1}$, specially for $De = 0.1$. These oscillations are provoked by the interaction between inelastic and viscoelastic zones. In theory, every simulation with $De > 0$

has a time interval where the domain can be divided between inelastic and viscoelastic parts, but the stress peak can break down the majority of the viscoelastic zones before the interaction between them can produce any visible effects.

Figure 34 – u_x^* oscillations between $10^{-2} < t^* < 10^{-1}$ at the expansion geometry wide channel. The adopted dimensionless parameters are presented in Table 9.

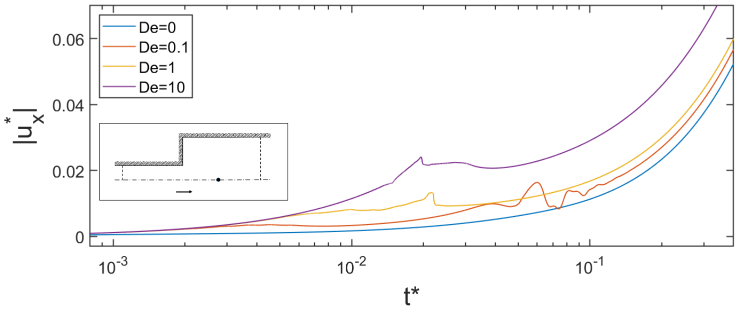

Figure 35 – Influence of the De over the temporal evolution of u_x^* at symmetry line of (a) the wide channel (-10,0) and (b) the narrow channel (5,0) of the contraction geometry. The adopted dimensionless parameters are presented in Table 9.

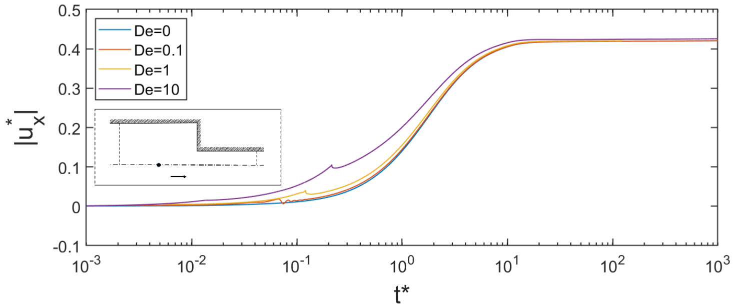

(a) (-10,0)

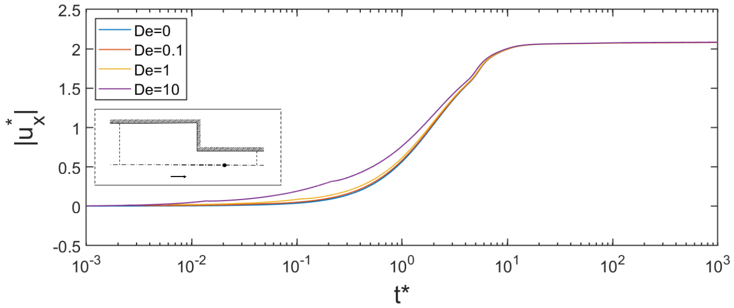

(b) (5,0)

The contraction geometry results follow the same trend that the expansion results have shown, as can be seen in Figure 35 and Figure 36: the higher the De, the higher the u_x^* at relatively small times ($t^* < 10$), and increasing De from 0.1 to 10 delays the moment when the stress peak occurs. The simulation with $De = 0.1$ had a lower stress peak, and kept a larger portion of its domain under the $\phi_v < 10^{-10}$. This way, the effects of the viscoelastic forces are more evident at $De = 0.1$ than at $De = 10$, as can be seen in Figure 37.

Figure 36 – Influence of the De over the temporal evolution of ϕ_v^* at symmetry line of the narrow channel (5,0) of the contraction geometry. The adopted dimensionless parameters are presented in Table 9.

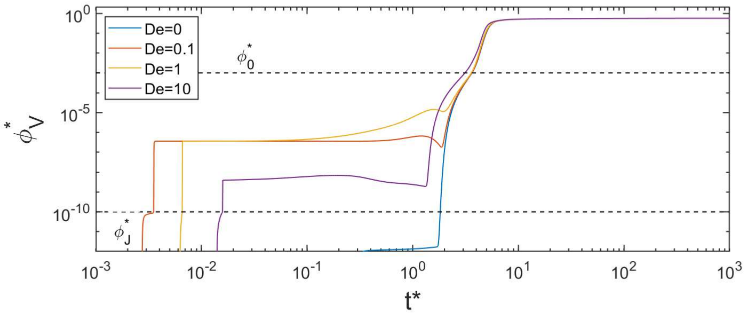

Figure 37 – Effects of the viscoelastic forces cease over u_x^* and the oscillations produced by the interaction between the viscoelastic part and the purely viscous part of the flow. u_x^* obtained at the point (-10,0) of the wide channel. The adopted dimensionless parameters are presented in Table 9.

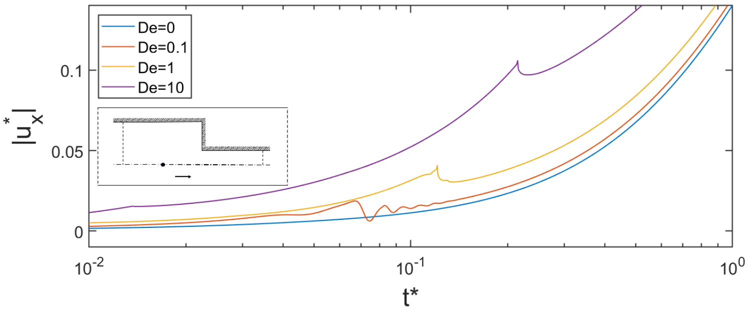

6.4 The influence of the α_t

As the material starts fully structured, it must first break down the internal structure before it starts to flow, meaning that α_t is one of the main rheological parameters of the simulations presented in this thesis. A higher α_t means that the structure takes longer to break, usually increasing the time needed to achieve the steady-state. Figure 38 shows the horizontal velocity at the expansion geometry for α_t equal to: 10^0, 10^1, 10^2, 10^3, and 10^4. The dimensionless parameters adopted in the present section are shown in Table 10.

For low values of α_t, such as 10^0 and 10^1, there is a clear yielded front, where the unstructured material of the narrow channel is transported through the wide channel,

Table 10 – The dimensionless parameters adopted in Section 6.4.

ϕ_0^*	n	$\dot{\gamma}_1^*$	α_t	$\mathrm{T}_{c,0}^*$	De	Δp^*	Re
10^{-3}	0.3	1	10^0 to 10^4	10^4	1	100	1.4

Figure 38 – Influence of α_t over the temporal evolution of u_x^* at symmetry line of (a) the narrow channel (-5,0) and (b) the wide channel (10,0) at the expansion geometry. The adopted dimensionless parameters are presented in Table 10.

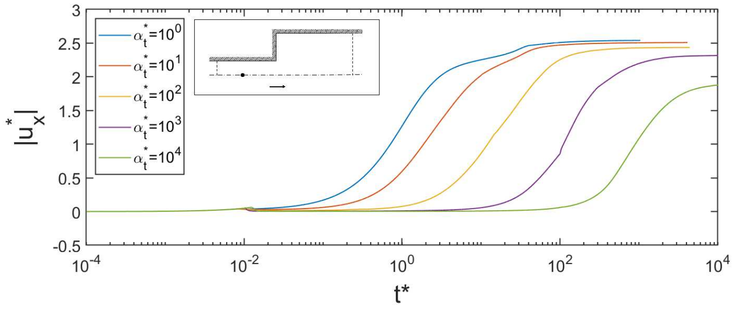

(a) (-5,0)

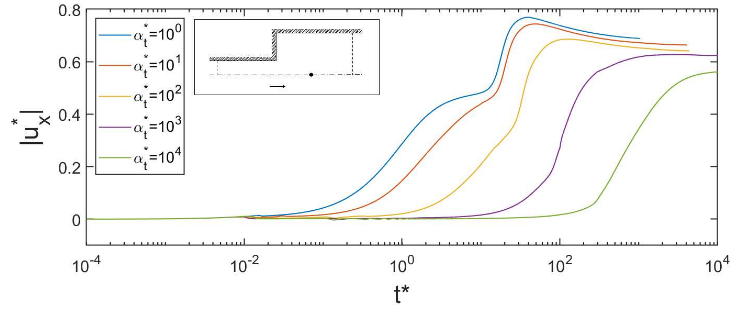

(b) (10,0)

increasing the fluidity and the flow velocity as it advances. On the other hand, for higher α_t values, the flow takes more time to break and to accelerate, meaning that the yield front is diluted over time, specially because the velocities are lower. This behaviour can be seen in Figure 39, where the temporal evolution of the ϕ_v^* for $\alpha_t = 10^4$ not only takes more time to surpass the $\phi_v^* > \phi_0^*$ mark, but also kept growing continuously after the almost vertical growth characteristic of the yield front.

Figure 40 shows an example of this diluted yield front, assuming $\alpha_t = 10^3$ and $t^* = 100$. Figure 23f shows the ϕ_v^* field for $\alpha_t = 10^1$ and $t^* = 10$. Comparing it with Figure 40 clearly shows that the yield front of $\alpha_t = 10^3$ has a lower ϕ_v^* value, besides its t^* being ten times bigger.

Another important aspect of Figure 39 is that the ϕ_v^* values at the steady-state decrease as the α_t increases. As already discussed, the inlet boundary conditions are set to simulate an infinite planar channel, meaning that the transport term of Equation 4.7 is null and the value of ϕ_v^* can be determined using only local parameters. However, the same is not true for the expansion region. The expansion region has a higher stress than

Figure 39 – Influence of α_t over the temporal evolution of ϕ_v^* at symmetry line of the wide channel (10,0) at the expansion geometry. The adopted dimensionless parameters are presented in Table 10.

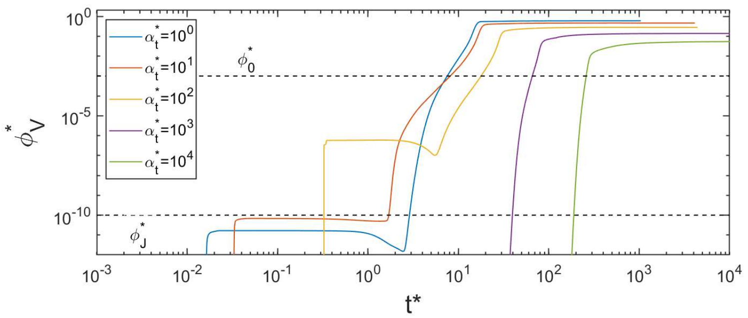

Figure 40 – ϕ_v^* field for $\alpha_t = 10^3$ and $t^* = 100$ at the expansion geometry. The adopted dimensionless parameters are presented in Table 10.

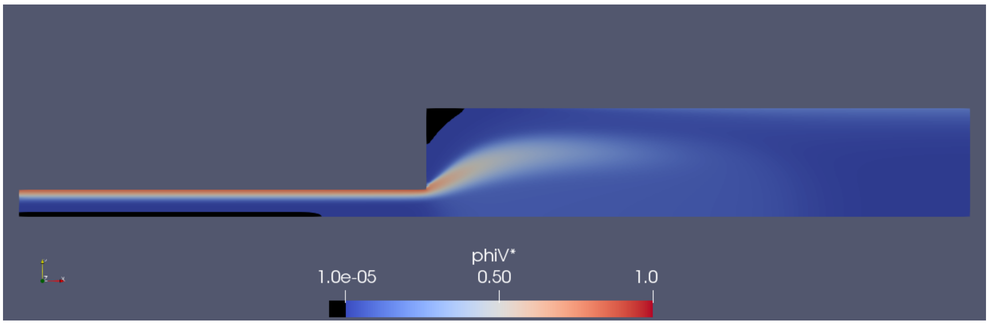

the narrow channel, leading to microstructure breakdown and making the transport term non-null. The microstructure breakdown is not instantaneous and its velocity is directly influenced by α_t (Equation 4.18). As the flow advances to the steady-state, the velocities at the expansion increase, meaning that, when α_t is high enough, there is not enough time to $\phi_v^* \rightarrow \phi_{eq}^*$. Figure 41 shows the stress field for $\alpha_t = 10^3$ and $t^* = 1000$, where the black areas have $\tau < \tau_0$.

Figure 41 – Stress field for $\alpha_t = 10^3$ and $t^* = 1000$ at the expansion geometry. The adopted dimensionless parameters are presented in Table 10.

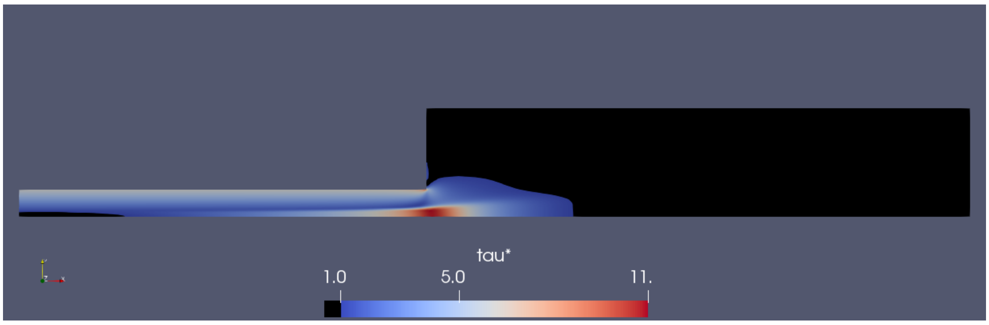

Figure 42 shows u_x^* temporal evolution for different values of α_t in the contraction geometry. As observed at the expansion geometry, increasing α_t decreases the velocity and delays the steady-state, but the contraction geometry results show a higher effect of the α_t variation.

Figure 42 – Influence of α_t over the temporal evolution of u_x^* at symmetry line of (a) the wide channel (-10,0) and (b) the narrow channel (5,0) at the contraction geometry. The adopted dimensionless parameters are presented in Table 10.

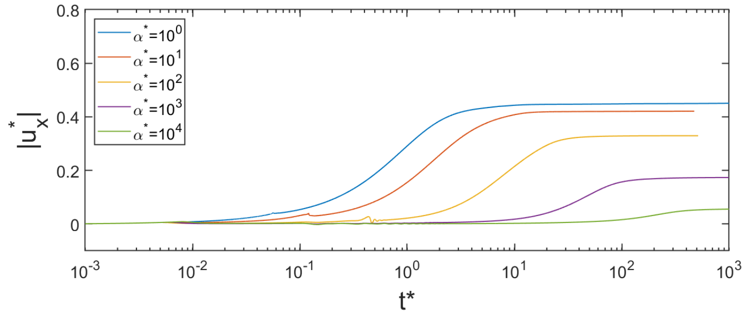

(a) (-10,0)

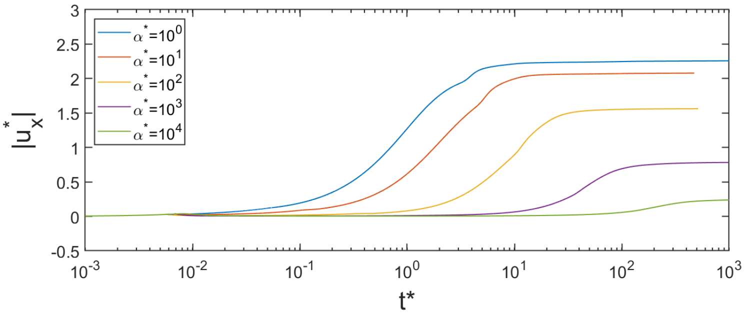

(b) (5,0)

Figure 43 – τ field for $\alpha_t = 10^4$ at $t^* = 10^3$ at the contraction geometry. The adopted dimensionless parameters are presented in Table 10.

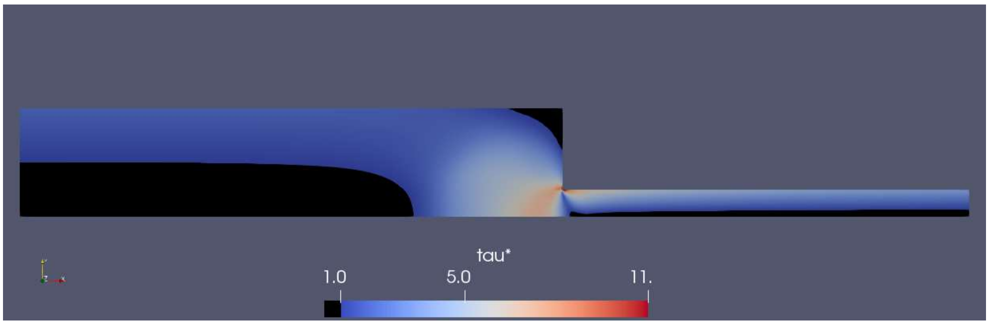

As can be seen in Figure 43, at the contraction geometry, the material near the walls flows from a relatively low-stress zone (the wide channel) to a relatively high-stress zone (the contraction and the narrow channel). This increase in the stress levels led to an increase at ϕ_{eq}^* and, consequently, ϕ_v^*. However, this increase at ϕ_v^* is not instantaneous and depends on the α_t values. A higher α_t means the microstructure needs more time to be broken. This way, it is possible to have an “entrance length” for ϕ_v^* at the narrow channel, where the microstructure is being continuously broken and transported. This region has a lower fluidity, which decreases the flow rate. On the other hand, the region near the symmetry line can have $\phi_v^* > \phi_{eq}^*$ at the narrow channel, meaning that the material microstructure is being recovered at this region. However, the effects of fluidity near the symmetry line are lower than the effects of the fluidity near the walls. Figure 44 shows the ϕ_v^* field for different values of α_t at $t^* = 10^3$.

Figure 44 – ϕ_v^* field for (a) $\alpha_t = 10^0$, (b) $\alpha_t = 10^3$, and (c) $\alpha_t = 10^4$ at $t^* = 10^3$ at the contraction geometry. The adopted dimensionless parameters are presented in Table 10.

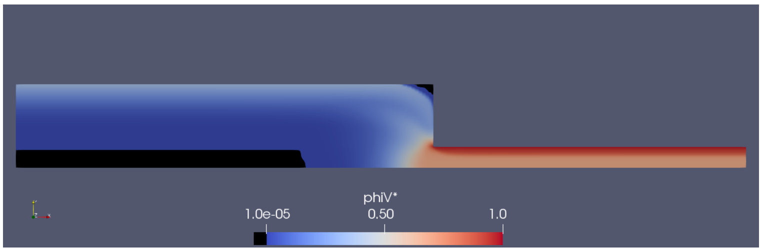

(a) $\alpha_t = 10^0$

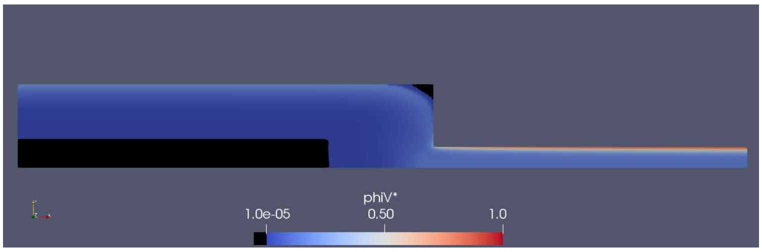

(b) $\alpha_t = 10^3$

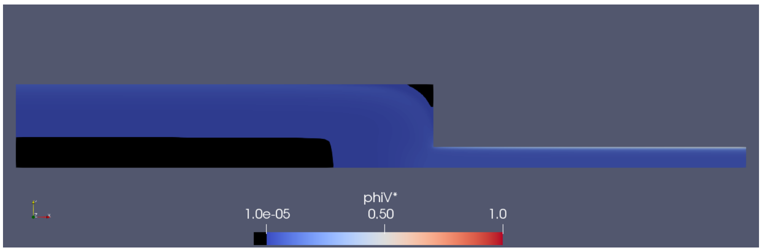

(c) $\alpha_t = 10^4$

Comparing the results for the expansion geometry (Figure 38) and the contraction geometry (Figure 42), it is possible to identify two main differences between the flow behaviours. First, there is no clear evidence of the yield front behaviour in Figure 42, and, second, the contraction geometry flow achieves a steady-state faster than its counterpart at the expansion geometry. The main reason for these differences is the fact that, at the contraction geometry, the material microstructure is been continuously broken. It is possible to identify a yield front at the contraction geometry, as can be seen in Figure 45, but its fluidity is still lower than ϕ_{eq}^* at the narrow channel walls, thus its impact over the contraction flow is lower than its effects at the expansion geometry. Besides that, the stress field is more stable and diluted at the contraction geometry, which helps it to achieve a steady-state. At the contraction geometry, the wall stress is always higher than τ_0 (Figure 43), for both the wide and the narrow channel.

Figure 45 – Example of yield front for $\alpha_t = 10^0$ at $t^* = 3.54$ at the contraction geometry. The adopted dimensionless parameters are presented in Table 10.

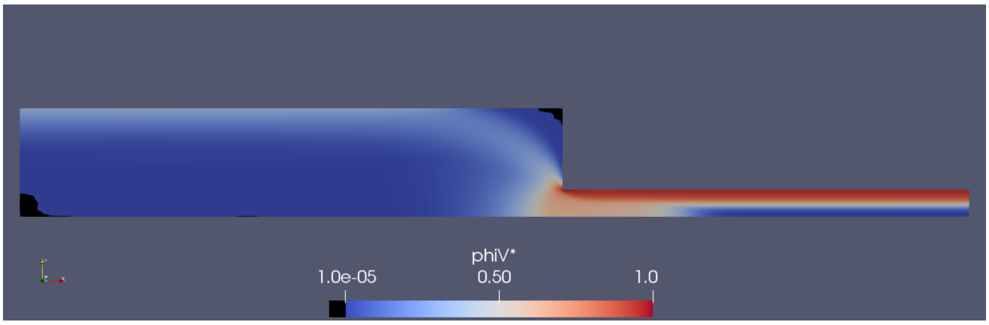

Due to the boundary conditions adopted, the inlet channel simulates an infinite planar channel. At the expansion geometry, the inlet channel is the narrow channel, which has a relatively high stress. This way, the material enters the domain already with high fluidity, and the advective term transports this high fluidity over the wide channel, allowing the material to flow even with $\tau < \tau_0$ at the wide channel and concentrating the stress field at the narrow channel. On the other hand, for the contraction geometry, the inlet channel is the wide channel, with a relatively low stress even at its walls. Thus, the material enters the domain with a lower fluidity and it is continuously broken through the contraction and the narrow channel. For this reason, the influence of α_t is increased at the contraction geometry.

6.5 The influence of the $\mathrm{T}^*_{c,0}$

In Section 4.1, it was discussed that the breakup time and the construction time of the thixotropy are modelled in different ways. As can be seen in Equation 4.18, the build up process is way more linear than the avalanche effect, which can lead to a sudden microstructure collapse. Besides that, the material starts fully structured, thus it needs to be broken first, and only after that, the construction dimensionless time can show its effects. This way, it was expected that all simulations varying $\mathrm{T}^*_{c,0}$ would have a similar behaviour for lower values of t^*, and only at higher t^* they would show different behaviours. Figure 46 shows the influence of the $\mathrm{T}^*_{c,0}$ over the temporal evolution of u^*_x for $\mathrm{T}^*_{c,0}$ equal to 10^{-1}, 10^0, 10^1, 10^2, 10^3, and 10^4 at the expansion geometry. The dimensionless parameters are presented in Table 11.

Table 11 – The dimensionless parameters adopted in Section 6.5.

ϕ^*_0	n	$\dot{\gamma}^*_1$	α_t	$\mathrm{T}^*_{c,0}$	De	Δp^*	Re
10^{-3}	0.3	1	10^1	10^{-1} to 10^4	1	100	1.4

Figure 46 – Influence of $\mathrm{T}^*_{c,0}$ over the temporal evolution of u^*_x at symmetry line of (a) the narrow channel (-5,0) and (b) the wide channel (10,0) at the expansion geometry. The adopted dimensionless parameters are presented in Table 11.

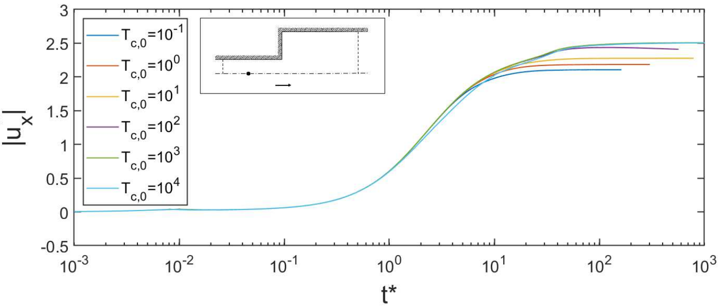

(a) (-5,0)

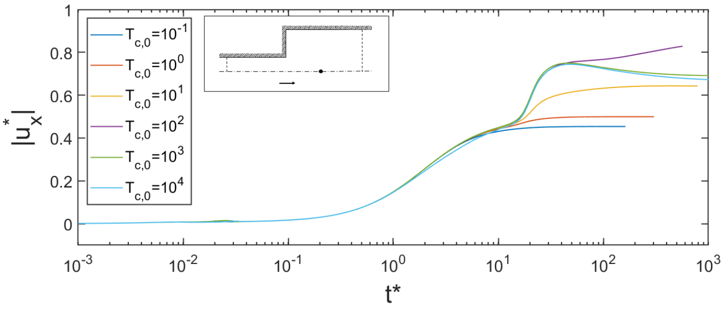

(b) (10,0)

The lower the $\mathrm{T}^*_{c,0}$, the faster the microstructure recovers, and the faster $\phi^*_v \rightarrow \phi^*_{eq}$, if $\phi^*_v > \phi^*_{eq}$. Thus, when decreasing $\mathrm{T}^*_{c,0}$, ϕ^*_v tends to decrease, decreasing the velocity of the flow too. This effect is clear at the narrow channel velocities (Figure 46a), but the wide channel velocities show a more complex behaviour (Figure 46b). Decreasing $\mathrm{T}^*_{c,0}$ increases the relevance of the build up term in Equation 4.7, to the point where there is no clear sign of the yield front at the u^*_x temporal evolution for $\mathrm{T}^*_{c,0}$ equal to 10^{-1} and 10^0. The yield front behaviour described in the present work is only possible due to a combination of the breakup term and the advective term of Equation 4.7. Increasing the relevance of the build up term can make the yield front disappear, as the material microstructure can recover faster than the flow can transport the unstructured material. From $\mathrm{T}_{c,0} = 10^1$ to 10^4, there is a clear influence of the yield front. The $\mathrm{T}_{c,0} = 10^3$ and $\mathrm{T}_{c,0} = 10^4$ curves show the behaviour previously explained, where the yield front advances with different velocities at the domain, leading to a more uniform velocity profile, decreasing the velocity at the symmetry line without necessarily decreasing the flow rate.

The stress field at the wide channel is higher when $\mathrm{T}^*_{c,0}$ equal to 10^{-1}, 10^0 and 10^1. Figure 47 shows the dimensionless stress field for $\mathrm{T}_{c,0} = 10^{-1}$ and $t^* = 1000$. The black areas have $\tau < \tau_0$. On the other hand, Figure 22 shows a simulation for $\mathrm{T}_{c,0} = 10^4$ that has the $\tau < \tau_0$ condition at the whole wide channel at $t^* = 1000$. When the $\mathrm{T}^*_{c,0}$ is high enough, the low-stress condition is not an issue, as the material does not have enough time to recover and it is possible to maintain the flow due to the unstructured material from the narrow channel transported through the wide channel. The higher stress at the wide channel for $\mathrm{T}^*_{c,0} \leq 10^1$ reduces the stress at the narrow channel, decreasing the fluidity in it and slowing down the flow, as can be seen in Figure 46.

Figure 47 – Stress field for $\mathrm{T}_{c,0} = 10^{-1}$ and $t^* = 1000$ at the expansion geometry. The adopted dimensionless parameters are presented in Table 11.

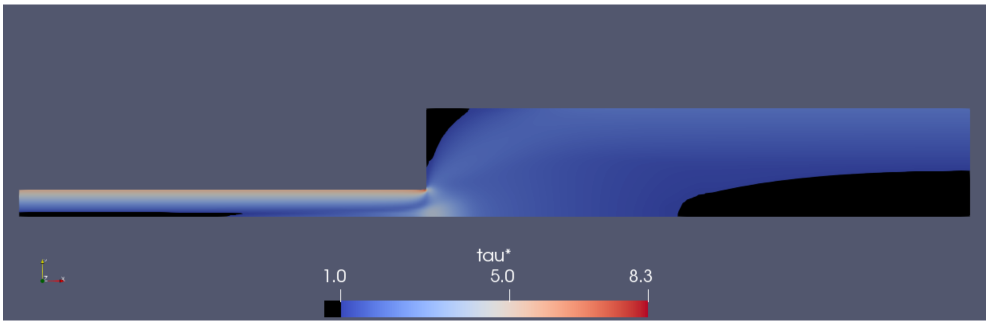

Figure 48 – ϕ^*_v for $\mathrm{T}_{c,0} = 10^2$ and (a) $t^* = 100$ and (b) $t^* = 650$ at the expansion geometry. The adopted dimensionless parameters are presented in Table 11.

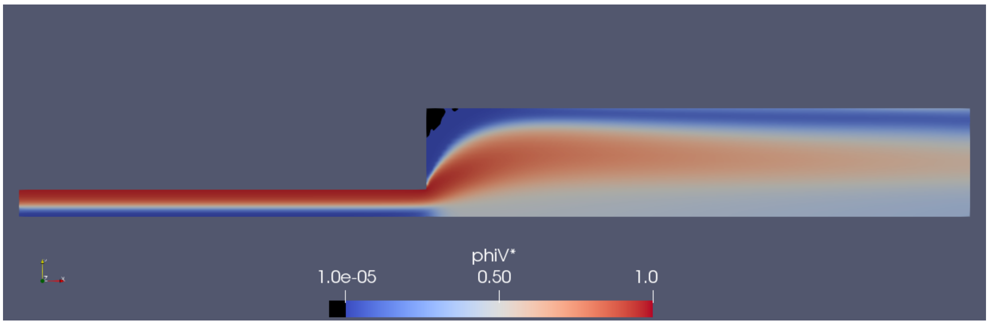

(a) $t^* = 100$

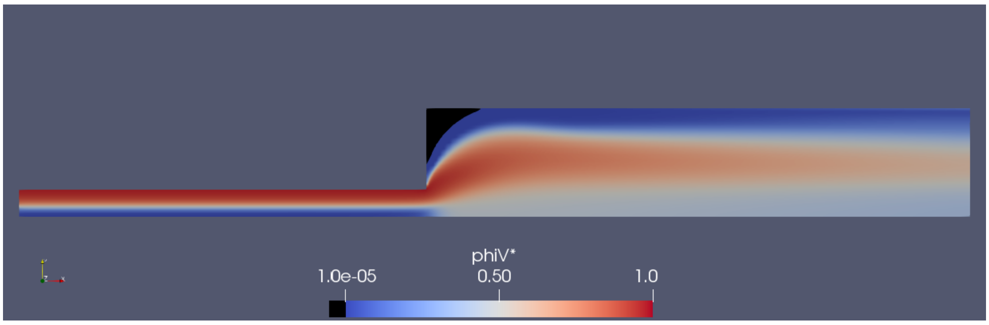

(b) $t^* = 650$

The $\mathrm{T}_{c,0} = 10^2$ flow is between these two behaviours, where the value of $\mathrm{T}^*_{c,0}$ is able to recover the material at the wide channel, but at a relatively low rate. This way, the material can recover the microstructure of some regions that have been unstructured by the yield front behaviour, but this process is not fast enough to completely erase all its consequences. Thus, $T_{c,0} = 10^2$ has the opposite effect of the $T_{c,0} = 10^4$ flow: as the flow advances to the steady-state, the flow is more and more concentrated near the symmetry line, increasing its velocity. Figure 48 and Figure 49 shows the normalized fluidity field and the horizontal velocity field for $T_{c,0} = 10^2$ and $t^* = 100$ and $t^* = 650$, respectively.

Figure 49 – u_x^* for $T_{c,0} = 10^2$ and (a) $t^* = 100$ and (b) $t^* = 650$ at the expansion geometry. The adopted dimensionless parameters are presented in Table 11.

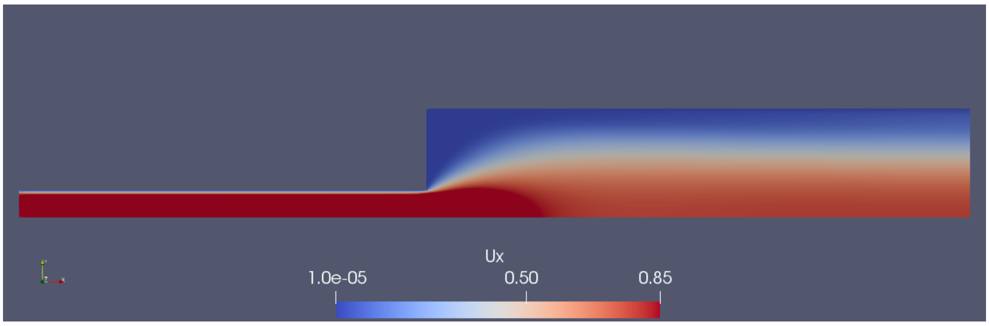

(a) $t^* = 100$

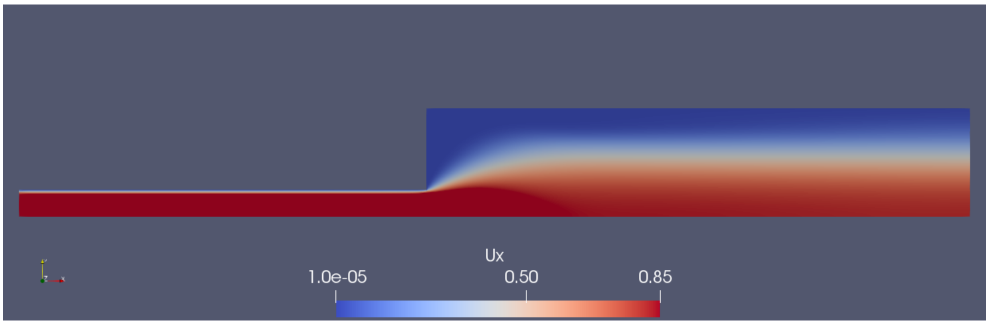

(b) $t^* = 650$

In the same way, the contraction geometry increases the influence of α_t when compared to the expansion geometry, it decreases the influence of $T^*_{c,0}$. As the flow starts fully structured and the inlet channel is the wide channel, the material must first have its microstructure broken, and then flow to a region with $\phi_v^* > \phi_{eq}^*$ to $T^*_{c,0}$ be a relevant parameter. As already discussed, the only region of the contraction geometry that satisfies these conditions is the region near the symmetry line of the narrow channel.

Figure 50 shows the u_x^* temporal evolution for different values of $T^*_{c,0}$ and Figure 51 shows the ϕ_v^* field for $t* = 100$ and two different values of $T^*_{c,0}$: 10^{-1} and 10^4. The increase from $T_{c,0} = 10^{-1}$ to $T_{c,0} = 10^4$ provoked an increase from $\phi_v^* < 10^{-5}$ to $\phi_v^* \approx 0.5$ at the sample point (5,0) of the narrow channel, and this change led to a decrease of ~ 10% at the local velocity and a reduction of ~ 5% at the flow rate. The local velocity has decreased more due to the tendency to form a plug zone, creating a velocity plateau at the velocity profile, as can be seen in Figure 52.

Figure 50 – Influence of $T^*_{c,0}$ over the temporal evolution of u^*_x at the symmetry line of (a) the wide channel (-10,0) and (b) the narrow channel (5,0) at the contraction geometry. The adopted dimensionless parameters are presented in Table 11.

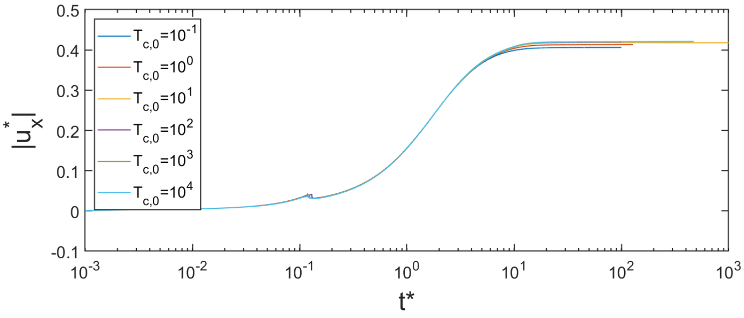

(a) (-10,0)

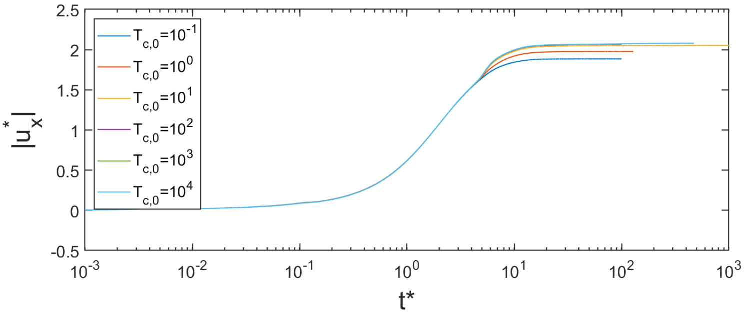

(b) (5,0)

Figure 51 – ϕ^*_v field for the contraction geometry at $t^* = 10^2$ and (a) $T_{c,0} = 10^{-1}$, and (b) $T_{c,0} = 10^4$. The adopted dimensionless parameters are presented in Table 11.

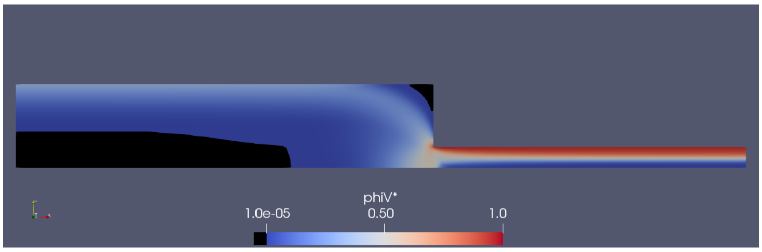

(a) $T_{c,0} = 10^{-1}$

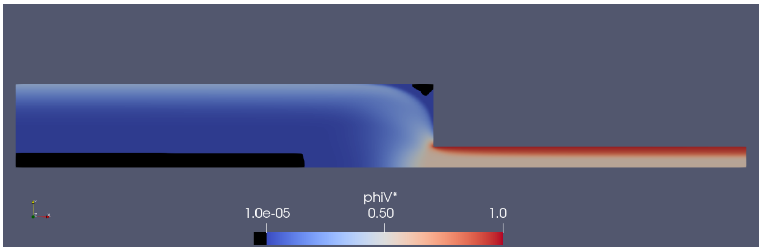

(b) $T_{c,0} = 10^4$

6.6 The influence of the Δp^*

The imposed pressure gradient is the driving force of the analyzed flow. In this section, Δp^* ranging from 40 to 120 were tested. The results are shown in Figure 53 for the

Figure 52 – Velocity profile for the contraction geometry at $x^* = 5$ and $t^* = 10^2$ for $\mathrm{T}_{c,0} = 10^{-1}$ and $\mathrm{T}_{c,0} = 10^4$. The adopted dimensionless parameters are presented in Table 11.

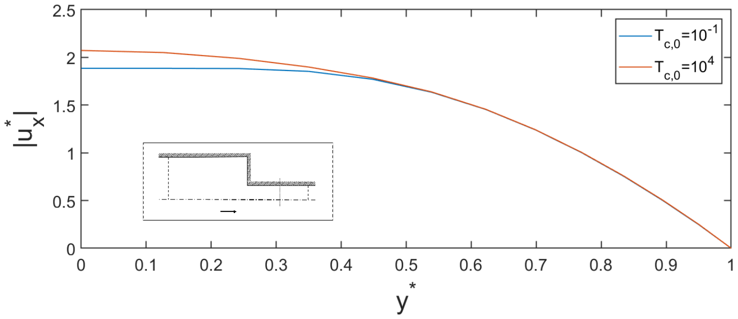

temporal evolution of the u_x^* for the expansion geometry. The dimensionless parameters are shown in Table 12.

Table 12 – The dimensionless parameters adopted in Section 6.6.

ϕ_0^*	n	$\dot{\gamma}_1^*$	α_t	$\mathrm{T}_{c,0}^*$	De	Δp^*	Re
10^{-3}	0.3	1	10^1	10^4	1	40 to 120	0.0456 to 2.087

Figure 53 – Influence of Δp^* over the temporal evolution of u_x^* at the symmetry line of (a) the narrow channel (-5,0) and (b) the wide channel (10,0) at the expansion geometry. The adopted dimensionless parameters are presented in Table 12.

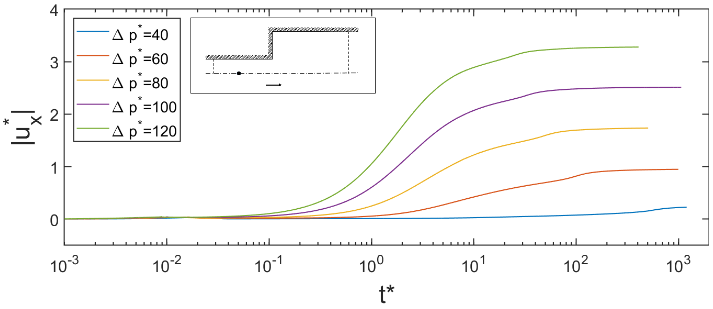

(a) (-5,0)

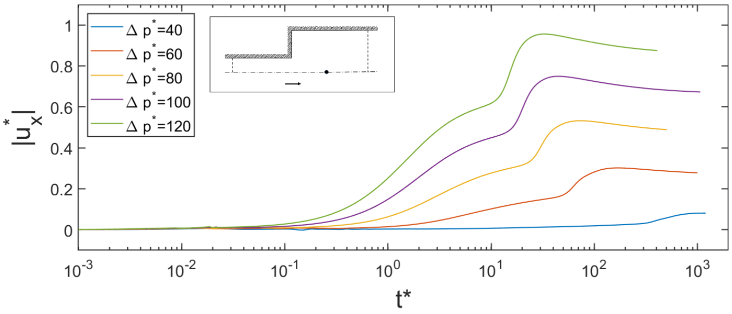

(b) (10,0)

As expected, the higher the Δp^*, the higher the velocities, the faster ϕ_v^* increases and the faster the flow achieves the steady-state. Due to the rheological dimensionless set, all simulations show the effects of the yield front, even the $\Delta p^* = 40$, which has a relatively low velocity before the yield front behaviour. Due to its low velocity, the time it takes to achieve the steady-state is higher.

All simulations of the section have a characteristic stress between $2\tau_0$ and $6\tau_0$. This means that probably all these simulations have a Δp^* relativity higher than the minimum imposed pressure gradient to re-start the flow. The calculation of τ_c does not take into account the effects of the expansion, thus the estimative of $\tau_c = \tau_0$ to the minimum imposed pressure gradient to re-start the flow may not be accurate. For example: the flow for $\Delta p^* = 40$ has a relatively low velocity and only shows a visible acceleration when almost all other simulations are already at steady-state, indicating the minimum imposed pressure gradient may not be distant.

Several images in the previous sections show stress fields where the whole wide channel of the expansion geometry is under the $\tau < \tau_0$ condition and the reasons and consequences of this scenario were discussed. These results may lead to the conclusion that it is possible to have, under the proposed circumstances, a restart flow with $\tau_c \leq \tau_0$. However, the presented results are not enough to sustain that conclusion. A $\Delta p^* = 20$ simulation was originally planned, which means $\tau_c = \tau_0$, but it achieves the adopted steady-state condition before it starts to flow. This $\Delta p^* = 20$ simulation had $\phi_v^* > \phi_0^*$ near the narrow channel walls, and its maximum velocity was around $|\mathbf{u}^*| \approx 10^{-3}$. In theory, this small velocity could be able to transport the material with $\phi_v^* > \phi_0^*$ through the wide channel, if the simulation lasts long enough and the $\mathrm{T}_{c,0}^*$ is high enough. However, under these circumstances, the velocity values are highly influenced by the value of ϕ_0^*. Thus, a deeper analysis of the ϕ_0^* influence would be necessary for the correct interpretation of the results.

Changing the Δp^* also impacted the Re, as the density was kept constant. Thus, the Re values in this section range from 0.0456 (for $\Delta p^* = 40$) to 2.087 (for $\Delta p^* = 120$). These values are estimates and are only used as a reference, to analyze if the inertia forces are relevant or not.

Figure 54 shows the temporal evolution of u_x^* for Δp^* values ranging from 40 to 120 at the contraction geometry. As already discussed, the contraction geometry tends to have lower velocities when compared to the expansion geometry, and the effects of the yield front are limited. These conditions are critical to lower values of Δp^*, and the maximum velocity value for $\Delta p^* = 40$ is around 10^-1, almost one-seventh of the maximum velocity of $\Delta p^* = 60$, for example.

Figure 55 presents the temporal evolution of the ϕ_v^* at the narrow channel symmetry line. Decreasing Δp^* decreases the stress, decreasing the relevance of the breakup term of the fluidity evolution equation (Equation 4.7). Decreasing Δp^* also decreases the flow velocity, increasing the time needed to transport ϕ_v^* over the domain. These changes delay

Figure 54 – Influence of Δp^* over the temporal evolution of u_x^* at the symmetry line of (a) the wide channel (-10,0) and (b) the narrow channel (5,0) at the contraction geometry. The adopted dimensionless parameters are presented in Table 12

.

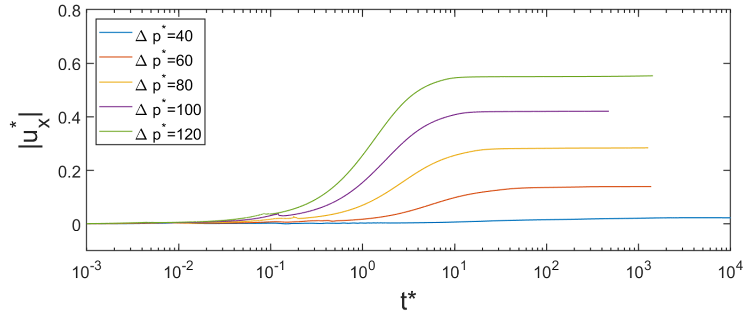

(a) (-10,0)

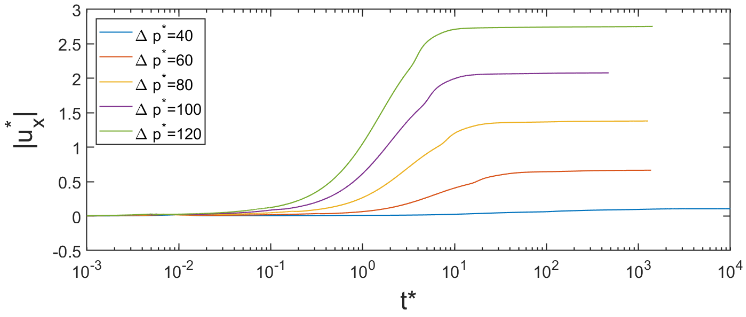

(b) (5,0)

the steady-state.

Figure 55 – Influence of Δp^* over the temporal evolution of ϕ_v^* at the symmetry line of the narrow channel (5,0). The adopted dimensionless parameters are presented in Table 12

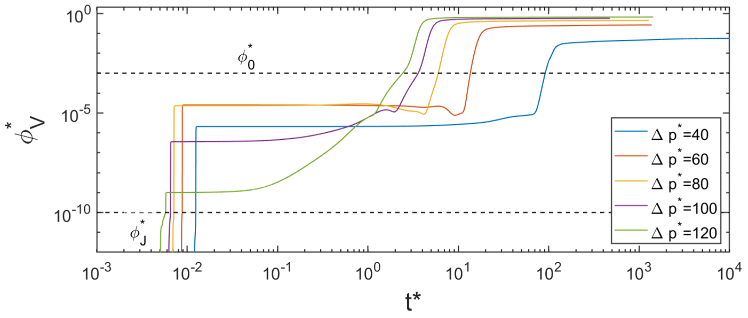

Part IV

Final remarks

7 Conclusions

The present work discussed the effects of several rheological and flow parameters on the velocity field and the fluidity field on a 4:1 contraction and a 1:4 expansion geometries, adopting the model proposed by (DE SOUZA MENDES; ABEDI; THOMPSON, 2018). The adopted model can emulate the viscoelastic, viscoplastic and thixotropic behaviours, and the rheological parameters of an aqueous suspension of laponite were used as a starting point for the dimensionless quantities adopted in the present work.

An OpenFOAM® routine was developed to solve the TEVP flow, taking into account the inertia effects and considering the flow as incompressible and isothermal. The flow was initially at rest, fully structured and without any internal effort. Then, a flat pressure profile was imposed at the inlet and the outlet of the domain, creating a pressure gradient between them. This pressure gradient served as the driving force of the flow, breaking its internal microstructure and accelerating it.

During the development of the routine, the numerical tools offered by the toolbox RheoTool were tested, but none of them showed a real improvement for the algorithm. The characteristics of the adopted viscoelastic behaviour do not justify the need to implement a log conformation routine, especially when considering the limitations imposed by this scheme. Furthermore, the viscoelastic stabilization method recommended by the RheoTool User manual presented an efficiency equivalent of the efficiency of the explicit diffusion technique when the term to account the variation of η_p was implemented.

The effects of the De, α_t, $\mathrm{T}^*_{c,0}$, and Δp^* were analyzed for both geometries. Different flow behaviours were identified and discussed during the analysis, with a direct impact on the flow velocity and fluidity.

The flow accelerated faster when the viscoelastic behaviour was considered, even though the steady-state velocity was the same for both conditions. The compliance function adopted in the present work predicted that the viscoelastic behaviour was only relevant when the material was fully structured ($\phi^*_v > 10^{-10}$), thus it was expected that the aforementioned behaviour would be less relevant as the flow develops. Another relevant behaviour identified was a stress peak at the moment when the viscoelastic behaviour ceases. This stress peak proved capable of increasing the normalized fluidity even from areas that usually have $\tau < \tau_0$ and changing, for example, the relevance of the viscoelastic regions after this stress peak dissipates. The $De > 0$ simulations also showed a deceleration after the stress peak. The origins and consequences of this behaviour were discussed, highlighting the conditions that increase its relevance.

As the material starts fully structured, its internal microstructure must be broken so it can flow. Thus, α_t showed to be one of the main dimensionless parameters of the flow. Increasing it decreases the velocity at both geometries, and it is especially relevant at the contraction geometry. At the contraction geometry, the material flows from a low-stress area to a high-stress area, creating an "entrance length", where the microstructure of the material is being broken. This entrance length decreases the fluidity of the flow and decreases the flow velocity. On the other hand, in the expansion geometry, the fluid flows from a high-stress area to a low-stress area, and the relatively high fluidity material is transported through the wide channel, allowing higher velocities and allowing the material to flow with the $\tau < \tau_0$ condition.

The influence of the $\mathrm{T}^*_{c,0}$ was shown to be more limited than the α_t influence. Usually, the region near the wall has relatively higher stresses and is more relevant to the flow. This way, $\mathrm{T}^*_{c,0}$ is more relevant at the regions near the symmetry line, with less relevance over the flow as a whole, but can change the velocity profile inside the domain.

Finally, different values of Δp^* were considered. As the material density was kept constant for the different simulations, changing the Δp^* also changed the Re. As the flow accelerates over time and due to the material complexity, it is not an easy task to define a characteristic velocity of the flow, thus the Re is only used as a reference, to identify if the inertia forces are relevant or not. Δp^* represents the driving forces of the flow, and decreasing it increases the time to achieve the steady-state, as a lower Δp^* means lower stresses and velocities, which decreases the magnitude of the breakup term and the advective transport term of the fluidity evolution equation.

Several results presented in Chapter 6 show that a relevant part of the domain has $\tau < \tau_0$, even though its velocity is not null nor constant. This can be explained by the transport of unstructured material from high-stress zones to low-stress zones. Even though this behaviour suggests that it is possible to a complex material flow with a pressure gradient lower than τ_0, the presented results are not enough to support this conclusion. Thus, future works are needed to understand the influence of ϕ^*_0 and its interactions with other rheological and operational parameters. The $J(\phi^*_v)$ function also needs more attention, even though its effects may be attenuated by the influence of the viscoelastic forces. Future works should also investigate more complex geometries, especially because the present work showed that the geometry can have a direct impact on the minimum pressure gradient to reestablish the steady-state flow.

References

ABEDI, B.; MENDES, R.; DE SOUZA MENDES, P. R. Startup flow of yield-stress non-thixotropic and thixotropic materials in a tube. *Journal of Petroleum Science and Engineering*, Elsevier, v. 174, p. 437–445, 2019.

ABIVIN, P.; TAYLOR, S. D.; FREED, D. Thermal behavior and viscoelasticity of heavy oils. *Energy & fuels*, ACS Publications, v. 26, n. 6, p. 3448–3461, 2012.

AIYEJINA, A. et al. Wax formation in oil pipelines: A critical review. *International journal of multiphase flow*, Elsevier, v. 37, n. 7, p. 671–694, 2011.

ALI, S. I. et al. Phenomena, factors of wax deposition and its management strategies. *Arabian Journal of Geosciences*, Springer, v. 15, n. 2, p. 133, 2022.

ALNAIMAT, F.; ZIAUDDIN, M. Wax deposition and prediction in petroleum pipelines. *Journal of Petroleum Science and Engineering*, Elsevier, v. 184, p. 106385, 2020.

AMOREIRA, L.; OLIVEIRA, P. Comparison of different formulations for the numerical calculation of unsteady incompressible viscoelastic fluid flow. *Adv. Appl. Math. Mech*, v. 2, n. 4, p. 483–502, 2010.

ANDRADE, D. E.; COUSSOT, P. Thermal fatigue and collapse of waxy suspensions. *Rheologica Acta*, Springer, v. 59, p. 279–289, 2020.

ASME, F. E. D. of. Procedure for Estimation and Reporting of Uncertainty Due to Discretization in CFD Applications. *Journal of Fluids Engineering*, v. 130, n. 7, p. 078001, 07 2008. ISSN 0098-2202. Avaible: <https://doi.org/10.1115/1.2960953>.

AZEVEDO, L. F. A.; TEIXEIRA, A. M. A critical review of the modeling of wax deposition mechanisms. *Petroleum Science and Technology*, Taylor & Francis, v. 21, n. 3-4, p. 393–408, 2003. Avaible: <https://doi.org/10.1081/LFT-120018528>.

BAO, Y.; ZHANG, J. Restart behavior of gelled waxy crude oil pipeline based on an elasto-viscoplastic thixotropic model: A numerical study. *Journal of Non-Newtonian Fluid Mechanics*, Elsevier, v. 284, p. 104377, 2020.

BARNES, H. A. Thixotropy—a review. *Journal of Non-Newtonian Fluid Mechanics*, v. 70, n. 1, p. 1–33, 1997. ISSN 0377-0257. Avaible: <https://www.sciencedirect.com/science/article/pii/S0377025797000049>.

BAUTISTA, F. et al. Understanding thixotropic and antithixotropic behavior of viscoelastic micellar solutions and liquid crystalline dispersions. i. the model. *Journal of Non-Newtonian Fluid Mechanics*, v. 80, n. 2, p. 93–113, 1999. ISSN 0377-0257. Avaible: <https://www.sciencedirect.com/science/article/pii/S0377025798000810>.

BIRD, R. B.; WIEST, J. M. Constitutive equations for polymeric liquids. *Annual review of fluid mechanics*, Annual Reviews 4139 El Camino Way, PO Box 10139, Palo Alto, CA 94303-0139, USA, v. 27, n. 1, p. 169–193, 1995.

BOEK, E. et al. Constitutive equations for extensional flow of wormlike micelles: stability analysis of the bautista–manero model. *Journal of non-newtonian fluid mechanics*, Elsevier, v. 126, n. 1, p. 39–46, 2005.

CALDERAS, F. et al. On the yield stress of complex materials. *Korea-Australia Rheology Journal*, Springer, v. 25, p. 233–242, 2013.

CHALA, G. T.; SULAIMAN, S. A.; JAPPER-JAAFAR, A. Flow start-up and transportation of waxy crude oil in pipelines-a review. *Journal of Non-Newtonian Fluid Mechanics*, v. 251, p. 69–87, 2018. ISSN 0377-0257. Avaible: <https://www.sciencedirect.com/science/article/pii/S0377025717300903>.

CHALA, G. T. et al. Temporal variation of voids in waxy crude oil gel in the presence of temperature gradient. *Chemical Engineering Communications*, Taylor & Francis, v. 207, n. 10, p. 1403–1414, 2020. Avaible: <https://doi.org/10.1080/00986445.2019.1655403>.

CHALA, G. T. et al. Influence of hydrostatic pressure on the formation of voids in gelled crude oil. *Applied Science and Engineering Progress*, v. 15, n. 4, p. 5569–5569, 2022.

CHEDDADI, I.; SARAMITO, P.; GRANER, F. Steady couette flows of elastoviscoplastic fluids are nonunique. *Journal of rheology*, The Society of Rheology, v. 56, n. 1, p. 213–239, 2012.

CHHABRA, R. P.; RICHARDSON, J. F. *Non-Newtonian flow in the process industries: fundamentals and engineering applications.* [S.l.]: Butterworth-Heinemann, 1999. ISBN 978-0750637701.

CHRISMAN, E. C. N. et al. Wax chemical and morphological investigation of brazilian crude oils. In: SOLIMAN, F. S. (Ed.). *Paraffin-an Overview.* Rijeka: IntechOpen, 2019. cap. 2. Avaible: <https://doi.org/10.5772/intechopen.83736>.

COURANT, R.; FRIEDRICHS, K.; LEWY, H. On the partial difference equations of mathematical physics. *IBM journal of Research and Development*, IBM, v. 11, n. 2, p. 215–234, 1967.

COUSSOT, P. et al. Avalanche behavior in yield stress fluids. *Physical review letters*, APS, v. 88, n. 17, p. 175501, 2002.

CUNHA, J. P.; DE SOUZA MENDES, P. R.; SIQUEIRA, I. R. Pressure-driven flows of a thixotropic viscoplastic material: Performance of a novel fluidity-based constitutive model. *Physics of Fluids*, v. 32, n. 12, p. 123104, 2020. Avaible: <https://doi.org/10.1063/5.0031991>.

DALLA, L. F.; SOARES, E. J.; SIQUEIRA, R. N. Start-up of waxy crude oils in pipelines. *Journal of Non-Newtonian Fluid Mechanics*, Elsevier, v. 263, p. 61–68, 2019.

DE SOUZA MENDES, P. R.; ABEDI, B.; THOMPSON, R. L. Constructing a thixotropy model from rheological experiments. *Journal of Non-Newtonian Fluid Mechanics*, Elsevier, v. 261, p. 1–8, 2018.

DE SOUZA MENDES, P. R.; THOMPSON, R. L. A critical overview of elasto-viscoplastic thixotropic modeling. *Journal of Non-Newtonian Fluid Mechanics*, Elsevier, v. 187, p. 8–15, 2012.

DE SOUZA MENDES, P. R.; THOMPSON, R. L. Time-dependent yield stress materials. *Current Opinion in Colloid & Interface Science*, Elsevier, v. 43, p. 15–25, 2019.

DOORMAAL, J. P. V.; RAITHBY, G. D. Enhancements of the simple method for predicting incompressible fluid flows. *Numerical Heat Transfer*, Taylor & Francis, v. 7, n. 2, p. 147–163, 1984. Avaible: <https://doi.org/10.1080/01495728408961817>.

DUARTE, A.; MIRANDA, A.; OLIVEIRA, P. Numerical and analytical modeling of unsteady viscoelastic flows: The start-up and pulsating test case problems. *Journal of Non-Newtonian Fluid Mechanics*, v. 154, n. 2, p. 153–169, 2008. ISSN 0377-0257. Avaible: <https://www.sciencedirect.com/science/article/pii/S037702570800092X>.

DULLAERT, K.; MEWIS, J. A structural kinetics model for thixotropy. *Journal of Non-Newtonian Fluid Mechanics*, v. 139, n. 1, p. 21–30, 2006. ISSN 0377-0257. Avaible: <https://www.sciencedirect.com/science/article/pii/S0377025706001431>.

EL-DALATONY, M. M. et al. Occurrence and characterization of paraffin wax formed in developing wells and pipelines. *Energies*, MDPI, v. 12, n. 6, p. 967, 2019.

FATTAL, R.; KUPFERMAN, R. Constitutive laws for the matrix-logarithm of the conformation tensor. *Journal of Non-Newtonian Fluid Mechanics*, Elsevier, v. 123, n. 2-3, p. 281–285, 2004.

FRIGAARD, I.; VINAY, G.; WACHS, A. Compressible displacement of waxy crude oils in long pipeline startup flows. *Journal of Non-Newtonian Fluid Mechanics*, v. 147, n. 1, p. 45–64, 2007. ISSN 0377-0257. Avaible: <https://www.sciencedirect.com/science/article/pii/S0377025707001607>.

GIANNOKOSTAS, K. et al. Advanced constitutive modeling of the thixotropic elasto-visco-plastic behavior of blood: Description of the model and rheological predictions. *Materials*, Multidisciplinary Digital Publishing Institute, v. 13, n. 18, p. 4184, 2020.

GUERRERO, J. 2018 summer session - unige introductory openfoam training. *University of Genoa. DICCA.*, July 2018.

GUéNETTE, R.; FORTIN, M. A new mixed finite element method for computing viscoelastic flows. *Journal of Non-Newtonian Fluid Mechanics*, v. 60, n. 1, p. 27–52, 1995. ISSN 0377-0257. Avaible: <https://www.sciencedirect.com/science/article/pii/0377025795013723>.

HAJIKARIMI, P.; Moghadas Nejad, F. Chapter 3 - mechanical models of viscoelasticity. In: HAJIKARIMI, P.; Moghadas Nejad, F. (Ed.). *Applications of Viscoelasticity*. Elsevier, 2021. p. 27–61. ISBN 978-0-12-821210-3. Avaible: <https://www.sciencedirect.com/science/article/pii/B9780128212103000036>.

HAMMAMI, A.; RATULOWSKI, J.; COUTINHO, J. A. Cloud points: can we measure or model them? *Petroleum Science and Technology*, Taylor & Francis, v. 21, n. 3-4, p. 345–358, 2003.

HAO, L. Z.; AL-SALIM, H. S.; RIDZUAN, N. A review of the mechanism and role of wax inhibitors in the wax deposition and precipitation. *Pertanika Journal of Science & Technology*, v. 27, n. 1, 2019.

HELSPER, S.; ALI, A. A.; LIBERATORE, M. W. Shear alters wax appearance in mineral oil+ paraffin wax mixtures. *Rheologica Acta*, Springer, v. 60, n. 9, p. 521–529, 2021.

HOU, L.; ZHANG, J.-j. Viscoelasticity of gelled waxy crude oil. *Journal of Central South University of Technology*, Springer, v. 14, p. 414–417, 2007.

ISSA, R. Solution of the implicitly discretised fluid flow equations by operator-splitting. *Journal of Computational Physics*, v. 62, n. 1, p. 40–65, 1986. ISSN 0021-9991. Avaible: <https://www.sciencedirect.com/science/article/pii/0021999186900999>.

JAHROMI, H. T. et al. Numerical investigation of transient contraction flows for worm-like micellar systems using bautista–manero models. *Journal of non-newtonian fluid mechanics*, Elsevier, v. 166, n. 1-2, p. 102–117, 2011.

KANÉ, M. et al. Morphology of paraffin crystals in waxy crude oils cooled in quiescent conditions and under flow. *Fuel*, v. 82, n. 2, p. 127–135, 2003. ISSN 0016-2361. Avaible: <https://www.sciencedirect.com/science/article/pii/S0016236102002223>.

KARIMI, Y.; NAZAR, A. R. S. An experimental study on evaluation of factors influencing the viscosity and viscoelastic properties of waxy crude oil. *Iranian Journal of Oil and Gas Science and Technology*, Petroleum University of Technology, v. 9, n. 1, p. 1–15, 2020.

LARSON, R. G.; WEI, Y. A review of thixotropy and its rheological modeling. *Journal of Rheology*, The Society of Rheology, v. 63, n. 3, p. 477–501, 2019.

LEE, H. S. et al. Waxy oil gel breaking mechanisms: adhesive versus cohesive failure. *Energy & Fuels*, ACS Publications, v. 22, n. 1, p. 480–487, 2008.

LEGNANI, A. et al. Waxy oils: deformation-dependent materials. *Journal of Non-Newtonian Fluid Mechanics*, Elsevier, v. 285, p. 104378, 2020.

LI, H. et al. The influence of the heating temperature on the yield stress and pour point of waxy crude oils. *Journal of Petroleum Science and Engineering*, v. 135, p. 476–483, 2015. ISSN 0920-4105. Avaible: <https://www.sciencedirect.com/science/article/pii/S0920410515301376>.

LINK, F. B. et al. Plane flow of thixotropic elasto-viscoplastic materials through a 1: 4 sudden expansion. *Journal of Non-Newtonian Fluid Mechanics*, Elsevier, v. 220, p. 162–174, 2015.

LÓPEZ-AGUILAR, J. et al. A new constitutive model for worm-like micellar systems–numerical simulation of confined contraction–expansion flows. *Journal of Non-Newtonian Fluid Mechanics*, Elsevier, v. 204, p. 7–21, 2014.

LÓPEZ-AGUILAR, J. E. et al. Numerical modelling of thixotropic and viscoelastoplastic materials in complex flows. *Rheologica Acta*, Springer, v. 54, p. 307–325, 2015.

LUTHI, I. F. Waxy crude oil characterization and experimental study of the restart of a line blocked with gelled waxy crude. In: ONEPETRO. *SPE Annual Technical Conference and Exhibition*. [S.l.], 2013.

MENDES, P. R. de S. Thixotropic elasto-viscoplastic model for structured fluids. *Soft Matter*, Royal Society of Chemistry, v. 7, n. 6, p. 2471–2483, 2011.

MEWIS, J.; WAGNER, N. J. Thixotropy. *Advances in Colloid and Interface Science*, v. 147-148, p. 214–227, 2009. ISSN 0001-8686. Colloids, polymers and surfactants.Special Issue in honour of Brian Vincent. Avaible: <https://www.sciencedirect.com/science/article/pii/S0001868608001735>.

MOISÉS, G. et al. The influence of thixotropy in start-up flow of yield stress fluids in a pipe. *Journal of Petroleum Science and Engineering*, Elsevier, v. 171, p. 794–807, 2018.

NEGRÃO, C. O.; FRANCO, A. T.; ROCHA, L. L. A weakly compressible flow model for the restart of thixotropic drilling fluids. *Journal of Non-Newtonian Fluid Mechanics*, Elsevier, v. 166, n. 23-24, p. 1369–1381, 2011.

NOVAES, R. C. S. *Campos maduros e áreas de acumulações marginais de petróleo e gás natural: uma análise da atividade econômica no recôncavo baiano*. Dissertação (Mestrado) — Universidade de São Paulo, São Paulo, 2010.

OBERKAMPF, W. L.; TRUCANO, T. G.; HIRSCH, C. Verification, validation, and predictive capability in computational engineering and physics . *Applied Mechanics Reviews*, v. 57, n. 5, p. 345–384, 12 2004. ISSN 0003-6900. Avaible: <https://doi.org/10.1115/1.1767847>.

OH, K.; JEMMETT, M.; DEO, M. Yield behavior of gelled waxy oil: Effect of stress application in creep ranges. *Industrial & Engineering Chemistry Research*, v. 48, n. 19, p. 8950–8953, 2009. Avaible: <https://doi.org/10.1021/ie9000597>.

OISHI, C. M.; MARTINS, F. P.; THOMPSON, R. L. The “avalanche effect” of an elasto-viscoplastic thixotropic material on an inclined plane. *Journal of Non-Newtonian Fluid Mechanics*, Elsevier, v. 247, p. 165–177, 2017.

OISHI, C. M.; THOMPSON, R. L.; MARTINS, F. P. Transient motions of elasto-viscoplastic thixotropic materials subjected to an imposed stress field and to stress-based free-surface boundary conditions. *International Journal of Engineering Science*, Elsevier, v. 109, p. 165–201, 2016.

OLAJIRE, A. A. Review of wax deposition in subsea oil pipeline systems and mitigation technologies in the petroleum industry. *Chemical Engineering Journal Advances*, Elsevier, v. 6, p. 100104, 2021.

OLDROYD, J. G. On the formulation of rheological equations of state. *Proceedings of the Royal Society of London. Series A. Mathematical and Physical Sciences*, The Royal Society London, v. 200, n. 1063, p. 523–541, 1950.

PATANKAR, S. *Numerical heat transfer and fluid flow*. [S.l.]: Taylor & Francis, 1980.

PATANKAR, S. V.; SPALDING, D. B. A calculation procedure for heat, mass and momentum transfer in three-dimensional parabolic flows. *International Journal Heat Mass Transfer*, v. 15, p. 1787–1806, 1972.

PHILLIPS, D. A. et al. Novel approaches to waxy crude restart: Part 1: Thermal shrinkage of waxy crude oil and the impact for pipeline restart. *Journal of Petroleum Science and Engineering*, Elsevier, v. 77, n. 3-4, p. 237–253, 2011.

PIMENTA, F. *Rheotool User Guide Version 6.0*. [S.l.], 2022. Avaible: <https://github.com/fppimenta/rheoTool>.

PIMENTA, F.; ALVES, M. Stabilization of an open-source finite-volume solver for viscoelastic fluid flows. *Journal of Non-Newtonian Fluid Mechanics*, v. 239, p. 85–104, 2017. ISSN 0377-0257. Avaible: <https://www.sciencedirect.com/science/article/pii/S0377025716303329>.

PIMENTA, F.; ALVES, M. A. A coupled finite-volume solver for numerical simulation of electrically-driven flows. *Computers & Fluids*, Elsevier, v. 193, p. 104279, 2019.

POOLE, R. The deborah and weissenberg numbers. *Rheology Bulletin*, v. 53, n. 2, p. 32–39, 2012.

REISTLE, C. E. Methods of dealing with paraffin troubles encountered in producing crude oil. US Government Printing Office, v. 414, 1928.

REISTLE, C. E. Paraffin and congealing-oil problems. US Government Printing Office, v. 348, 1932.

RICHARDSON, L. F. The approximate arithmetical solution by finite differences of physical problems involving differential equations, with an application to the stresses in a masonry dam. *Philosophical Transactions of the Royal Society of London. Series A, Containing Papers of a Mathematical or Physical Character*, The Royal Society, v. 210, p. 307–357, 1911. ISSN 02643952. Avaible: <http://www.jstor.org/stable/90994>.

ROACHE, P. J. Perspective: A Method for Uniform Reporting of Grid Refinement Studies. *Journal of Fluids Engineering*, v. 116, n. 3, p. 405–413, 09 1994. ISSN 0098-2202. Avaible: <https://doi.org/10.1115/1.2910291>.

SÁNCHEZ, H. A. C. et al. Numerical simulation of a thixotropic-viscoelastic model in expansion-contraction geometries. *SSRN*, 2022. Avaible: <https://ssrn.com/abstract=4048814>.

SANDU, C.; WRIGHT, B. Innovative solutions for processing shale oils. *Hydrocarbon Processing*, Gulf Publishing Co., 2013.

SARAMITO, P. A new constitutive equation for elastoviscoplastic fluid flows. *Journal of Non-Newtonian Fluid Mechanics*, Elsevier, v. 145, n. 1, p. 1–14, 2007.

SARGENTINI, R. *Simulação numérica do deslocamento de óleos parafínicos em dutos considerando efeitos térmicos e não newtoninaos*. Dissertação (Mestrado) — Universidade Federal Fluminense, 2013.

SEITZER, W.; LOVELL, P. Flow properties of utah shale oils. *Society of Petroleum Engineers Journal*, OnePetro, v. 21, n. 06, p. 679–686, 1981.

SHAFQUET, A. et al. Estimation of gas void formation in statically cooled waxy crude oil using online capacitance measurement. *International Journal of Multiphase Flow*, Elsevier, v. 75, p. 257–266, 2015.

SIERRA, A. G.; VARGES, P. R.; RIBEIRO, S. S. Startup flow of elasto-viscoplastic thixotropic materials in pipes. *Journal of Petroleum Science and Engineering*, Elsevier, v. 147, p. 427–434, 2016.

SIQUEIRA, I. R.; PASQUALI, M.; DE SOUZA MENDES, P. R. Couette flows of a thixotropic yield-stress material: Performance of a novel fluidity-based constitutive model. *Journal of Rheology*, v. 64, n. 4, p. 889–898, 2020. Avaible: <https://doi.org/10.1122/8.0000041>.

SOUSA, A. M. et al. Review of the economic and environmental impacts of producing waxy crude oils. *Energies*, Multidisciplinary Digital Publishing Institute, v. 16, n. 1, p. 120, 2023.

SULAIMAN, S. A.; CHALA, G. T.; ZAINUR, M. Z. Experimental investigation of compressibility of waxy crude oil subjected to static cooling. *Journal of Petroleum Science and Engineering*, Elsevier, v. 182, p. 106378, 2019.

TARCHA, B. et al. The elasto-viscoplastic-time-dependent nature of waxy crude oils. *Revista de Engenharia Térmica*, v. 13, n. 2, p. 16–19, 2014.

TENG, H.; ZHANG, J. A new thixotropic model for waxy crude. *Rheologica Acta*, Springer, v. 52, p. 903–911, 2013.

THIEN, N. P.; TANNER, R. I. A new constitutive equation derived from network theory. *Journal of Non-Newtonian Fluid Mechanics*, Elsevier, v. 2, n. 4, p. 353–365, 1977.

THOMPSON, R. L.; SOARES, E. J. Viscoplastic dimensionless numbers. *Journal of Non-Newtonian Fluid Mechanics*, v. 238, p. 57–64, 2016. ISSN 0377-0257. Viscoplastic Fluids From Theory to Application 2015 (VPF6). Avaible: <https://www.sciencedirect.com/science/article/pii/S0377025716300465>.

TINSLEY, J. F. et al. Waxy gels with asphaltenes 1: Characterization of precipitation, gelation, yield stress, and morphology. *Energy & Fuels*, ACS Publications, v. 23, n. 4, p. 2056–2064, 2009.

VARCHANIS, S. et al. Modeling the rheology of thixotropic elasto-visco-plastic materials. *Journal of Rheology*, The Society of Rheology, v. 63, n. 4, p. 609–639, 2019.

VINAY, G.; WACHS, A.; FRIGAARD, I. Start-up transients and efficient computation of isothermal waxy crude oil flows. *Journal of Non-Newtonian Fluid Mechanics*, v. 143, n. 2, p. 141–156, 2007. ISSN 0377-0257. Avaible: <https://www.sciencedirect.com/science/article/pii/S0377025707000651>.

VISINTIN, R. F. et al. Structure of waxy crude oil emulsion gels. *Journal of Non-Newtonian Fluid Mechanics*, Elsevier, v. 149, n. 1-3, p. 34–39, 2008.

WACHS, A.; VINAY, G.; FRIGAARD, I. A 1.5 d numerical model for the start up of weakly compressible flow of a viscoplastic and thixotropic fluid in pipelines. *Journal of Non-Newtonian Fluid Mechanics*, Elsevier, v. 159, n. 1-3, p. 81–94, 2009.

WATERS, N. D.; KING, M. J. Unsteady flow of an elastico-viscous liquid. *Rheologica Acta*, v. 9, p. 345–355, 1970.

ZHANG, J.-j.; LIU, X. Some advances in crude oil rheology and its application. *Journal of Central South University of Technology*, Springer, v. 15, n. 1, p. 288–292, 2008.

ZHAO, J. et al. Research on heat transfer characteristic of waxy crude oil during the gelatinization process in the floating roof tank. *International Journal of Thermal Sciences*, v. 115, p. 139–159, 2017. ISSN 1290-0729. Avaible: <https://www.sciencedirect.com/science/article/pii/S1290072916310122>.

ZHAPBASBAYEV, U. et al. Flow and heat exchange calculation of waxy oil in the industrial pipeline. *Case Studies in Thermal Engineering*, Elsevier, v. 26, p. 101007, 2021.